Title	Designing Mechanical Tools for Flexible Robotic Assembly with Manipulators and Two-Finger Parallel Grippers
Author(s)	胡, 正涛
Citation	大阪大学, 2022, 博士論文
Version Type	VoR
URL	https://doi.org/10.18910/88105
rights	
Note	

Designing Mechanical Tools for Flexible Robotic Assembly with Manipulators and Two-Finger Parallel Grippers

ZHENGTAO HU

MARCH 2022

Designing Mechanical Tools for Flexible Robotic Assembly with Manipulators and Two-Finger Parallel Grippers

A dissertation submitted to
THE GRADUATE SCHOOL OF ENGINEERING SCIENCE
OSAKA UNIVERSITY
in partial fulfillment of the requirements for the degree of
DOCTOR OF PHILOSOPHY IN ENGINEERING

BY

ZHENGTAO HU

MARCH 2022

Designing Mechanical Tools for Flexible Robotic Assembly with Manipulators and Two-Finger Parallel Grippers

Zhengtao Hu

Osaka University 2022

Abstract

This thesis focuses on designing mechanical tools for two-finger parallel grippers and enabling robots to manipulate various parts for assembly tasks. The manipulation ability of a robot heavily relies on the functions of the equipped hands. For various task requirements, instead of mounting the bulky and costly hand changers or general-purpose hands, using different tools held by a general gripper is a popular way. To be functional, the tools are always designed with embedded transmissions and power devices. Thus, the tailed cables for power supply and control are indispensable. However, the deformable cables result in a high risk of tangling robots and colliding with environment. The proposed tools in this thesis are entirely mechanical and manumotive, allowing the general two-finger parallel grippers to use without any peripheral and power supply. Provided multiple tools with different functions, robots with a simple gripper can easily adapt to various assembly requirements.

The contributions of this thesis consist of three parts. Firstly, the thesis explains the mechanism design and the structure optimization of the tools. The tools manipulated by the gripper can be viewed as a mechanism that transmits the power of the gripper and converts the gripper motion into different output motions on the tooltip. Besides, the tool requires to be firmly held in the manipulation process. The mechanisms design especially considers the transmission and

the grasp constraints. Secondly, the thesis proposes to solve the problems on the aspect of tool use. On the one hand, it includes the task-oriented planning for tool poses and the grasp/regrasp planning for pose reorientation. On the other hand, it employs force-control-based methods to manipulate the tool compliantly against uncertainty, such as inserting tools, exchanging tooltips, and screwing. Additionally, the thesis focuses on an important challenging topic in assembly, eliminating the grasp of uncertainty. A peripheral tool, a triangular corner fixture (TCF), is presented to perform like a regrasp intermedia to reduce the grasp uncertainty in a sensorless way. The TCF can be used to regrasp the goal objects and also the proposed mechanical tool, which effectively helps to achieve precise grasps and increase the success rate of assembly tasks.

The concepts of using mechanical tools, the mechanism designing methods, and the manipulation strategies proposed in this thesis promote the effective solutions on adaptive robotic grasp and varying assembly manipulations. The author believes that using mechanical tools to extend the manipulation abilities of robots is a practical and low-cost approach, and would like to develop more functional tools for fitting wider application needs.

CONTENTS

Chapter 1

Introduction

1.1 Challenges in Modern Manufacturing

In modern society, the booming development makes the market change rapidly, which significantly challenges the manufacturing industry [1]. In the 1960s, the manufacturing industry put the cost on the primary concern to meet the intensive market competition. With the improvement of living standards, product quality gradually dominated. Later, the delivery system becomes a major factor limiting the further development of the market. Nowadays, for the increasingly diverse market, the manufacturing industry has to be adaptable to the requirements of the market segment [2]. Modern manufacturing must be flexible and effective to gear to the customer demands and remain competitive in a changing market [3] [4]. Under this background, a perspective and effective technical route, cellular manufacturing [5], was proposed. This approach is far more efficient than production lines for the demands of small and variable batches of products. Cell manufacturing requires a single piece to be completed in a cell and the production equipment and labor to coordinate to balance the production speed according to the order requirements. In each cell, laborers are assigned with multiple tasks rather than a single repetitive work. This variation greatly exploits the characteristics of humans as intelligent beings to transfer knowledge to complete a series of tasks adaptively and also avoids the fatigue of laborers repeatedly performing a tedious operation.

Not only the production pattern, the popularization of robots has been also contributing to the development of the manufacturing industry. Human laborers expected to get rid of the hard environment, high-intensity work, and arduous operations [6]. Over the past few decades, the replacement of robots on workers has been a growing trend in manufacturing. Robots are the high-precision, high-output and high-speed manipulators, which can perform effectively in hazardous environments without any working time limit. Robot density has also been an important indicator of a country's manufacturing development. For the traditional assembly line operations, industrial robots can be widely deployed as they are just assigned to perform simple and arduous tasks [7]. The deployment of robots undoubtedly liberated a lot of labors and accelerated the production process. However, the essential problem of the ineffective production of the traditional manufacturing still exists.

Applying robots to assist the cell manufacturing is not an easy work. This manufacturing pattern requires human labours to handle a variety of work pieces for high-mix and low volume tasks. However, the current robot systems cannot work effectively without the precise arrangement and cautious teaching, namely, are are inflexible and fail to match the changeable production demands. Thus, the current robot systems are still incapable to replace the human labours [8]. The author, in this dissertation, especially focuses on the manipulation challenges in robotic assembly and provides practical solutions for the robot application in variable conditions.

1.2 Robotic Manipulation and Assembly

Human laborers are hard to be duplicated as their adaptive manipulation ability in job-shop. Humans have both highly adaptive perception and hands, leading to the great working performance in unstructured environments. The lifelong practice and train also benifit human beings from obtaining the adaptive brain-eye-band systems. Contrarily, in the field of manipulation, robots cannot even get trapped by the extremely simple tasks for human works. Robotic manipulation, a challenging topic, has been attracting extensive researches [9] [10]. Manipulation refers to the activities performed by hands. Pragmatically speaking, the difficulties in robotic manipulation involve three aspects: sensing, mechanism, and mechanics [11].

Sensing bridges the gap between robots and the real world. An entire manipulation work always relates two kinds of sensors. One plays the role in the eye of a robot, serving for searching and locating [12] [13]. The other provides the perception of a robotic hand [14], which includes, but is not limited to force/torque [15], contact [16], and tactile [17]. Researchers always pursue robust sensing systems that provide accurate and precise recognition and high-speed feedback.

Mechanism refers to the design of robotic hands. The ability of manipulation directly relies on the function of robotic hands [18]. Researchers pursue to design and organize mechanical components to realize versatile and robust functions in an elegant way. One main concern is to use fewer actuators and sensors to obtain multiplier and more adaptive functions. The other technical route aims to specialize the hand for better and more robust performance in a single task.

Mechanics is about the mathematical and physical principles of manipulation. manipulation can be modeled as a hybrid task combining both kinematic and dynamic processes. Back to the origin of manipulation, mechanics contributes to the analysis of the interaction between an object and manipulators, the sensing and mechanism design are developed to meet the requirements constrained by mechanics. To fast compute the constraints for planning, researchers develop many simplified models to transfer the complicated physical mechanics, they include but are not limited to the estimation of force/form closure and the soft-finger contact model.

A manipulation task always suffers from the changes of the aforementioned three aspects [11]. Considering a robotic assembly task, with a known assembly target, a robot is always required to search and locate the part to be assembled in the environment, stably grasp it, orient its pose, and apply a skillful interaction force to complete the assembly. For the complex assemblies with various parts, how to quickly adapt to different assembly parts is one of the main problem we need to solve.

1.3 Robotic Hands for Various Tasks

The vast majority of assembly tasks start from a grasping motion. Gripped firmly, an objected can be manipulated to exert interaction forces with environment and other parts to complete assembly [19]. So the stable and robust grasp is the precondition of robotic assembly, except some passive compliance control based on slip and in-hand manipulation. The hands and robot motions together decide the overall work performance. The robotic hands are not limited within only grasping but are also expected to exert force to manipulate objects. Therefore, the robotic grippers playing various manipulation tasks, can lighten the burden of the control and planning of the robot body. From the perspective of the development of robotic hands, we hope to expand their adaptation and functionality to facilitate the assembly work. There are conventionally two technical routes. One is to develop versatile and adaptive grippers, the other one is to use hand changers to equip different grippers accordingly.

1.3.1 General-Purpose Hands

In this part, we discuss three types of general-purpose grippers. The first one is adaptive grippers including underactuated grippers, soft grippers, and etc. They are designed with the active or passive mechanisms to build the stable contact pairs between their finger pads and goal objects. For instance, Laliberte et al. [20] developed selfadaptive and reconfigurable robot hand. The underactuated hand has 10 DoFs and two motors. It's finger can adapt to the shape of objects during grasping. Hirata et al. [21] proposed a gripper that can cage and self-align various objects. Liu et al. [22] presented a compliant gripper made by soft materials to grasp size-varied fragile objects. These grippers can perform well for a group of workpieces, however they can never be completely universal. Besides, the adaptive grippers perform effectively for only changeable grasping tasks, consequently, they are incapable of other manipulation requirements.

The second one refers to multi-function grippers. By integrating multiple mechanisms and actuators, this kind of gripper enables the robot to handle different manipulation problems. For instance, Harada et al. [23] developed a novel gripper by combing a multifinger mechanism and a granular jamming component, which can achieve versatile grasping firmly as well as flexibly. Triyonoputro et al. [24] developed a double jaw hand for grasping and assembly. The inner and outer grippers can work together to finish a task. The design was inspired by a human hand holding and manipulating two objects using one hand in product assembly. Nie et al. [25] proposed a pair of fingers for arranging screws. The gripper can pick up and tile a screw to let the screw slide to the bottom of the finger so as to achieve the picking and alignment. However, the multi-function grippers always face the trading-off between the functionality and compact structures. Accumulated functions make the gripper bulky. and the redundant functions also increase the consumption. Additionally, similar to the adaptive gripper, the multi-function grippers are also not completely universal, instead, only applicable for the limited tasks. The multi-function grippers are more like the integrated end-effecters specially customized for a series of tasks.

Anthropopathic hands are also general-purpose grippers as human hands are good at performing flexible grasping and dexterous manipulation [26]. It is the ultimate goal of anthropopathic hands is to completely mimic the motion of human hands. But, in the field of robotic assembly, the large amount of redundancy makes the motion planning hard. And, there is still huge gap between the sensing abilities of human and sensors. Thus, the feedback control of the redundant gripper is still challenging. Additionally, the disadvantages of human hands, such as low accuracy and weak force output, are inherited by the anthropopathic hands.

1.3.2 Hand Changers

Using hand changer is an effective way to extend the functionallity of robots. It is very intuitive to change the current inapplicable gripper into a feasible one. As the hand changer allows robots to using different grippers for different tasks, each gripper can be designed to focus on a single task. Thus, the robots can perform stably for every task. Robot hand changers originate from the tool changers used in Computer Numerical Control (CNC) machines [27] [28] [29], and are still widely studied [4][5]. The reason is to use robots in industry applications, engineers have to design various grippers [6] to adapt to different tasks and objects. Recent development in robot hand changers has two trends. The first is developing automatic tool changers for mobile manipulators. Some of them are electro-mechanically actuated, like the one presented in [7]. Some others are passive, like the one presented in [8]. Which used passive mechanisms actuated by host robots. Other than the changers, some studies design interfaces for robot end-effectors. An example is the da Vinci Surgical Research Kit [9]. The idea is to set an adapter between the tool and the original end-effector. A fingertip changer [10] shares the similar idea. The aforementioned studies all provide effective ways to change hands for robots. However, though those systems can provide reliable and precise fixing as well as connection, the efficiency of the exchanging process is still a problem. Also, the tools are adapted for specific end shapes, and the peripheral equipment is indispensable, which restricts the potential applications.

1.4 Manipulation Using Tools

Robotists always take inspiration from human behavior. Human beings can leverage tool to solve different manipulation problems. Human morphology and brain are flexible and adaptive specifically to improve our performance in-hand manipulation and fabricating better tools that contribute to daily work. Humans evolved to use naturally occurring tools and to fabricate better tools, and then covered with these tools [30] [11]. Not only humans but also primates and some birds can use tools for foraging [31] [32]. This give us all the more reason for seeing the significance of tool use for object manipulation.

Human tools mainly include two categories: manumotive tools and powered tools. [pic]Manumotive tools are powered by human hands, they transit the motion of hands (squeezing or stretching) into various motion output on the tooltips. The scissor, tweezer, and plier are representative manumotive tools. [pic]Powered tools are always equipped with a power supply and driven by a power-machinery, such as the electrical motor or the pneumatic actuator. They can be designed with various embedded transmission mechanisms for functional motions. The common powered tools are such as electrical/pneumatic screwdrivers, vacuums, and magnet grippers.

The tool designing on one hand considers the functionality, while on the other hand takes the hand morphology and the grasp behavior into account from the view of ergonomics. [Zoom in of the handles of scissors, driver, e-driver]. It stands to reason that anthropopathic hands are capable to use all the tools designed for human beings. However, considering the aforementioned problems of cost and difficulties on planning and control, deliberately employing the anthropopathic hands to use the tools is not an effective method. The optimal gripper candidate from the viewpoint of economy and stability is the two-finger parallel grippers. They are also the most widely installed grippers in industrial automations and robots [33]. A two-finger parallel gripper requires only one degree of freedom, thus, is compact and cheap. One the other side, it can only exert a simple parallel gripping motion, leading to limited functions. Therefore, it will be a promising technology to use tools to extend the functionalities of two-finger parallel gripper. Manumotive tools are in-hand manipulated while being held by human hands. The human oriented manumotive tools consider less about the grasp features of robotic grippers. Thus, they are inapplicable for two-finger parallel grippers. Powered tools, however, can be easily used by two-finger parallel grippers. When using them, the gripper can be viewed as a coupling for reconfiguration. After gripping the tool, namely the robot reconfigurates it's end-effector. In the operation, the robot needs only to move the tool to a goal pose. Thus, the tool use problems are simplified into a pick-move motion. Of course, the two-finger parallel grippers are still hard to directly use the powered tools designed for human beings as the design of their comfortable handles. Two-finger parallel grippers exert a strict parallel constraint on the grasped objects. The essential condition for holding an object is the existence of the parallel contact pairs on the object surface. The problem is also empirically solvable by reshaping the tool shell [34]. But, the powered tool always needs the cables or tubes for power supply and control, which cause unignorable problems. These cables are soft and deformable, leading to unpredicted configurations in the operation process. They may collide with the surrounding and may also bind robots, and even drag the robots until protective stop in a worst case. Daniel et al. [35] proposed to use an assistant robot to drag the cable to a position without interference corresponding to the planned position of the objective tool. They further developed to use two dual-arm robots, namely four arms, to manipulate the tool and cable [36]. The multi-robot cooperation even enables the tailed tool to be handover. However, assigning four robots to manipulate a single tool is too costly. The ultimate solution for avoiding the impact of the tailed cables is to fully remove the cable. Thus, we combine the features of the manumotive tool with the powered tool to design the tools that can be powered and controlled by a two-finger parallel gripper while being held by the gripper.

1.5 Mechanical Tools for Two-Finger Parallel Grippers

The mechanical tools can be viewed as the mechanisms that transmit the gripping force and convert the motion of the grippers. The function of a parallel gripper thus is not limited by the intrinsic grasping configuration. Simply, the gripper can use a clamping tool to pick tiny objects that are much smaller than the original finger pads. The clamping tool transmits the parallel gripping of the gripper to the parallel gripping on the tooltips. Using a similar mechanism, we can design the tool with large pads on the tooltips and a wider grasp range. Therefore, the gripper can also handle large objects whose dimensions exceed the original grasp range. Instead of grasping, we can also design the tools with different functions, such as shearing, twisting, and screwing.

The features of the designed tool are: (i) The tool is mechanical and is only manipulated and actuated by robotic grippers. (ii) The tool can be designed with various tooltips adapted for different tasks. (iii) The tool can be placed at an arbitrary pose in the workspace, and be recognized, grasped, manipulated, and used by parallel robotic grippers.

In the following part of this section, we will explain the difficulties and challenges of designing and using mechanical tools for two-finger parallel grippers, and discuss the contributions of this thesis on this topic.

1.5.1 Mechanism Design and Structure Optimization

It is challenging for a two-finger parallel gripper to hold and control the tool as the gripper has only one parallel motion degree of freedom and has no specific jigs on the finger pads. Both the firmly holding and force output rely on the gripping force. The designed mechanism should allow a deformation that caters to the parallel gripping motion and also exerts resistance force for holding. Importantly, the mechanism should be capable of transmission from parallel motion into various motions. This thesis focuses on achieving parallel-to-parallel transmission and parallel-to-rotation transmission. The mechanism designs are based on the parallel four-bar link mechanism and the scissor-like mechanism, respectively. The parallel four-bar link mechanism contributes to the transmissions between the parallel motions. And, the rotating motions can be obtained by the rotating arms of the scissor-like mechanism while its structure gets extended or squeezed. To structure the tools, we need to consider the symmetry of the gripper motion and grasp configuration, the grasp position on the tools, and the stability of the tools in the operation. We use a pair of symmetrical parallel mechanisms to design the tools for parallel-parallel transmission. When held by the gripper, the tooltips are ganged to the fingerpads, thus, can strictly follow the parallel motion. And, we employ the C-SLMs to design the rotating tool. The design on one hand constrains the tool pads to move parallelly and symmetrically, while on the other hand constrains the rotation central axis on a fixed position. For resisting support force, we install torsion springs on the joints.

1.5.2 Planning and Control for Tool Use

The first problem is grasp planning. In the case of using the tool to grasp an object, the object should be firmly clamped by the tool while the tool is stably held by the gripper. The planner is required to consider the grasp constraints from the two parts. And, the method of reorienting the tool pose is indispensable as the initial tool poses may have no direct path to reach the pose for the task execution. Additionally, in the process of task operation, the interaction between the tool and the environment may force the robot to stop or may make the tool fall. Compliance control is required to offset the unexpected force interaction.

This thesis uses a model-based method to plan grasps. The planning starts from a known object mesh, samples the parallel contact pairs, and checks the stability and collision. The stability estimation is based on GWS method. We use a graph-based motion planning method to generate the paths to use the tool to grasp the object. Instead of directly bridging the robot configurations from the initial grasps to the goal grasps, we add the nodes of grasping the tool. And, we use the regrasp-graph to plan the regrasp paths to orient the tool, especially, we add the grasp constraints of the tool-control poses. The problem of interaction force intensively occurs on the screw fastening task using the rotating tool, the robot should follow the downwards motion of the screws while avoiding getting stuck. We use the hybrid force/position control on the robot to make the gripper can both exert torque on the tool axis and be adaptive in the other directions to offset the uncertain collision and slide.

1.5.3 Manipulation for Uncertainty Elimination

The tool use extends the manipulation ability, but also introduces much more grasp uncertainty. Uncertainty is a crucial problem to employ robotic manipulators for assembly tasks. Especially for autonomous manipulators that receive vision feedback and generate manipulation motion online, uncertainty is challenging to eliminate – They originate from a series of mutually coupled components like vision, control, contacts, etc. Overcoming them and achieving precise manipulation is tricky. Using the tools to grasp an object, the uncertainty on grasping the tools are accumulated to the overall uncertainty, leading to lower success rate.

In this thesis, we presents a tool with a shape of triangular corner fixture, and proposes an regrasp planning method to eliminate grasp uncertainty by using the tool as a regrasp intermedia. The tool, a Triangular Corner Fixture (TCF) is made by three inclined and mutually perpendicular plates. The inclined plates of the TCF form a gravity bucket that holds a dropped objects in stable states under gravity. In a real scenario, a robot picks up an object and releases it above the TCF. The released object will reach a stable state on the TCF. Then, the robot regrasps and moves the stabilized object to the target pose with reduced uncertainty. The robots can use the tool to eliminate the uncertainty of both the goal objects and the mechanical tools, making the accurate assembly successful.

Chapter 2

Related Work

This chapter introduces related research that inspire this thesis. Three topics are summarized: mechanism design, robotic manipulation of tool use, and the manipulation for uncertainty elimination. In the first part, mechanism design, we focus on the mechanisms for designing a high-performance end-effector, especially the designs that contribute to the force transformation and motion convention. In the part of robotic manipulation of tool use, we review the explorations of the reasoning and planning on tool use. In the third topic, we investigate the methods of the sensor-less manipulation and the placement estimation for eliminating uncertainty. Additionally, we compare our proposed method with the previous research and highlight our novelties.

2.1 Mechanism Design

Mechanism designing in robotics is an old problem that has been extensively studied in industry. The most notable reading materials about are the books written by Monkman et al. [37] and Wolf et al. [38]. They not only discussed the mechanisms but also the actuation system. Compared to them, our focus is on the mechanical design part. We proposed to actuate our tools using the force exerted by the robotic gripper.

2.1.1 Parallelogram and Elastic Component

For the clamping tool, our design is based on parallelograms, which is a popular and widely seen mechanism in robotic gripper design. For example, Hassan et al. [39] presented a novel gripper for "pick and place" tasks. One of their multiple fingers was active, and was driven by a motor via a four-bar mechanism. Kocabas et al. [40] presented a one DOF gripper for power grasping. It consisted of a spherical symmetrical parallelogram to envelope objects. Triyonoputro et al. [24] and Nie et al. [25] developed a double jaw hand for grasping and assembly. The inner and outer grippers were made by four parallelograms that could work together to align and hold multiple objects.

Elastic components are widely used in underactuated hands to make up the insufficiency of actuators. For example, Laliberte et al. [20] and Birglen et al. [41] used elastic components to switch parallel grippers to a compliant mode and trigger power grasps. Ma et al. [42] used rubber connections between finger links as the elastic components to implement adaptive, shape-enveloping underactuated hands. Chen et al. [43] compared the adaptability of different underactuated mechanisms implemented with elastic components.

We use two symmetric parallelograms as the transmission mechanism of the tool and used the soft-finger contact model [44] to analyze the contact forces and torques between the robotic gripper and the tool as well as between the tool and the object to be grasped. The tool reopens after being released by taking advantages of the energy stored in some elastic components (torsion springs). The tool does not have an active actuation system. It is passively driven by robotic grippers.

2.1.2 Scissor-Like Mechanism and Ratchet

To develop the rotating tool that can output continuous rotation following the continuous close-and-open of a gripper, we use Scissor-Like Elements (SLEs) and ratchet mechanisms as basic elements, and also use elastic elements to provide resisting forces for holding the tool and producing torque output when a gripper releases the tool.

An SLE is a widely seen mechanical unit in scissors and scissor-like tools like pliers. A basic SLE element has two scissor arms that can freely rotate around a pivoting point [45]. This basic element has many variations. For example, Monkman et al. [37] and Khasawneh et al. [46] respectively extended basic SLEs to a pantograph for transmitting the grasp stroke of grippers. Maden et al. [47] reviewed Chained SLEs (C-SLE) used in planar or spatial structures. The C-SLE is a popular mechanism for robotic end-effector design. Yang et al. [48] presented a 2-DoF planar translational mechanism based on SLE-parallel – a mechanism consisting of two identical SLE limbs connected at two corresponding nodes by links. Corinaldi et al. [49] proposed a 3-DoF deployable gripper mechanism using SLEs and Sarrus linkages, which has a spatial structure to transmit motion symmetrically. Kocabas et al. [40] developed a 1-DoF spherical gripper mechanism consisting of spiral SLEs and linkages for power grasping of various shapes. Sanaani et al. [50] and Mehrabi et al. [51] used SLEs to design microgrippers. Instead of directly using conventional hinges, the authors studied to approximate their functions using the deformation of materials, making the design compact applicable to microdevices. Yuan et al. [52] compared SLEs with other transmission mechanisms like pulley blocks, lead screws and racks, and designed a cable-driven telescope. Other than robotic end-effector design, SLEs are also widely used in the structure of robot bodies [53] [54] [55] [56], exoskeleton [57], as well as general mechatronic devices to perform tasks like mobile pavilions, foldable stairs, collapsible doors, etc. [58] [59]. Besides the mechanism, the dynamic performance of SLEs is also widely studied. For example, Sun et al. [60] modeled the dynamics of a spatial deployable structure made of three SLEs using screw theory. Wang et al. [61] presented a method for solving the ordinary differential dynamics equations of deployable structures. Li et al. [62] studied the negative effects of joint clearance on SLE-based deployable structures' dynamic performance.

A ratchet allows continuous linear or rotary motion in one direction but locks opposite motion. The feature makes it a widely used transmission mechanism [63] [64]. In robotics, a ratchet is usually used as a locking device [65]. Li et al. [66] developed a hopping robot, in which a locked ratchet mechanism is released to trigger an energy storage mechanism. Geeroms et al. [67] developed an active knee-ankle prosthesis, in which a ratchet unit is used to lock the weight acceptance mechanism. As for the end-effector design, Abe et al. [68] designed a re-configurable end-effector for endoscopic surgery using a bending mechanism where a ratchet unit is employed to lock and release transmission following the bending conditions. Gerez et al. [69] and Sabetian et al. [70] focused on the development of underactuated grippers using ratchets. Besides, an electrostatic microgripper was presented in [71] by taking advantage of a ratchet's locking feature.

We use the above mechanical components to design a tool for parallel grippers. The actuation force of the tool is transmitted from the grippers. Two modified C-SLE (mC-SLE) are used to convert the parallel robotic gripping motion into oscillating rotation. A double-ratchet mechanism is connected to the two mC-SLEs to modulate the oscillating rotation into a unidirectional and continuous one. Like our previous tweezer tool [72], elastic elements are used to provide resisting force for robotic grasping. They are also used to stretch the tool and maintain the rotation when a robotic gripper is opened.

2.2 Manipulation of Tool Use

Using tools is an extensively studied robotic manipulation problem. With known models, developing robotic applications to use tools can be formulated and solved as an AI reasoning problem [73] [74]. The motion for using a tool can be planned by combined task and motion planning [75]. The task routine for using a tool is complicated, which, however, can be resolved into several subproblems [76] [77] like tool selection, tool recognition, constrained grasping and tool reorientation, etc. [78] [79] [80] [81]. Practical systems can thus be implemented in a divide-and-conquer way. Learning from demonstrations is also a popular approach to transfer the routine of using tools to robots. In [82], robots learned complicated manipulation like using a hammer through simulated demonstrations. In [83], human demonstrations were captured by pose-tracking and were then employed to learn how to identify and use tools. Raessa et al. [84] proposed a human demonstration-based method for teaching robots to use tools with special consideration of regrasp planning. Additionally, instead of demonstration, Xie et al. [85] presented the method of using video prediction for reasoning the potential robotic use of surrounding objects as tools in an improvisational way.

Besides the motions and task routines, many studies also focus on the various constraints and force problems. For example, Rachel et al. [86] studied the force constraints in the tool manipulation tasks. Toussaint et al. [73] studied the physical interaction between a tool and an object. Especially, the forces in a screw-fastening process are complicated [87], and improper control policies may lead to jamming, unqualified fastening torque, or cause damage to the screws and parts. For these problems, Nicolson et al. [88] discussed the maximum tilt angle of a screw and proposed an accommodation matrix-based control method to avoid jamming. Tan et al. [89] developed a Series Elastic Actuator (SEA) based electric actuator to implement hardware impedance in a screw-fastening process.

In this work, we study the forces and develop the manipulation policies for a robot to use the designed mechanical screwing tool to fasten screws. Our novelty is two-fold. First, we carefully study the contacts and forces between a robot hand and the tool so that the hand can stably hold and use it. Second, we design manipulation policies and policy-selection algorithms for tool recognition, adjusting grasping poses, exchanging tooltips, and detecting and completing screw fastening tasks. Hybrid arm control and gripper squeezing-stretching actions are combined to achieve both steady screwing and successful detachment after finishing a fastening task.

2.3 Manipulation for Eliminating Uncertainty

In this thesis, we propose to use the triangular corner fixture as a regrasp intermedia to eliminate the grasp uncertainty. This research relates to two aspects: sensorless manipulation and placement estimation.

2.3.1 Sensorless Manipulation

Like its name, sensorless manipulation means manipulating objects without using sensors. It relies on the mechanic and geometric constraints of a task to pose objects, and is simpler and more robust compared to sensor-based manipulation [90]. Sensorless manipulation is widely seen in automation lines to eliminate the uncertainty. The exemplary mechanism used for sensorless manipulation includes chutes, hoppers, bowl feeders and feed tracks, etc [91]. For robotic applications, Mason initially discussed the basic concept of sensorless robotic manipulation in [92]. After that, a variety of sensorless robotic manipulation approaches were studied. For example, Brost et al. [93] proposed using combined pushing and squeezing and flat finger pads to grasp an object with uncertainty. Nie et a. [94] and Hirata et al. [21] designed special-shape finger pads to align uncertain objects. Ha et al. [95] developed an automatic designer that finds finger pad shapes for robustly grasping various objects. Goldberg et al. [96], and Zhou et al. [97] used a sequence of parallel grasp actions to orienting and positioning uncertain objects to a specific pose. Maeda et al. [98] and Varkonyi et al. [99] developed caging-based methods to achieve in-hand manipulation and parts feeding, respectively. Erdmann et al. [100] and Schmidt et al. [101] used the active actions of palms and boundary walls to manipulate objects. Berretty et al. [102] and Akella et al. [102] studied the usage of passive settings like fences. Grossman et al. [103], Erdmann et al. [90], and Mannam et al. [104] respectively used robotic manipulators to move a tray attached to its tool center point. As the robotic manipulator moves, an object in the tray will be slid into a trihedral corner and stopped by the tray's walls. The final pose of the object can be determined by carefully planning and controlling the tray's tilting motion.

Similar to the conventional sensorless manipulation systems, our proposed method uses geometric constraints to hold objects. The objects are supposed to be dropped by a robotic manipulator onto a TCF and trapped by the tilted TCF inner surfaces under gravity. We assume that visual recognition is used to locate an object's initial pose, and allow recognition and other uncertainty. We develop algorithms to plan stable placement poses, estimate dropping poses, and plan grasp/regrasp poses to reduce uncertainty while taking advantage of the TCF's geometric constraints. Our process is fully automatic and applies to a wide variety of objects given their model information.

2.3.2 Placement Estimation

We consider a placement estimation as a two-part process. In the first part, we find a set of stable placement poses of the part. Then, based on the placement poses, we infer the dropping or releasing poses. The review of related work in placement estimation is carried out by inspecting the two parts.

The most fundamental problem of placement estimation is finding a stable placement on a horizontal plane. In this case, the object's stability can be determined by checking if its Center of Mass (CoM) projection passes through the convex supporting polygon [105] [106] [107]. As an extension to the fundamental problem, Wan et al. studied the placement planning on a tilted plane [108], a support pin [106], and arbitrary support structures [109]. Harada et al. [110] developed an algorithm to plan the stable object placement with non-flat contact considering the convexity of the paired contact surfaces. They assumed that the friction force is large enough to prevent sliding. The placement stability of rigid bodies and assemblies considering frictional contact was discussed in [111] [112]. Contact Wrench Space (CWS) was widely used for stability estimation. The radius of a maximum inscribed sphere in the contact wrench cone indicates how much external wrench or inertial wrench a grasp can tolerate. It can be used to evaluate the grasp qualities and find optimum grasp configurations [113] [114] [115] [116], and can also be used to estimate the stability of structures [117] [118].

Dynamic dropping simulation is also widely used for placement estimation [109] [119]. However, to assure the reliability of the simulated results, various parameters need to be tuned, and repeated examinations must be performed, which makes the methods less credible and time-consuming. For this reason, many researchers studied fast alternatives for dynamic simulation. For example, Kriegman and David [120] proposed an algorithm that computed a maximal capture region of the desired stable pose in the configuration space where the object pose would converge into a desired one. Jorgensen et al. [121] presented to generate drop regions for stable poses and discussed two methods, the largest enclosing ellipsoid computation and the kernel density estimation to determine optimal drop poses from them. Varkony [122] provided a statistics-based prediction method for estimating the resting poses of the dropped parts. Fekula et al. [123] used a similar method to perform the estimation, and based on the reasoned stable poses and the rendered top view images of them, they further positioned the objects using a vision-based method. Baumgartl et al. [124] developed a fast placement planner, which is capable of computing a stable position and orientation for a dropped object in complicated environments. In addition, learning-based methods also became popular for placement estimation and handling the uncertainties in manipulation processes. Lu et al. [125]

proposed to train a probabilistic graphical model as a classifier to predict the appropriate grasp types (power grasp or precision grasp). Li et al. [126] developed a deep network that uses a single depth point cloud to estimate the pose of an articulated object. Newbury et al. [127] used two Convolutional Neural Networks (CNNs) to estimate both the placement rotations and stabilities and obtain the human-preferred object placements and orientations. CNNs are also well used to estimate the grasp configurations [128] and predict the grasp qualities [129] as well. Feng et al. [130] used a Support Vector Machine (SVM) and a Long Short-Term Memory (LSTM) model to analyze the features of tactile sensors to detect slip and unstable grasps.

In our proposed method, a TCF is used to hold the dropped object and constrain its final configuration. We first find the SPPs on the tray corner considering the geometric constraints at the contact. Then, we use analytical and learning methods to obtain the DDPs of the objects that lead to the found SPPs. We compare the performances of the different estimation methods to understand the advantages and disadvantages.

Chapter 3

Clamping Tool

This chapter elaborates the clamping tool in this section. We discuss the details of the design, including the kinematic structure, the analysis and optimization of grabbing force and sizes, and the consideration of stable placements, recognition, pose adjustment, and working poses. We carry out experiments to analyze the performance of the design, as well as develop a robot system that uses the tools with different tips to pick up various objects. The experiments and analysis show that the mechanical tool is a flexible alternative to tool changers and finger-tip changers. With the help of visual detection and motion planning algorithms, robots are able to automatically recognize and use the tool to perform a wide range of tasks.

3.1 Design and Optimization

This section presents the details of design and optimization, including the kinematic structure, the optimization of forces and sizes, as well as the variation in tooltips.

3.1.1 Kinematic Structure

The tools designed for human hands usually have a rotational joint, as shown in Fig.4.1(a). The reason is that the rotational grab formed by the thumb is the main synergy of human hands [131], as shown in Fig.3.1(a). Likewise, a tool designed for parallel robotic grippers (Fig.3.1(b)) is best to have a parallel mechanism to cater to the parallel motion of the robotic gripper.

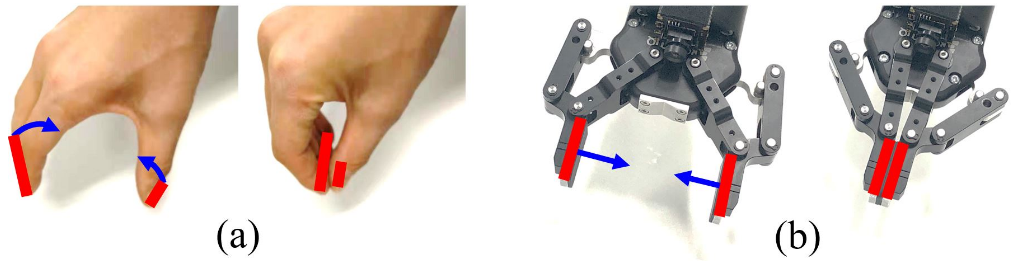

Figure 3.1: (a) The main synergy of a human hand. The thumb and the remaining fingers form a rotational grab. The tools designed for human hands thus usually have a rotational joint. (b) The motion of a parallel robotic gripper. The tool designed for it is best to have a parallel mechanism.

An intuitive idea to implement parallel motion is to use sliding rails. Linear springs may be attached to the rails to help return to the initial state after releasing. Fig.3.2(a) illustrates the idea. This idea is easy to understand, but is difficult to assure stable parallel motion. Fig.3.2(b) shows the free body diagram of the intuitive mechanism. To meet the momentum equilibrium, equation $F_A d_A - F_B d_B = 0$. That is, d_A and d_B must equal to each other. To assure a stable parallel motion, the contact can only be applied at the center of the two springs, which severely decreases the possible grasp configurations and increases the difficulty of automatic manipulation planning.

Instead of the simple sliding rails, we design the tool by using two symmetric parallelograms, as shown in Fig.3.2(c) and Fig.3.2(d). The two parallelograms allow the force from robotic grippers to be evenly distributed to the joints, and could therefore better assure stable parallel motion. Both of the two configurations in Fig.3.2(c) and Fig.3.2(d) can provide parallel motion transmission. The configuration in Fig.3.2(c) is selected since the configuration shown in Fig.3.2(d) is less stable. The details will be explained in the force analysis subsection.

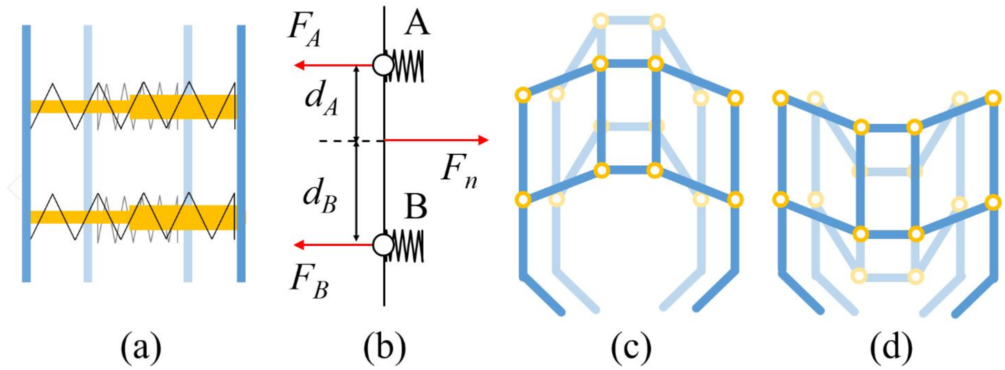

Figure 3.2: (a) The motion of an intuitive parallel mechanism made by sliding rails and linear springs. (b) The free body diagram of the intuitive mechanism. (c) A parallel mechanism made of two symmetric parallelograms. In this case, the base frame will move backward while the tool is closed. (d) An inversed design of (c). In this case, the base frame will move forward while the tool is closed.

Fig.3.3 shows the design. The jaw is fully opened and closed in Fig.3.3(a) and (b) respectively. The two parallelograms are symmetric and force the two tooltips to move in parallel. Four torsion springs are installed at joints P_1~P_4. The torsion springs are concentric with the rotating shafts. The ends of the torsion springs are fixed to the base frame and the angular links. The torsion springs provide resistance forces to prevent the tool from sliding out of the robotic gripper. They also provide forces to reopen the tool as the robotic gripper releases.

The torsion springs are installed with a pre-angle β, which is determined by the stopper crafted in the base frame. The torque exerted by a spring to an angular link is:

$$T_{spring} = \kappa(\beta + \Delta\theta), \tag{3.1}$$

where T_{spring} is the exerted torque. β is the pre-angle. κ is the elastic coefficient. $\Delta\theta$ is the rotational angle of the angular link. Choosing a proper β is an optimization problem. On the one hand, with the same $\Delta\theta$, a large β provides a large resistance force to robot grippers and hence provides larger friction to

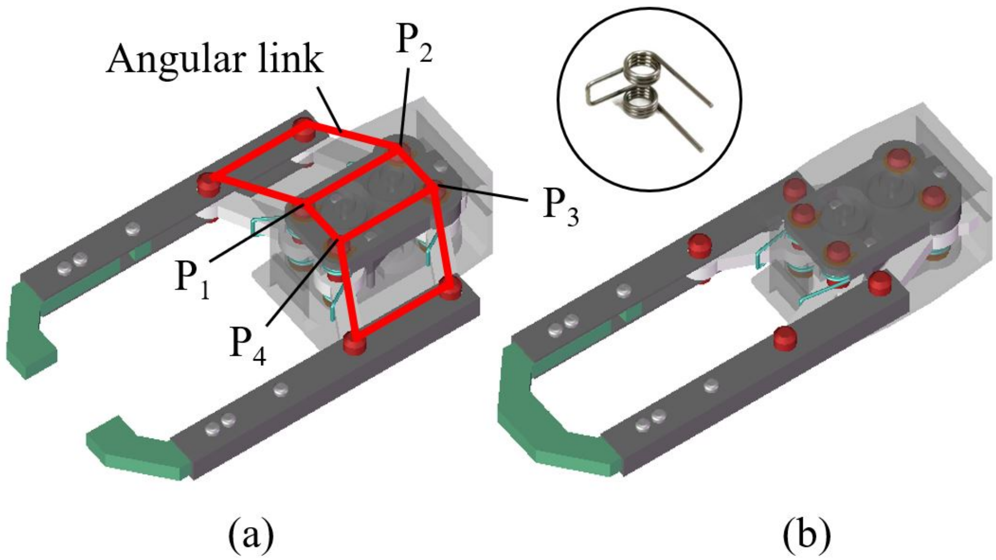

Figure 3.3: The designed mechanical tool. (a) The tool is completely open. (b) The tool is closed. Torsion springs shown in the circle are installed at joints P_1~P_4.

prevent the tool from sliding out of the robot gripper. It also leads to a shorter stroke of the robotic gripper to get the same transmitted force. On the other hand, if β is too large, the robot gripper has to exert a very large force to overcome the tension of the torsion springs. In the worst case, the tool may not be closed. The details of the optimization and force analysis will be discussed in the next subsections.

3.1.2 Force Analysis

In this subsection, we analyze the forces between the tool and a robot gripper to optimize the design. The subsection comprises two parts. In the first part, we analyze the condition for a robot gripper to firmly hold the tool as well as the relationship between robot grasping force and the resistance force from the torsion springs. In the second part, we analyze the maximum weight of objects that can be pick up by the tool.

Holding the tool

We model the contact between the robot gripper and the tool as a soft finger contact. Following [132] [133], the force and friction exerted by the robot gripper can be computed by:

$$f_{gripper}^2 + \frac{T_{gripper}^2}{e_{gripper}^2} \leqslant \mu_{gripper}^2 F_{gripper}^2, \tag{3.2}$$

where $f_{gripper}$ is the tangential force at the contact. $T_{gripper}$ is the torque at the contact. $F_{gripper}$ is the gripping force exerted by the robot gripper. $e_{gripper}$ is an eccentricity parameter computed as the ratio between the maximum friction and the maximum friction torque on the contact surface:

$$e_{gripper} = \frac{\mathtt{max}(T_{gripper})}{\mathtt{max}(f_{gripper})}. \tag{3.3}$$

The free body diagram when the tool is held by a robot gripper is shown in Fig.3.4. Here, α is the angle between the tool and the direction of gravity. It is called the tool angle. d_{com} is the distance between the grasping point and the center of mass *com* of the tool. By using the symbols shown in the figure and the soft finger contact model, we can get the condition to hold the tool as:

$$d_{com} \leqslant e_{gripper} \sqrt{\frac{4\mu_{gripper}^2 F_{gripper}^2 - G_{tool}^2}{G_{tool}^2 \sin\alpha^2 \mu_{gripper}^2 F_{gripper}^2}}. \tag{3.4}$$

When d_{com} equals 0, there is no torque at the contact. The robot gripper can hold the tool as long as $2\mu F_{gripper} \geq G_{tool}$. When d_{com} is not 0, the $F_{gripper}$ needed to hold the tool is a function of d_{com}, G_{tool}, μ_{tool}, and α.

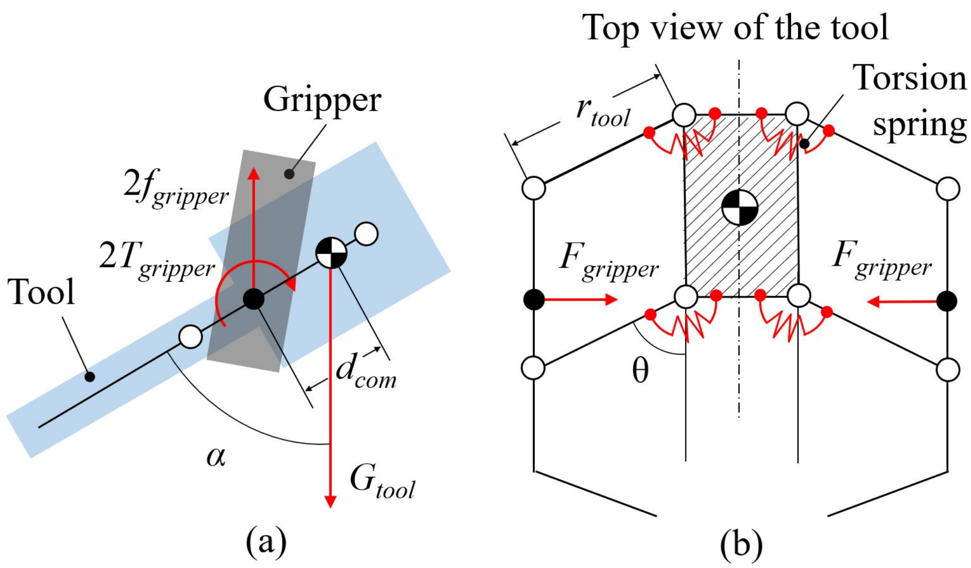

Figure 3.4: The free body diagram when the tool is held by a robot gripper. $F_{gripper}$ is the force exerted by the robot gripper.

When the tool is held firmly by the robotic gripper, the relationship between $F_{gripper}$ and the torque exerted by the torsional springs T_{spring} is:

$$F_{gripper} = \frac{G_{tool} \cos\alpha \tan\theta}{2} + \frac{2T_{spring}}{r_{tool}\cos\theta}. \tag{3.5}$$

The gripping force equals to the resistance force induced by the torsion spring and the gravity. The equation shows (*i*) $F_{gripper} \propto G_{tool}$ when $\alpha \in (-90°, 90°)$, and (*ii*) d is irrelevant and the resistance force is the same at any grasping point.

The first point further implies that when $\alpha \in (-90°, 90°)$, a larger gravity leads to a larger resistance force and hence a larger contact force (a larger friction) between the robot gripper and the tool. The implication reveals another advantage of the configuration in Fig.3.2(c) over the one in Fig.3.2(d). The force relations of Fig.3.2(d) is

$$F_{gripper} = -\frac{G_{tool} \cos\alpha \tan\theta}{2} + \frac{2T_{spring}}{r_{tool}\cos\theta}, \tag{3.6}$$

where $F_{gripper} \propto -G_{tool}$when $\alpha \in (-90°, 90°)$. In this case, the gravity of the base frame reduces the friction and makes the hold less stable. Thus, the configuration in Fig.3.2(c) is preferrable than the one in Fig.3.2(d) when $\alpha \in (-90^\circ, 90^\circ)$.

Grasping an object using the tool

Next, we analyze the maximum weight of objects that can be pick up by the tool. The contact between the object and the tool is also modeled using the soft finger contact.

The force exerted by the tool to the object could be computed as

$$F_{tool} = F_{gripper} - \frac{G_{tool} \cos\alpha \tan\theta}{2} - \frac{2T_{spring}}{r_{tool} \cos\theta}. \tag{3.7}$$

Using the soft finger contact model shown in equation (4.1) and (4.2), the friction coefficient μ_{tool} at the contact between the tool and the object must meet

$$\mu_{tool} \geqslant \frac{G_{obj}}{2F_{tool}} \sqrt{1 + \frac{r_{obj}^2}{e_{tool}^2}} \tag{3.8}$$

to assure the object could be stably clamped by the tool. Here, e_{tool} is the eccentricity of the soft contact between the tooltip and the object.

When equation (3.8) is met, the maximum weight of an object that can be pick up by the tool can be computed as follows. The meanings of the symbols are noted in Fig.3.5.

When the force and torque are balanced, we get:

$$2f_{tool} - G_{tool} - f_{obj} = 0, \tag{3.9}$$

$$G_{tool} d_{com} \sin\alpha + 2T_{tool} - f_{obj} d_{tooltip} \sin\alpha = 0. \tag{3.10}$$

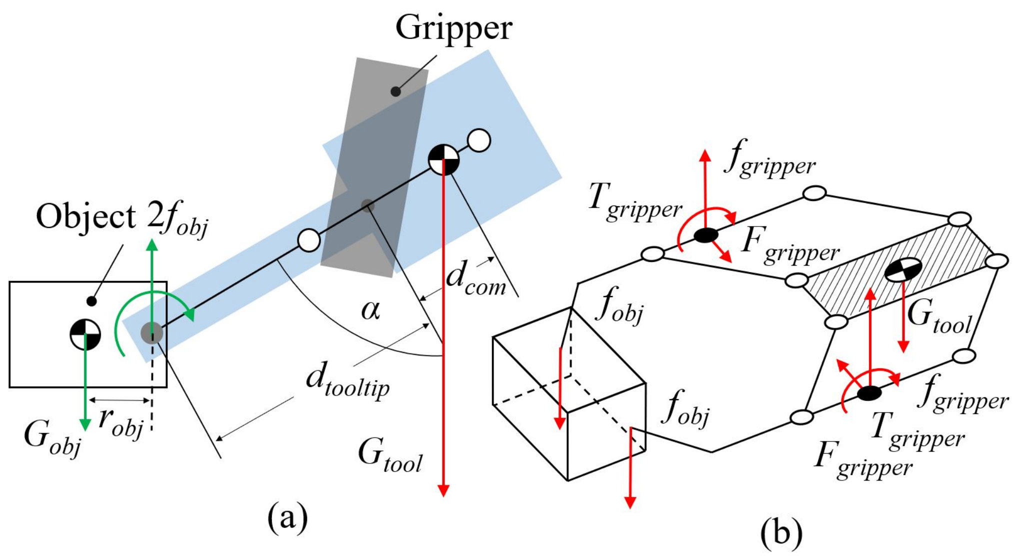

Figure 3.5: The free body diagram when the tool is holding an object. $F_{gripper}$ is the force exerted by the robot gripper.

The maximum weight of the object to be held can be computed using equations (3.9), (3.10), and the boundary condition in equation (4.1) as:

$$a = 1 + \frac{d_{tooltip}^2 \sin\alpha^2}{e_{gripper}^2}, \tag{3.11}$$

$$b = G_{tool}(1 - \frac{d_{tooltip} d_{com} \sin\alpha^2}{e_{gripper}^2}), \tag{3.12}$$

$$c = \frac{G_{tool}^2}{4} + \frac{G_{tool}^2 d_{com}^2 \sin\alpha^2}{4e_{gripper}^2} - \mu_{gripper}^2 F_{gripper}^2, \tag{3.13}$$

$$Maximum\ weight = \frac{-b + \sqrt{b^2 - 4ac}}{a}. \tag{3.14}$$

3.1.3 Size and Material Optimization

In this section, we discuss the optimization of the tool considering geometric constraints, maximum pickable object weight, and the materials of the tooltips.

We would like the tool to have a large stroke and compact size, at the same time, we hope it to be able to clamp a large load.

Geometric constraints

The dimension parameters shown in Fig.3.6 are used for optimization. Equa-

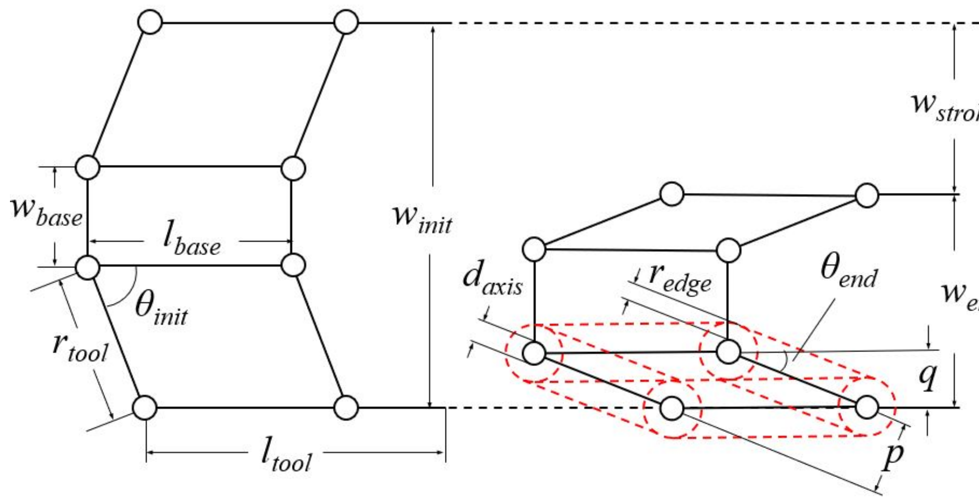

Figure 3.6: The dimensional parameters used for optimization.

tions (3.15) and (3.16) show the relationship among the width of the tool, the stroke of the tool, and the rotational angles of the angular link.

$$w_{init} = w_{base} + 2r_{tool} \sin \theta_{init} \tag{3.15}$$

$$w_{stroke} = 2r_{tool}(\sin \theta_{init} - \sin \theta_{end}) \tag{3.16}$$

Given a fixed w_{init}, w_{stroke} is expressed as:

$$w_{stroke} = \frac{w_{init} - w_{base}}{\sin \theta_{init}}(\sin \theta_{init} - \sin \theta_{end}). \tag{3.17}$$

Equation (3.17) shows that increasing θ_{init} and decreasing θ_{end} and w_{base}will enlarge the stroke w_{stroke}. When θ_{init} is 90°, θ_{end} is 0°, w_{base} is 0, w_{base}reaches to its maximum. However, the relationship between $F_{gripper}$ and θ shown in (3.5) tells that an overlarge θ_{init} will significantly increase the requirements on the grasping force $F_{gripper}$ and make the tool hard to be compressed. If θ_{init} reaches 90°, the tool can never be used. Also, if $w_{base}$is 0, the base will disappear. In this case, since the links have a width in the real world, w_{base}should meet:

$$w_{base} \geqslant d_{axis} + 2r_{edge}. \tag{3.18}$$

For the same reason, θ_{end} cannot be 0°. Its minimum can be calculated considering the radius of the joints and the width of the links. The red dot lines in Fig.3.6 show the situation when θ_{end} reaches its minimum. In this case, the parallel link touches the base frame. The minimum θ_{end} can be computed using Equation (3.19). p should meet equations (3.20) and (3.21). h should meet equation (3.22). Otherwise, the links will overlap with each other.

$$\theta_{end} = \arcsin \frac{q}{r_{tool}} \tag{3.19}$$

$$q = d_{axis} + 2r_{edge} \tag{3.20}$$

$$p \geqslant l_{base} \sin \theta_{end} \tag{3.21}$$

$$l_{base} \geqslant r_{tool} \cos \theta_{end} + \tan \theta_{end}(d_{axis} + 2r_{edge}) \tag{3.22}$$

Maximum pickable object weight

The maximum weight that the tool can pick follows equation (3.11)-(3.14). The sum of $d_{tooltip}$ and d_{com} is the parameter we would like to optimize. It linearly increases with l_{tool}. Meanwhile, d_{com} must meet equation (3.4) and (3.5) to allow the tool to be held stably by the gripper, that is, the maximum value of d_{com} is:

$$d_{com} = e_{gripper}\sqrt{\frac{4\mu_{gripper}^2(\frac{G_{tool}\cos\alpha\tan\theta}{2}+\frac{2T_{spring}}{r_{tool}\cos\theta})^2 - G_{tool}^2}{G_{tool}^2\sin\alpha^2\mu_{gripper}^2(\frac{G_{tool}\cos\alpha\tan\theta}{2}+\frac{2T_{spring}}{r_{tool}\cos\theta})^2}}. \tag{3.23}$$

By combining it with equations (3.11)-(3.14) and approximate the sum of $d_{tooltip}$ and d_{com} using l_{tool} , we can formulate the maximum weight as a function of l_{tool}, r_{tool}, α, and some other variables. The complete form of the formulation is complicated and is not listed in the paper. Interested readers may deduce it by replacing d_{com} using l_{tool} in equations (3.11)-(3.14) using equation (3.23) and l_{tool}-equation (3.23).

To analyze the equation, we assume the following values for the other variables and focus l_{tool} and α. We set the maximum gripping force of the robotic gripper to be 80 N, the θ angle when the tool is picked up to be 45°, the weight of the tool to be 3 N, and the coefficient of the torsional spring to be 3.5 $N \cdot mm \cdot degree$. Under the assumption, the maximum weight changes with respect to l_{tool}, r_{tool}, and α follows the 3D plots in Fig.3.7. The surface shows that to bare a large load, it is advisable to make l_{tool} as short as possible. r_{tool} is not an important parameter. It can be simply determined considering the geometric constraints.

In practice, l_{tool} is limited by several factors as follows. (*i*) l_{tool} needs to be larger than l_{base}. (*ii*) There should be some space to install the anti-collision units. (*iii*) Some tooltips are thin and longer. Considering these factors, in our implemen-

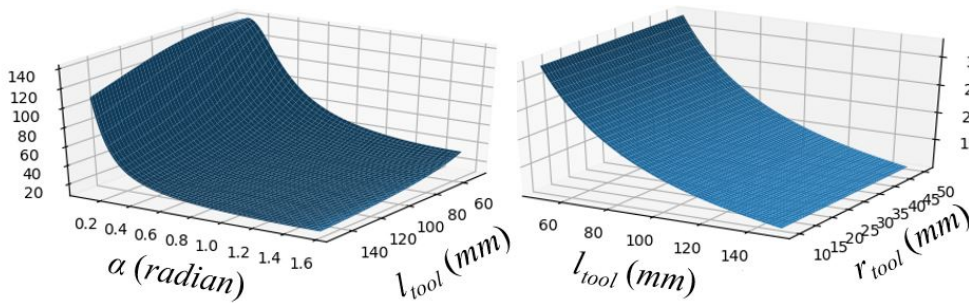

Figure 3.7: Left: Changes of maximum object weight with respect to l_{tool} and α. r_{tool} is fixed to 30 mm. Right: Changes of maximum object weight with respect to l_{tool} and r_{tool}. α is fixed to 90°. r_{tool} has little influence on the shape of the 3D surface.

tation, l_{tool} is chosen to be

$$l_{base} + \text{length}(anticollision\ unit) + \text{length}(finger\ tip) \approx 2.5 l_{base}. \tag{3.24}$$

Materials of the tooltips

Equation (3.8) shows the limitation on the friction coefficient of the tooltip. By replacing the F_{tool} using equation (3.7). The minimum friction coefficient can be written as a function of α and several other miscellaneous variables. We assume the following values for the miscellaneous variables. The maximum gripping force of the robotic gripper is set to be 80 kgf. The θ angle when the tool is picked up is set to be 45°. The weight of the tool is set to be 3 kgf. The coefficient of the torsional spring is set to be 3.5 $N \cdot m \cdot degree$. r_{tool} is set to be 30 mm. Then, the minimum friction coefficient is

$$\mu_{tool} \geqslant 0.0075 G_{obj} \sqrt{1 + \frac{r_{obj}^2}{e_{tool}^2}}. \tag{3.25}$$

Under the following conditions: (i) The contact between the fingertip and the object is a spherecial soft contact with radius 3 mm, (ii) the weight of an object is less than 20 N, and (*iii*) the *com* of the object is less than 5 *mm* from the tooltip center, the minimum friction coefficient must be larger than 0.396.

3.1.4 Variation in Tooltips

In addition to the mechanical design, we can make different tooltips for different tasks. A robot may determine which tool to use according to task requirements and using task and motion planning technique. This is different from the commercial grippers which require manually changing fingertips or using tool changers to replace the whole end-effector. The cost of a single tool is low, and there could be lots of tools for a robot to choose from. Some examples are shown in Fig.3.8.

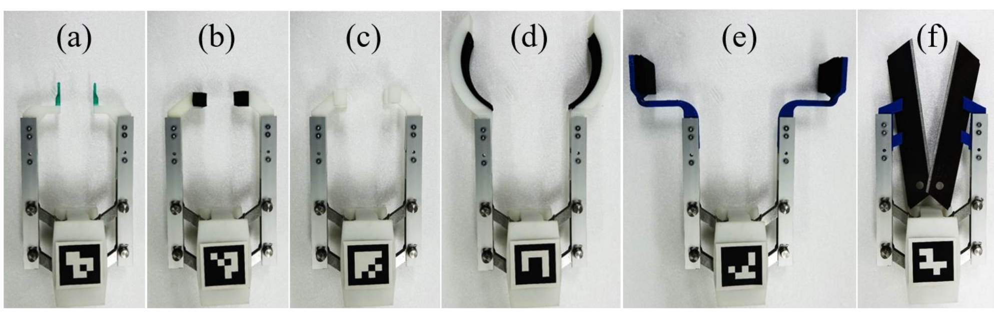

Figure 3.8: Tools with different tooltips. A robot may use planning to choose a tool following task requirements.

3.2 Using the Tool

When performing specific tasks, the tool is placed in an arbitrary pose in the workspace. A robot identifies the tool using AR markers and grasps it using pre-planned grasp configurations. To use the tool, the robot should be constrained to grasp the tool in specific poses (working poses). When the pose of the tool makes it impossible or difficult to be picked up in a working pose, regrasp planning [134] may be employed to adjust the grasp configuration.

3.2.1 Working Poses

There are several pairs of parallel surfaces of the tools that can be stably grasped, but the tool can be used only when the sides of the parallel links are used as the contact surfaces. In addition, the tool angle α is expected to be within the range of $-90^\circ \sim 90^\circ$ to assure $F_{gripper} \propto G_{tool}$. The angle γ, which is defined as the angle between the hand and the tool (Fig.3.9(b.1)), is also expected to be within the range of $-90^\circ \sim 90^\circ$ to let the tooltip face "forward".

For the working poses with $\alpha \in (-90^\circ, 90^\circ)$ and $\gamma \in (-90^\circ, 90^\circ)$, we further analyze the most stable one considering the various soft penetration models like surface, punctual, linear, etc. The details are as follows. The $e_{gripper}$ in equations (4.2) and (3.4) can be further expanded using the Winler elastic foundation models as:

$$e = \frac{\mathtt{max}(T)}{\mathtt{max}(f)} = \frac{\int_S r\mu K u_i(r) dS}{\int_S \mu K u_i(r) dS}. \tag{3.26}$$

Here, K is the elastic modules of the foundation over the thickness of the soft finger pad. S is the contact area between the finger pad and the object. $u_i(r)$ is the depth of the soft penetration. r is the distance between a differential contact point and the center of the contact region.

$Ku_i(r)$ is determined by the soft penetration of a grasp. We model it using the 7 types shown in Fig.3.9(a.1~a.7). The upper-right corner of each small image

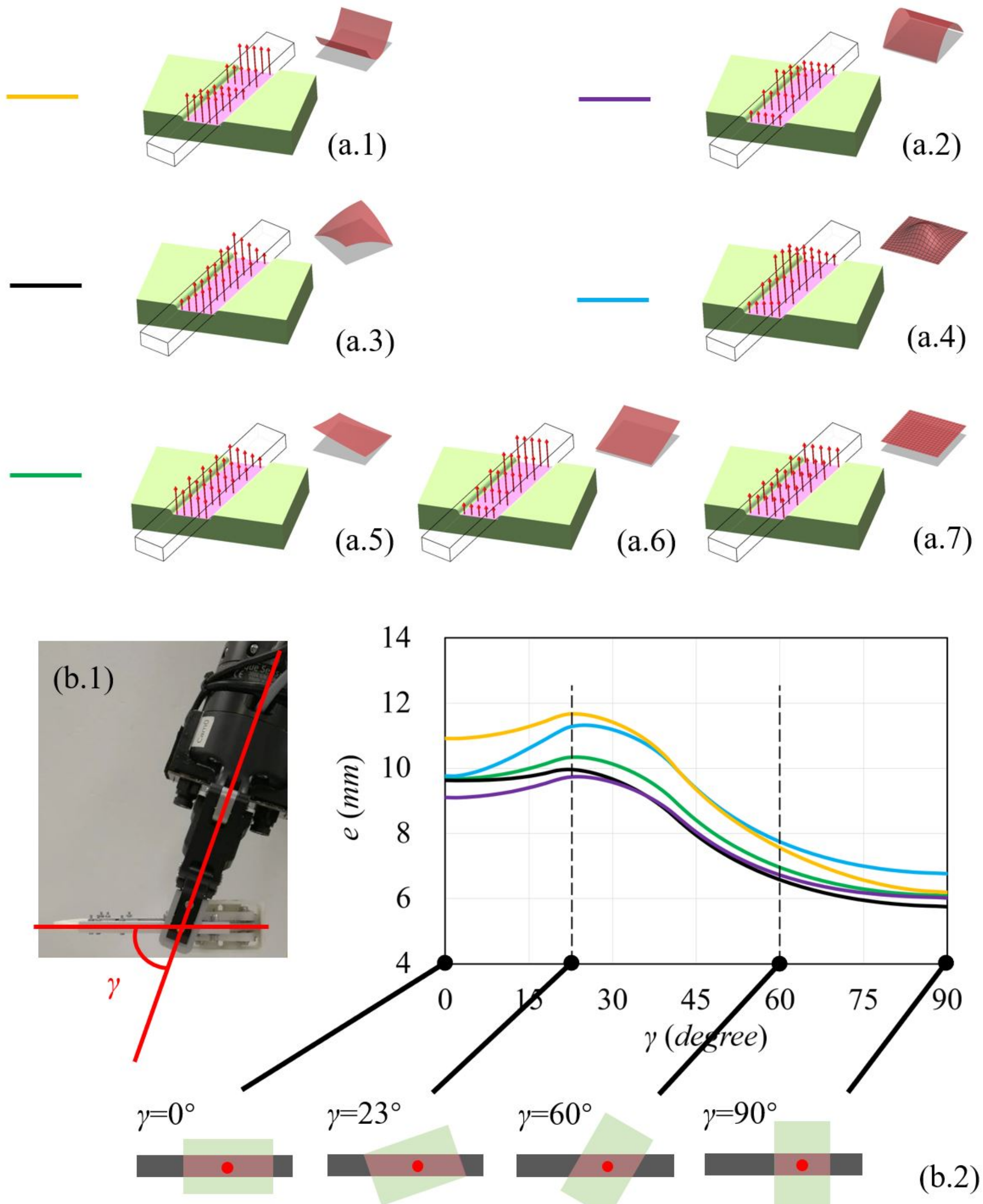

Figure 3.9: (a.1-7) The 7 soft penetration models we used to analyze the eccentricity and the most stable grasp. (b.1-2) The eccentricity e corresponding to the soft penetration models. Each curve in (b.2) shows the changes of e with respect to different γ shown in (b.1). Different colors indicate different soft penetration models.

shows the shape of the soft penetration using 3D surfaces. (a.1) is a model where the soft penetration is small in the middle line and increase as the contact position departs from the middle line. (a.2) is a model where the soft penetration is large in the middle and gets small as the contact position gets apart. (a.3) is a model where the soft penetration along the diagonal line is large and decreases as the contact position departs from the diagonal line. (a.4) is a Gaussian soft penetration model where the maximum penetration is in a middle point, and decreases as the contact position gets apart. (a.5) and (a.6) have maximum penetration at one corner. (a.7) is a uniform model where all soft penetrations on the contact area are the same. The eccentricity e corresponding to these soft penetration models are shown in Fig.3.9(b.2). Each color corresponds to one of the models. The changes of the curves show the changes of e at different γ.

These 7 soft penetration models cover various contact types like surface (a.1, a.5, a.6, a.7), punctual (a.4), and linear (a.2, a.3). The results show that the eccentricity reaches its maximum value at around 23°, with little dependency on the penetration models. Grasping the tool with a +23°/-23° tilting angle is most stable and is the best working pose. The reason is probably the contact area reaches its maximum size around this angle. The size of the contact area is dominant over the other soft contact parameters.

3.3 Experiments

A dual-arm UR3 robot is used to conduct the experiments. The dual-arm robot consists of two UR3 robots mounted symmetrically with 45° to a body frame. Two Robotiq F-85 grippers are installed to the two robots as the robotic grippers. An ELP-USBFHD06H-L36 skewless HD web camera is mounted to one side of the Robotiq F-85 gripper for visual detection.

3.3.1 Maximum Weight of an Object

First, we perform experiments to test the maximum weights of an object that can be picked by the tool. DynPick force sensor (Fig.3.10) is used for measurement.

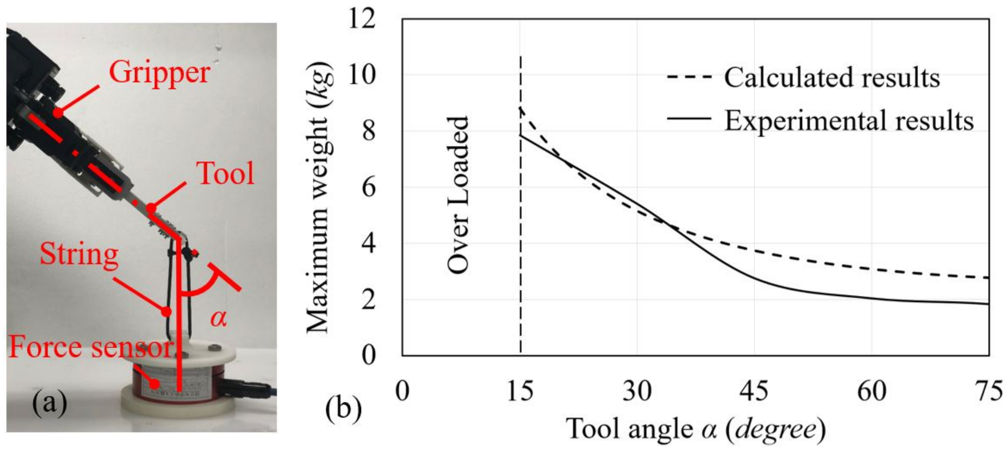

Figure 3.10: (a) The set up to measure the maximum weights of objects that can be picked by the tool. The peak force measured by the force sensor before the tool moves is recorded as the maximum weight of an object that can be picked by the tool. (b) The maximum weight that the tool can pick at different α.

The sensor is fixed to a table. A string is used to connect the sensor and the tooltips. The robot gripper holds the tool and drag the string up vertically until the tool is moved. The peak force measured by the force sensor before the tool moves is recorded as the maximum weight of an object that can be picked by the tool. The test is repeated with the tool angle α changing from 0° to 75°. To simplify the experiment and improve precision, the γ angle is set to 0°.

The results are shown in (b). The solid curve shows the changes of the maximum weight with respect to different α. The dash curve is the theoretical values computed using equation (3.11-3.14). The measured results are nearly the same as the theoretical analysis. The proposed design could pick up an object of 8 kg when the angle between the tooltip and the gravity direction is 15°.

3.3.2 Using Various Tooltips

Second, to test the performance of the various tooltips, we conducted experiments to pick up small objects like screws and washers, and large objects like cans and boxes, as well as using a scissor variation to cut a piece of paper. These objects are difficult to be handled by only the Robotiq F85 gripper.

Fig.3.11 shows the experimental results. In (a), a thin tooltip is used [25] to pinch or stretch small objects like the screws and washers (diameter of the screw: 2 *mm*; diameter of the washer hole: 5.5 *mm*). In (b), the robot picked up a bolt in a tray by taking advantages of its thin arms. The tooltip, in this case, is bigger to stably hold the bolt (diameter of the bolt: 8 *mm*). In (c), a widely open tooltip is used to pick up a tissue box whose width is larger than both the maximum stroke of the robotic gripper and the maximum opening width of the parallelogram. (width of the box: 90 *mm*). In(d), a circular tooltip is used to pick a cylindrical can (diameter of the can: 66 *mm*). In (e), the tooltip is changed to a pair of knives to perform cutting tasks.

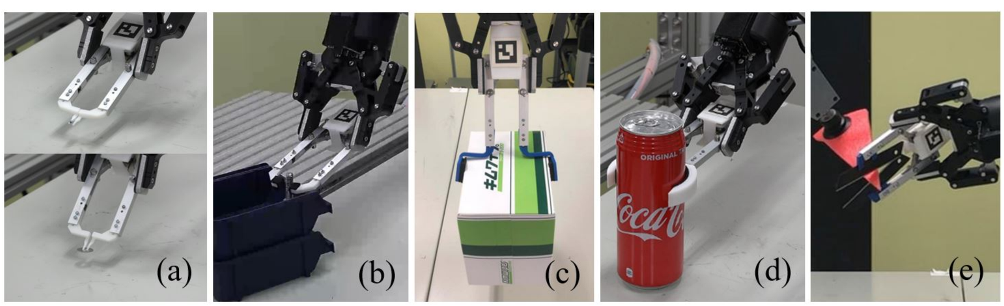

Figure 3.11: Using different tooltips to pick up various objects. (a) Small objects like screws and washers. (b) A bolt in a narrow tray. (c, d) Large objects like boxes and cans. (e) Using a scissor variation to cut a piece of paper.

3.3.3 Automatic Recognition and Planning

Third, we program the robot to use the tools with different tooltips to perform various tasks with regrasp planning. The results are shown in Fig.3.12. Regrasp planning is used to adjust the pose of the tool. The robot can recognize the tool, plan a regrasp motion to adjust the pose of the tool using placement-based regrasp or handover-based regrasp, and plan a motion to use the tool. Together with the automatic recognition and planning, the tool can be used flexibly without requirements on the power supply, vacuum supply, or delicate mechanism and control. Readers may refer to the video attachment for more details.

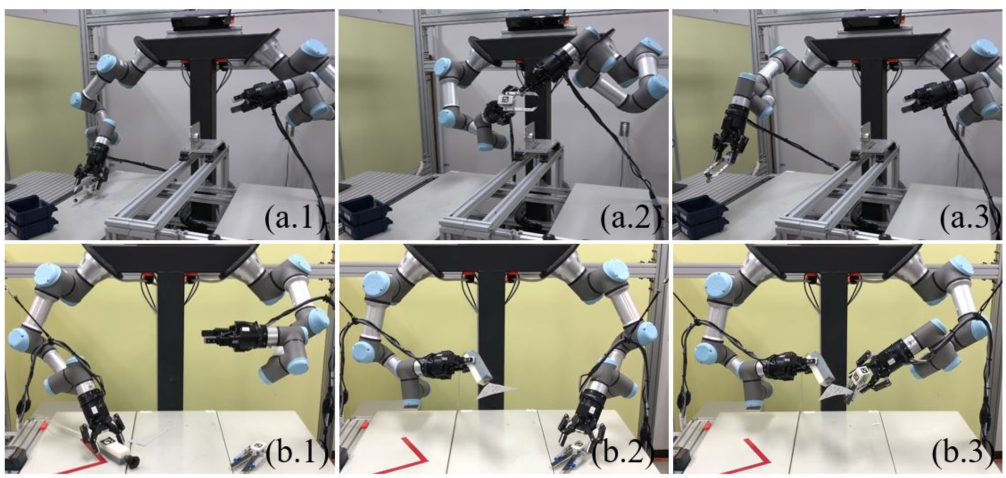

Figure 3.12: A robot using the tools with different tooltips to perform various tasks with regrasp lanning.

3.4 Summary

This chapter presented the design of a mechanical tool for robots with 2-finger parallel grippers. The tool can extend the function of the robotic gripper without additional requirements on tool exchangers or other actuators. It is general, dose not require power or air supply, and can be used by any robots with 2-finger parallel grippers. Experimental results showed that intelligent robots can use the tool through vision and planning to perform complicated tasks.

Right now, the tool is specially designed for 2-finger parallel grippers. We limited it to 2 fingers since the two parallel finger pads are the same. It is simpler to deduce the formulae and analyze the contacts for two same finger pads. Despite the special design, the tool can be used by multi-finger grippers whose contact surfaces can move parallelly. However, in these cases, the contacts at the two parallel sides are different. It is more complicated to analyze the friction forces and torques. We will study it in our future work.

Chapter 4

Rotating Tool

In the last chapter, we discuss the clamping tool for a robot hand to pinch various sized objects. The tool reinforces a robotic gripper by extending the parallel motion. Following a similar conception, we in this paper present the rotating tool which converts the parallel motion of a robotic gripper to a continuous rotation, as shown in Fig.4.1. The tool's essential structure is based on Scissor-Like Elements (SLEs) and a double-ratchet mechanism. The SLEs form the mainframe of the tool. They help to keep a fixed rotation center during transmission. To make the structure compact, the holding pads are optimized to have a curved profile to reduce the SLE arms' length. The double-ratchet unit is installed concentrically with the pivoting center of the SLEs. It is made of two ratchets with reversed locking directions. The two ratchets are fixed to the arms of the front and back SLEs, respectively. A central shaft connects them. Torsion springs are installed at the SLE joints to provide enough resistant pressure for both being held by robotic grippers and stretching the tool.

In the remaining part, we present the tool's design details, including the related optimization for dimensions, effective stroke lengths, and contacts and forces to achieve stable grasping and screwing. Besides the design, we also present the manipulation policies for using the tool. The policies include visual recognition, grasping and manipulation, exchanging tooltips, and detecting and completing screwing tasks. The developed tool produces clockwise rotation at the front end and anti-clockwise rotation at the back end. Various tooltips can be installed at both ends. With the policies' help, robots may exchange tooltips and switch the functional ends following the needs of specific

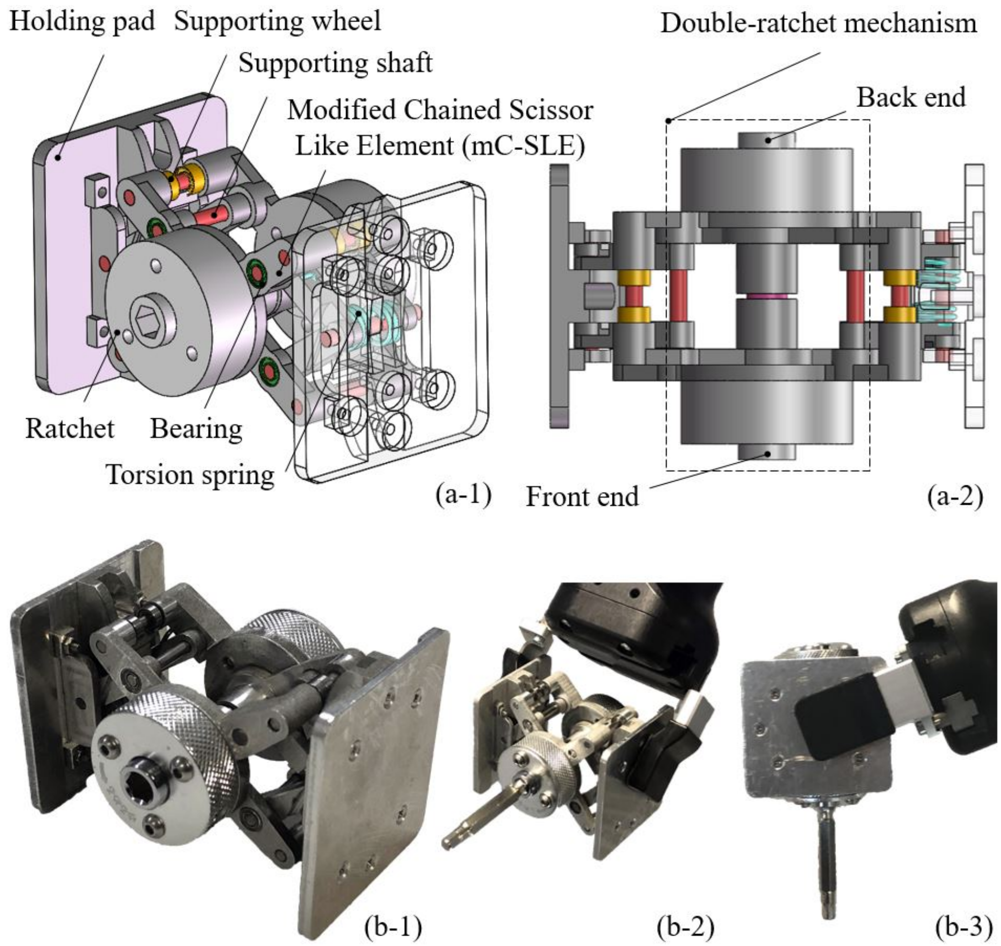

Figure 4.1: The proposed mechanical screwing tool. It employs a Scissor-Like Element (SLE) mechanism and a double-ratchet mechanism to convert parallel gripping motion to continuous rotating motion. (a.1,2) The CAD models of the design. (b.1) A prototype. (b.2,3) The prototype held by a parallel gripper.

fastening or loosening tasks. Robots may also reorient the tool using pick-and-place and handover, and move it to work poses. During screwing, robots can determine control policies following our proposed policy-selection algorithm, and successfully perform screwing, termination, and detaching actions. Experiments and real-world robotic applications are carried out to verify the tool's mechanical properties and demonstrate its robustness and usefulness.

4.1 Mechanical Structure

4.1.1 Scissor-Like Elements (SLEs)

Basic SLE and its problems

Fig.4.2(a, b) show a basic SLE. The rotation of the basic SLE induces the translational motion of $P_1P_2 \rightarrow P'_1P'_2$ and $P_3P_4 \rightarrow P'_3P'_4$, making the basic SLE a good candidate mechanism for our tool. The linear motion of *segment*s P_1P_2 and P_3P_4 affords the parallel gripping motion.

A shortcoming of the basic SLE is that the length of *segment* P_1P_2 (also *segment* P_3P_4) changes during the translation. They turn into longer *segment*s $P'_1P'_2$ and $P'_3P'_4$, making them not suitable to be held by fingers. Thus, to ensure a stable hold, some points on the SLE arms must be fixed. Fig.4.2(c) shows an intuitive solution used in a mini scissor lift. In this case, P_2 and P_4 are attached to two pads using rotational joints. P_1 and P_3 are free ends. As the two pads move close, P_1 and P_3 slide up to P'_1 and P'_3. The pads move in a stable linear motion and are meanwhile suitable to be held. However, this intuitive solution does not meet the requirements of a screwing tool. As the pads close, the pivoting joint O moves up to O', as shown in Fig.4.2(c). Screwing tooltips cannot be attached to the moving pivoting point, and further modification is needed.

Chained SLE (C-SLE) and the proposed modification

We propose to use a modified Chained SLE (mC-SLE) to solve the problems mentioned above. We chain one full and two half basic SLEs up to keep the po-

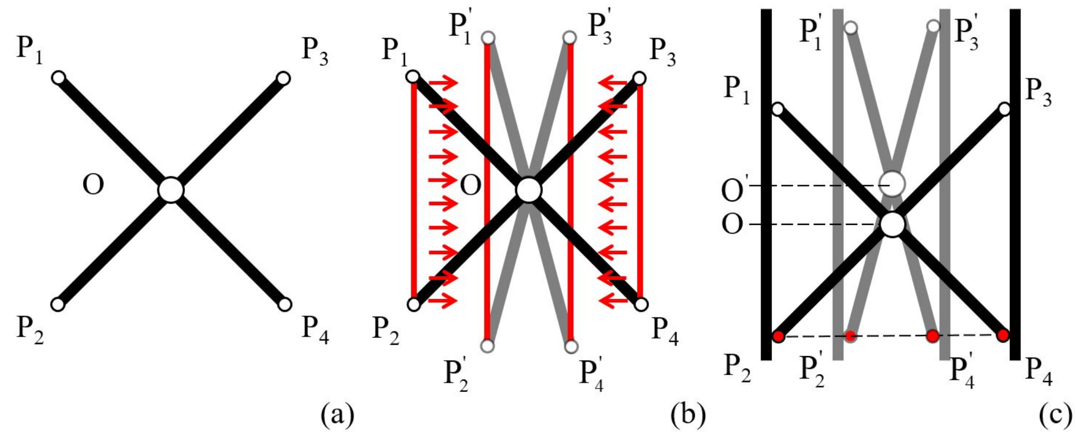

Figure 4.2: (a) A basic Scissor-Like Element (SLE). (b) The length of *segment*s P_1P_2 and P_3P_4 change with rotation. (c) An intuitive solution to implement graspable pads. P_2, P_4: Rotating joints; P_1, P_3: Free ends. O, O′: Pivoting joints.

sition of the pivoting joint fixed while the two pads close. Fig.4.3(a, b) illustrate the idea. In Fig.4.3(a), the blue links form a full basic SLE. The yellow links form two half basic SLEs. P_5 and P_6 are the rotational joints connected to the holding pads. When the mechanism is squeezed, the distance between P_5 and P_6 will decrease and the arms of the basic SLE will rotate around the pivoting joint O. Also, O is the center of *segment* P_5P_6, and P_5-O-P_6 keep co-linear all the time. The position of O will remain unchanged while a robotic gripper presses P_5 and P_6.

A drawback of the design shown in Fig.4.3(a) is that it cannot withstand an external torque as there are only point constraints at P_5 and P_6. The design collapses if the pressing forces are not exactly exerted at the points P_5 and P_6. To avoid this problem, we extend the arms of the full basic SLE for support. As shown in Fig.4.3(b), the cross H_1H_4-H_2H_3 is the full SLE. The H_1-H_5-H_2 and H_3-H_6-H_4 on the two sides are the two half SLEs. By extending OH_1 to P_1, OH_2 to P_2, OH_3 to P_3, and OH_4 to P_4, and using P_1-P_4 as the supporting joints, the mechanism can accept pressure at any positions on the two holding pads. The parallel

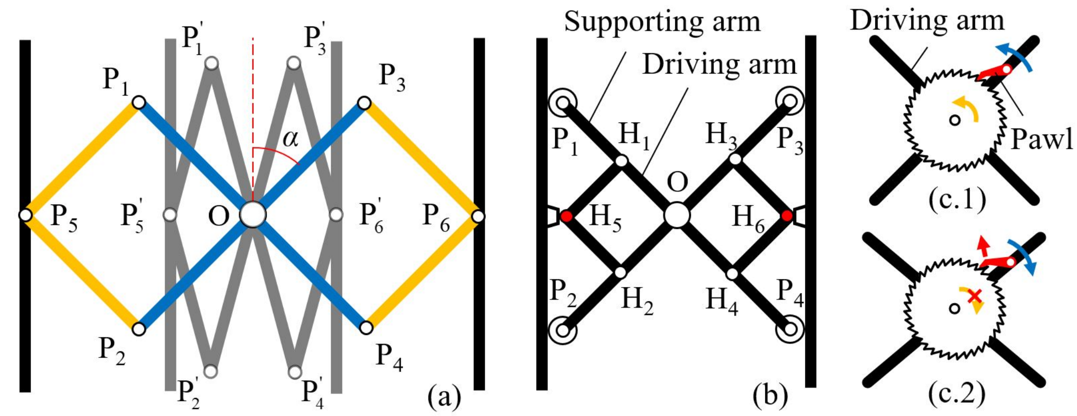

Figure 4.3: (a) The structure and motion of a kinematic SLE chain made of one full SLE (blue) and two half SLEs (yellow). The position of O remains stationary when being squeezed. (b) The proposed mC-SLE design. The OH_i ($i = 1, 2, 3, 4$) arms are extended to P_i to resist torques. (c.1,2) A basic ratchet is attached to the pivoting center and one arm of the mC-SLE.

motion of a robotic gripper can be converted into a rotational motion around O. P_1-H_5-P_2 and P_3-H_6-P_4 maintain collinearity during the rotation. Note that all the P_i ($i = 1, 2, 3, 4$) play the role of a free end. Supporting wheels are therefore installed on them to enable the free motion. The arms H_1P_1, H_2P_2, H_3P_3, H_4P_4 are called the supporting arms. They are symmetric and have the same length. The arms OH_1, OH_2, OH_3, OH_4 are called the driving arms. They are also symmetric and have the same length.

This modified C-SLE design is called mC-SLE. We install two mC-SLEs in parallel to hold the double-ratchet mechanism and realize continuous rotating motion. The details are presented in the next subsection after introducing ratchets.

4.1.2 Ratchet Mechanism

A single ratchet and its problems

The arms of the mC-SLE rotate back and forth with the open and close of the holding pad. Such motion does not meet the requirements of a screwing tool, where only a single-direction motion is needed. We use a ratchet to regulate the back-and-forth rotation into a single-direction one, as shown in Fig.4.3(c). A ratchet comprises a ratchet gear (or a rack with teeth) and a pawl engaged with the gear teeth for locking. We can attach the gear and pawl of a ratchet to the pivoting center and one arm of the mC-SLE, respectively. In a locked condition, the arm will drive the pawl to push the gear to rotate, as shown by the yellow arrow in Fig.4.3(c.1). In a released condition, the pawl gets stuck in the gear and the rotation stops, as shown in Fig.4.3(c.2).

A problem with a single ratchet is that the gear does not necessarily stay stationary in a released condition. If the friction between the pawl tip and the gear teeth is larger than the gear's rotational resistance, the gear may rotate back together with the pawl, leading to failure in the single-direction regulation. Although a large rotation load may provide enough external torque to overcome the friction, it is however not reasonable to assume a rotation load to be large. Also, even if the external torque in the released condition is large, the resulted motion is an intermittent rotation instead of a continuous one. Thus, we propose using a double-ratchet mechanism to cancel out the resistance and implement continuous rotation.

The proposed double-ratchet mechanism

Fig.4.4(a) shows the double-ratchet mechanism. We attach the pawls of two ratchets to two inversely rotating SLE arms. When the back ratchet is in a locked condition, the front ratchet is in a released condition. If the back SLE arm is pushed, the back gear will be driven by the back pawl to rotate clockwise. The back gear motion will be transmitted to the front gear by the central connecting shaft and cause the front gear to rotate clockwise, too. The front pawl will not block the rotation since it is released. The transmitted driving force overcomes the friction between the front pawl tip and the gear teeth; When the front ratchet is in a locked condition, it will be pushed by the front pawl to continue rotating clockwise. The back ratchet is in a released condition and will rotate accordingly with the front gear following the connecting shaft. Like the previous case, the back pawl will not block the rotation since it is released.

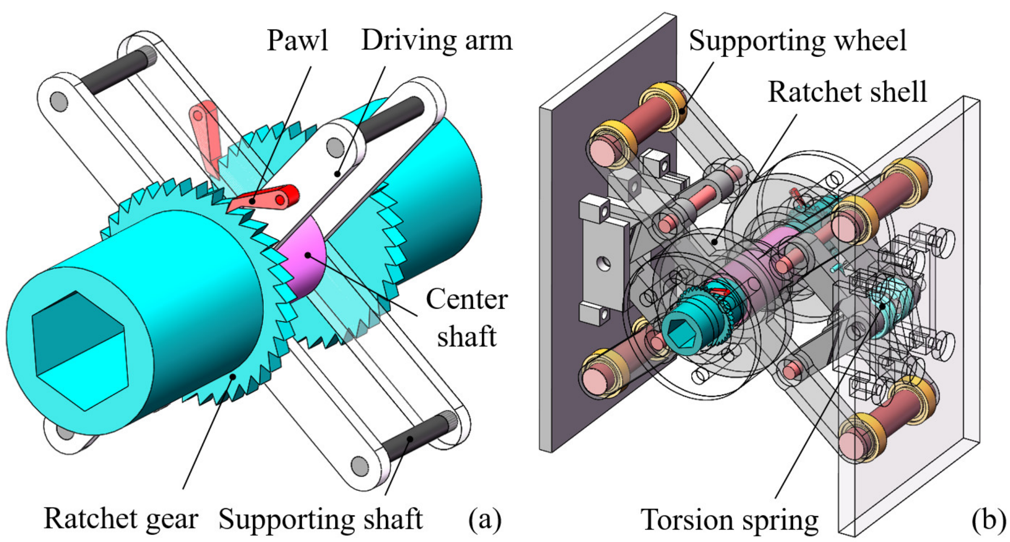

Figure 4.4: (a) A double-ratchet mechanism and two hosting SLE arms. (b) The proposed mechanical screwing tool design.

Fig.4.4(b) illustrates the screwing tool design considering the mC-SLEs and double-ratchet mechanism. It comprises two parallel and co-centric mC-SLEs. On the front mC-SLE, a ratchet is attached to perform clockwise rotation when the pads are squeezed. On the back mC-SLE, a second ratchet is attached to continue the rotation when the pads get stretched. The two ratchets are attached inversely to produce rotations in different directions. They enable the tool to output a continuous single-direction rotation.

4.2 Analysis and Optimization

In this section, we perform quasi-static analysis to optimize the tool. The goal is to make it stable and compact.

4.2.1 Grasping the Tool

The condition to stably hold the tool

We formulate the contact between robotic fingers and the holding pads of the tool as soft finger contacts [113]. The friction and force at the contact meet the following equation

$$f_{\text{fgr}}^2 + \frac{T_{\text{fgr}}^2}{e^2} \leqslant \mu^2 P_{\text{fgr}}^2, \tag{4.1}$$

where P_{fgr} is the pressure force exerted by the robot finger, T_{fgr} and f_{fgr} are the finger's tangential torque and force, μ is the friction coefficient, and e is an eccentricity parameter that can be computed as

$$e^2 = \frac{\max T_{\text{fgr}}^2}{\max f_{\text{fgr}}^2}. \tag{4.2}$$

When grasping the tool, robotic fingers may contact the tool holding pad at an arbitrary position. Fig.4.5(a) shows an example. Here, d_{com} indicates the distance between the Center of Mass (com) of the tool and the center of the contact. The contact forces can be analyzed following two conditions, as shown in Fig.4.5(b, c). The first condition is when a gripper grasps the tool sufficiently. In this case, the contact force is a distribution shown in Fig.4.5(b). The contact position must meet the following equation to make sure the tool can be stably held

$$d_{\mathrm{com}} \leqslant \sqrt{\frac{4\mu^2 P_{\mathrm{fgr}}^2 e^2}{G_{\mathrm{tool}}} - e^2}. \tag{4.3}$$

Here, G_{tool} denotes the gravity of the tool, and P_{fgr} can be computed by

$$P_{\mathrm{fgr}} = \frac{T_{\mathrm{sprg}}}{r_{\mathrm{drv}} \cos \alpha} - F_{\mathrm{res}}, \tag{4.4}$$

where

$$T_{\mathrm{sprg}} = \xi(\gamma + \alpha - \alpha_{\mathrm{init}}). \tag{4.5}$$

The notation T_{sprg} indicates the torque of torsion springs, r_{drv} indicates the length of an mC-SLE's driving arm, α indicates the angle between an mC-SLE's driving arm and the holding pad, F_{res} indicates the resistance force caused by the reversing ratchet pawl and various frictions, ξ indicates the elasticity coefficient of the torsion springs, γ indicates the pre-set rotational deformation of the torsion springs used in assembling the tool (the springs cannot be fixed without it), and α_{init} is the α angle when the tool is initially held by a gripper.

The second condition is a canonical state where the contact forces concentrate on one side of the fingers, as shown in Fig.4.5(c). It happens when the tool is bearing a maximum rotational load. We study it in detail in the following part to analyze the maximum output torques.

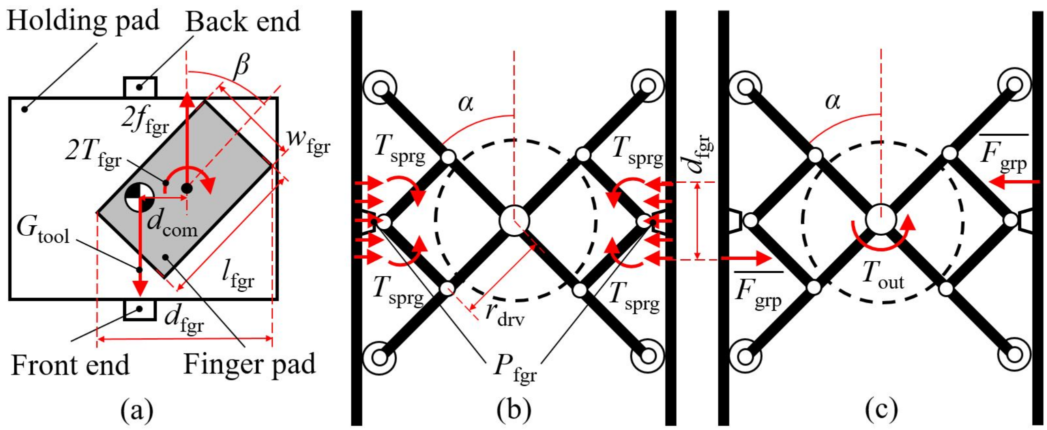

Figure 4.5: (a) Side view of a robotic gripper grasping the tool. (b) A free body diagram of the tool when it is held by a robotic gripper. (c) A free body diagram of the tool when it is bearing a maximum rotational load.

Maximum output torque at the tooltip

We analyze the second condition and study the maximum output torque at the tooltip by considering squeezing and stretching phases respectively. In the squeezing phase, the maximum output torque T_{sqz} can be computed by

$$T_{\mathrm{sqz}} = (F_{\mathrm{grp}} - \frac{T_{\mathrm{sprg}}}{r_{\mathrm{drv}} \cos\alpha} - F_{\mathrm{res}}) \cdot d_{\mathrm{fgr}}, \tag{4.6}$$

where

$$d_{\mathrm{fgr}} = w_{\mathrm{fgr}} \sin\beta + l_{\mathrm{fgr}} \sin\beta. \tag{4.7}$$

The meanings of the various notations in equation (4.7) are graphically explained in Fig.4.5(a), where w_{fgr} and l_{fgr} are the width and length of a finger, and β is the finger angle. The contact force F_{grp} concentrates on $\overline{F_{\mathrm{grp}}}$ in the squeezing phase to provide a maximum actuating torque and thus a maximum output torque at the tooltip.

To have an intuitive view of the relation between F_{grp} and T_{sqz}, we set the parameters γ, ξ to constants ($\gamma \leftarrow 0^\circ$, $\xi \leftarrow 6.00\times10^{-3} Nm/^\circ$) and examine the changes of T_{sqz} with respect to varying F_{grp}, α, β, and r_{drv}. The results are shown in Fig.4.6(a). They reveal how the grasping force, jawwidth, and grasping pose influence the squeezing output. In the figure, α, β and r_{drv} are decoupled to make the function map visualizable. Fig.4.6(a.1) shows the relation between (F_{grp}, α) and T_{sqz}, where β and r_{drv} are fixed to 59° and 20.0mm. Fig.4.6(a.2) shows the changes of T_{sqz} with respect to different F_{grp} and β, where α and r_{drv} are fixed to 45° and 20.0mm. The influence of F_{grp} and β on T_{sqz} is shown in Fig.4.6(a.3), where α and β are fixed to 45° and 59°.

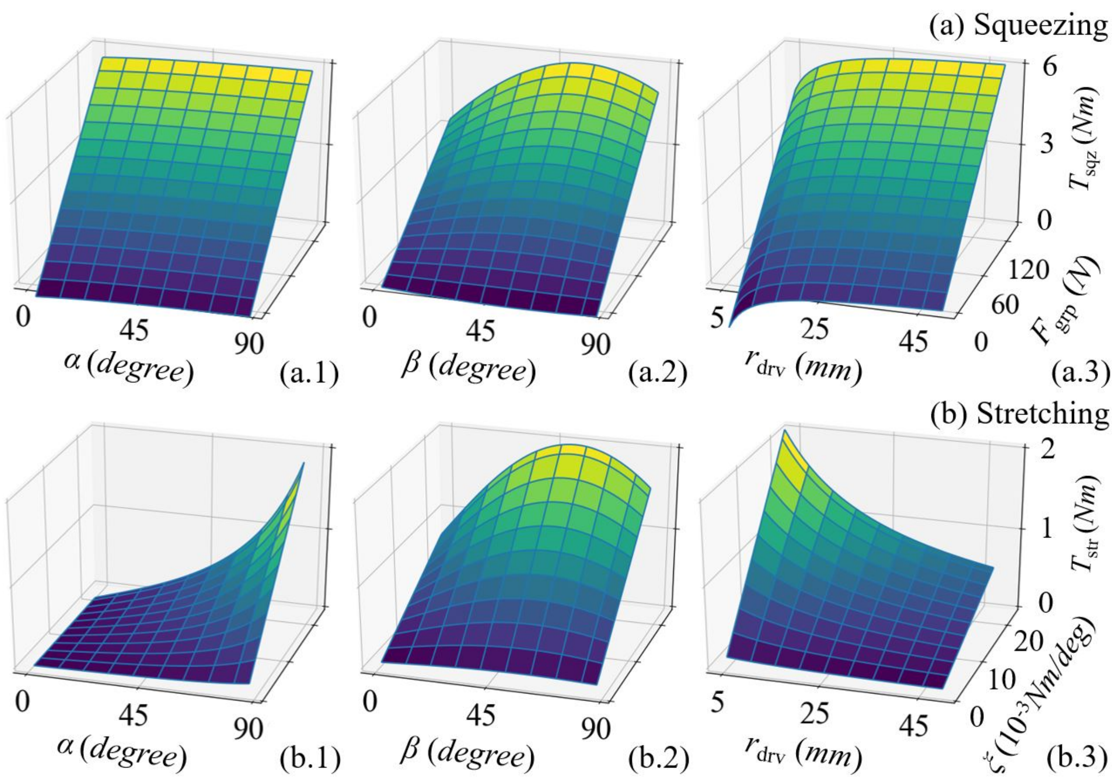

Figure 4.6: (a) Changes of T_{sqz} with respect to varying F_{grp}, α, β, and r_{drv}. (b) Changes of T_{str} with respect to varying ξ, α, β, and r_{drv}.

In the stretching phase, F_{grp} also concentrates on $\overline{F_{\mathrm{grp}}}$ when the output torque reaches maxima, but the gripper fingers no longer exert active forces on the tool. The tool's actuating torque is provided by T_{sprg}, and F_{grp} is a passive force that maintains balance at the holding pads. The maximum output torque can be computed by

$$T_{\mathrm{str}} = \left(\frac{T_{\mathrm{sprg}}}{r_{\mathrm{drv}} \cos\alpha} - F_{\mathrm{res}}\right) \cdot d_{\mathrm{fgr}}. \tag{4.8}$$

Fig.4.6(b) shows the changes of T_{str} with respect to varying ξ, α, β, and r_{drv}, where γ is set to $0°$, and the other parameters are fixed in the same way as Fig.4.6(a).

Velocities at the tooltip

The rotation of the output end continues across the squeezing and stretching phases, as shown in Fig.4.7. The black arrow denotes the rotation of the output end. The triangle markers show the historic angle changes. Fig.4.7(a, b) is the squeezing phase. In this phase, the black arrow points to the yellow triangle initially. As the tool gets squeezed, the output end rotates clockwise to the blue triangle. The angle between the blue and yellow triangles is the squeezing phase's output rotation. It can be formulated as

$$\delta_{\mathrm{sqz}}(t) = \alpha_{\mathrm{init}} - \sin^{-1}\left(\sin\alpha_{\mathrm{init}} - \frac{v_{\mathrm{sqz}} \cdot t}{4r_{\mathrm{drv}}}\right), \tag{4.9}$$

where $\delta_{\mathrm{sqz}}(t)$, t, and v_{sqz} denote the output angle, a time variable, and the velocity of the gripper fingers in the squeezing phase. The range of t is $[0, t_{\mathrm{m}}]$, where t_{m} is the end time instant of the squeezing phase.

Fig.4.7(c, d) is the stretching phase that follows (a, b). The black arrow points to the blue triangle initially (end state of the squeezing). As the tool gets stretched, the output end continues to rotate clockwise to the green triangle. The angle between the green and blue triangles is the output rotation of the stretching

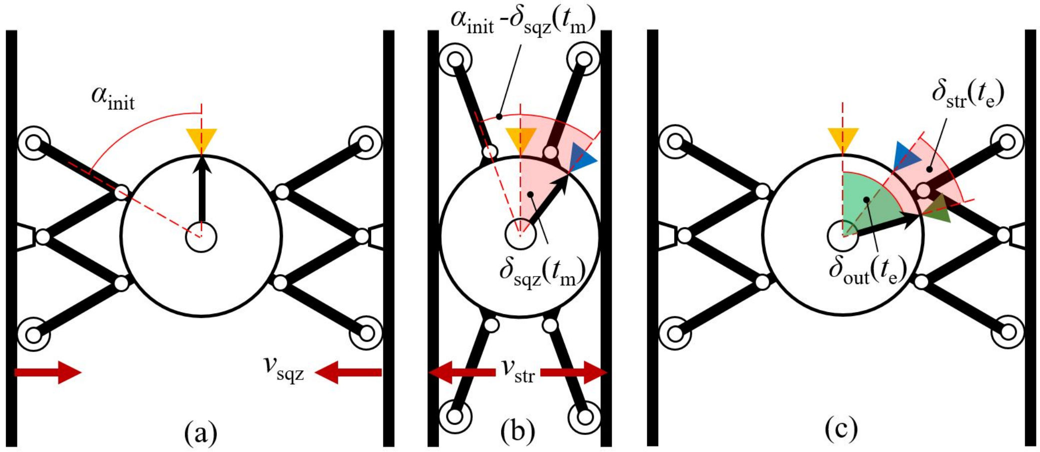

Figure 4.7: (a) Initial angle in a squeezing phase (α_{init}). (b) Output angle at the end of a squeezing phase ($\delta_{\text{sqz}}(t_{\text{m}})$), it is also the initial angle of a following stretching phase. (c) Output angle at the end of a stretching phase ($\delta_{\text{str}}(t_{\text{e}})$).

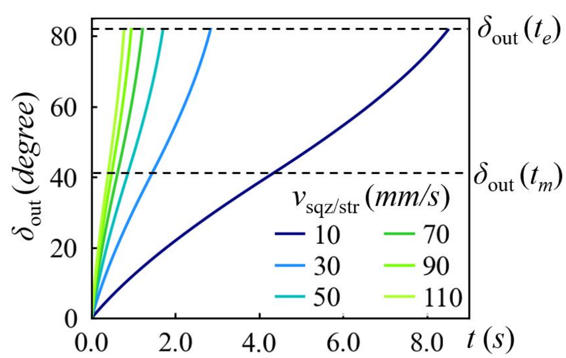

Figure 4.8: δ_{out}-t relation curve under different v_{sqz} and v_{str}.

phase. It can be formulated as

$$\delta_{\text{str}}(t) = -(\alpha_{\text{init}} - \delta_{\text{sqz}}(t_{\text{m}})) + \sin^{-1}\left(\sin\left(\alpha_{\text{init}} - \delta_{\text{sqz}}(t_{\text{m}})\right) + \frac{v_{\text{str}} \cdot t}{4r_{\text{drv}}}\right), \tag{4.10}$$

where $\delta_{\text{str}}(t)$, t, and v_{str} indicate the output angle, a time variable, and the velocity of gripper fingers in the stretching phase. The range of t is $(t_{\text{m}}, t_{\text{e}}]$, where t_{e} is the end time instant of the stretching phase.

In a complete squeezing-stretching cycle, the output rotation continues and forms a total output angle denoted by the green sector in Fig.4.7(d). It can be formulated as a piece-wise function

$$\delta_{\text{out}}(t) = \begin{cases} \delta_{\text{sqz}}(t) & 0 \le t \le t_{\text{m}}, \\ \delta_{\text{str}}(t) & t_{\text{m}} < t \le t_{\text{e}}. \end{cases} \tag{4.11}$$

Fig.4.8 shows the curves of the piece-wise function under different $v_{\text{sqz/str}}$ values (v_{sqz}=v_{str}=10~110mm/s with 20mm/s intervals). The results imply that an increased $v_{\text{sqz/str}}$ significantly reduces the operation time and hence screwing costs.

4.2.2 Selecting Proper Torsional Springs

We choose the torsional springs considering the balance of the output torques in both squeezing and stretching phases. The reversed signs of T_{sprg} in equations (4.6) and (4.8) imply a trade-off between T_{sqz} and T_{str}: T_{sqz} monotonically increases with T_{sprg}. Contrarily, T_{str} monotonically decreases with T_{sprg}. The spring forces are resistant in the squeezing phase but propulsive in the stretching phase. A larger spring coefficient will lead to a large output torque in the stretching phase but a weaker one in the squeezing phase.

The relations between T_{sqz}, T_{str}, and T_{sprg} are visualized in Fig.4.9(a). Here, we use T_{out} in the vertical axis to denote either T_{sqz} or T_{str}. The values of α and d_{fgr} are fixed to 45° and 45mm for 2D visualization. The horizontal axis indicates the coefficient of the torsional springs, ξ. The solid blue curves show the T_{sqz}-ξ relation under different F_{grp} values. The yellow dashed curve shows the T_{str}-ξ relation (F_{grp} is passive in computing the yellow dashed curve). The figure shows that T_{str} increases as the coefficient of the torsional springs increases. At the same time, the gripper will need a larger force to produce the same amount of T_{sqz}.

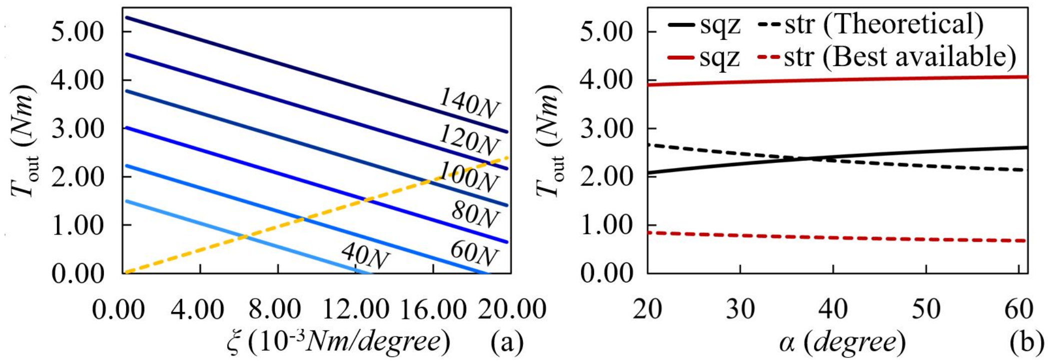

Figure 4.9: (a) Blue curves: The T_{sqz}-ξ relation under different gripper forces. Yellow dashed curve: The T_{sqz}-ξ relation when F_{grp} is at its minimum. (b) Black curves: The output torque-angle relation when a theoretically optimal spring is used (ξ=18.84 $\times$ $10^{-3}Nm/^{\circ}$, F_{grp}=125N). Red curves: The output torque-angle relation when a best commercially available spring is used (ξ=6.00 $\times$ $10^{-3}Nm/^{\circ}$, F_{grp}=125N).

Considering this trade-off, we propose to select a proper ξ by optimizing equation (4.12)

$$argmax_{\xi} \int_{\alpha_{\mathrm{init}}-\delta_{\mathrm{sqz}}(t_{\mathrm{m}})}^{\alpha_{\mathrm{init}}} \left|T_{\mathrm{sqz}}(\alpha,\xi)\cdot T_{\mathrm{str}}(\alpha,\xi)\right| d\alpha. \tag{4.12}$$

The equation computes the definite integral of $|T_{\mathrm{sqz}}(\alpha,\xi)\cdot T_{\mathrm{str}}(\alpha,\xi)|$ under bounds $\alpha_{\mathrm{init}} - \delta_{\mathrm{sqz}}(t_{\mathrm{m}}) \sim \alpha_{\mathrm{init}}$. The reason we propose this optimization is that the ξ that induces the max integral will make T_{sqz} and T_{str} simultaneously large.

The optimal ξ by solving equation (4.12) is $18.84 \times 10^{-3}Nm/^{\circ}$. The black curves in Fig.4.9(b) show the changes of T_{sqz} and T_{str} under this value with respect to a varying α. The curves show that when ξ=18.84 $\times$ $10^{-3}Nm/^{\circ}$, T_{sqz} is close to T_{str} at all α angles and the tool rotates smoothly and steadily in a whole squeezing-stretching cycle. Unfortunately, commercial torsional springs with the theoretically optimal ξ are too large to fit the size of our tool. Thus, we give up this optimal value and choose a spring with $\xi = 6.00 \times 10^{-3} Nm/^{\circ}$ instead. This spring meets the dimensional requirements. Meanwhile, it has an acceptable ξ value. The T_{sqz}-α and T_{str}-α relations using the chosen spring are shown by the solid and dashed red curves in Fig.4.9(b).

Under this spring selection, the designed tool can provide forces to fasten screws with the sizes shown in the light grey area of Table 4.1. Here, a Robotiq Hand-E gripper with a maximum 125N gripping force is assumed to squeeze and stretch the tool. The values in the table are from the Japanese Industrial Standards for general machinery (JIS B [135] [136]). The tool can output a torque between 3.85Nm~4.06Nm in the squeezing phase and between 0.65Nm~0.78Nm in the stretching phase. According to the table, it could maximally fasten M5 screws with 4.8 property class.

To further increase the fastening ability, one may use a gearbox to increase the output torque or screwing speed of the screwing tool. Like the screwing tool, the gearbox can also be designed as a robot-oriented tool. A robot can grasp it and attach it to the output end of the screwing tool to increase output torque or screwing speed. Fig.4.10 shows an example of a gearbox tool. It has two ends. When end-a is connected to the rotating tool and end-b is connected to a tooltip, the screwing efficiency will be improved. In contrast, when end-b is connected to the rotating tool and end-a is connected to a tooltip, the output torque will be increased. The transmission gear train of this tool is embedded in the black frame. It is based on a commercial planetary gearbox (Taizhi PLF042-5).

The gearbox tool can be implemented with different gear ratios following task requirements. The one shown in Fig.4.10 has a 1:5 gear ratio. It may help increase output torque by 5 times while losing 4/5 of output speed. Originally,

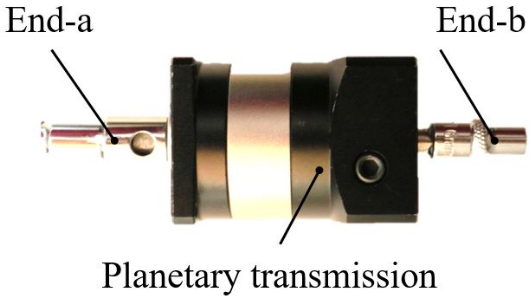

Figure 4.10: A gearbox tool.

the screwing tool can output a torque between 3.85Nm~4.06Nm in the squeezing phase and between 0.65Nm~0.78Nm in the stretching phase. The values cover the standard bolt torques colored in light grey in Table.4.1. It can maximally fasten M5 screws with a 4.8 property class. With the shown gearbox tool's help, the total maximum output torque will be between 19.25Nm~20.30Nm in the squeezing phase and between 3.25Nm~3.90Nm in the stretching phase. Thus, the coverable standard bolt torques expand to the deep grey area, and the tool could maximally fasten M8 screws with a 4.8 property class.

Table 4.1: Standard Bolt Torque Chart

Screw size	Tightening torque (Nm)				
	Property class				
	4.8	6.8	8.8	10.9	12.9
M3	0.56	1.10	1.45	2.08	2.43
M3.5	0.89	1.73	2.28	3.27	3.82
M4	1.31	2.57	3.38	4.84	5.66
M5	2.65	5.19	6.80	9.78	11.43
M6	4.50	8.81	11.60	16.60	19.40
M7	7.56	14.78	19.48	27.88	32.58
M8	10.94	21.39	28.20	40.30	47.20

Note that since the stretching force is weak, the tool may not afford enough torque to fasten bolts in a stretching phase. It may also get stick and slip out of the robotic gripper. To avoid these problems, we develop policy-selection algorithms in Section VI to change the control methods online. A robot will leverage hybrid control and autonomously switch between the squeezing and stretching phases considering force feedback to assure stable and firm screwing. The details and validations will be presented in the related sections.

4.2.3 Optimizing the Geometric Dimensions

Maximum rotational travel

Our geometric optimization's top goal is to maximize the rotational travel of the tool's output end (or equally the rotational travel of an mC-SLE's driving arm). We use the notations shown in Fig.4.11 to carry out the analysis, where the notations α^+ and α^- represent the geometrically maximal and minimal α angle[1], w^+_{tool} and w^-_{tool} represent the geometrically maximal and minimal tool width, h_{tool} represents the height of the tool, r_{drv} is the same as equation (4.4), r_{sup} represents the length of an mC-SLE's supporting arm, r_{whl} represents the radius of a supporting wheel, w_{pad} represents the width of a holding pad, and d_{rcht} represents the diameter of a ratchet gear.

The maximum rotation travel is

$$\Delta\alpha_{\max} = \alpha^+ - \alpha^- = \sin^{-1}\frac{w^+_{\text{tool}} - 2r_{\text{whl}}}{4r_{\text{drv}}} - \sin^{-1}\frac{w^-_{\text{tool}} - 2r_{\text{whl}}}{4r_{\text{drv}}}. \tag{4.13}$$

It depends on four parameters: r_{drv}, w^+_{tool}, w^-_{tool}, and r_{whl}. They are subject to the following constraints.

[1]These geometric values are different from the initial and final angles in Section IV.A.2 since a spring angle is needed there for the springs to provide friction forces for grasping. The relation is $\alpha^+ > \alpha_{init}$ and $\alpha^- < \alpha_{init} - \delta(t_{\text{m}})$.

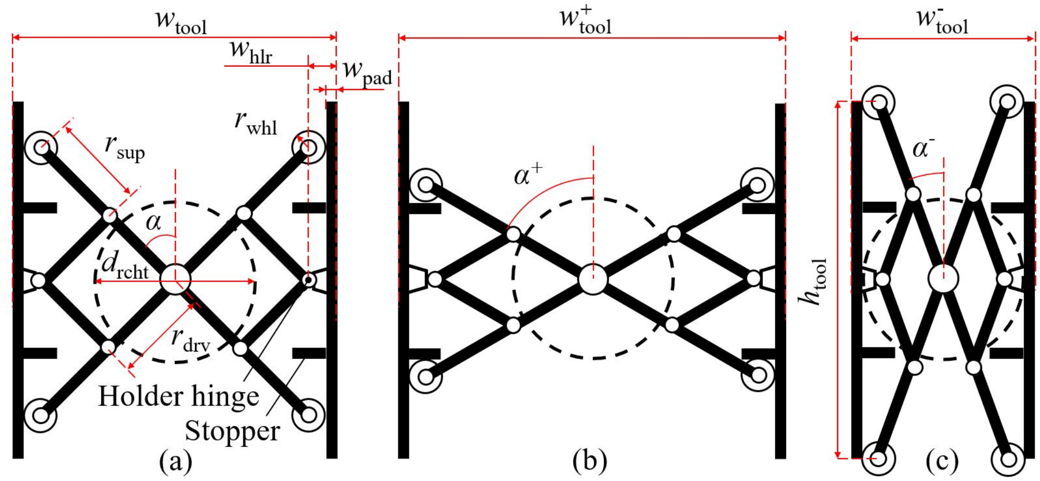

Figure 4.11: Various parameters used in geometric optimization. (a) An intermediate state. (b) The geometric expanding extreme. (c) The geometric folding extreme.

r_{drv}: The value of $\Delta\alpha_{\max}$ monotonically increases with $1/r_{\text{drv}}$, thus r_{drv} is preferred to have a small value. On the other hand, r_{drv} must meet the requirements of the maximum output torque, as shown in equations (4.6) and (4.8).

w^{+}_{tool} and w^{-}_{tool}: Their values must meet

$$w_{\text{tool}} = 4r_{\text{drv}} \sin\alpha + 2w_{\text{hlr}}, \tag{4.14}$$

where w_{hlr} is the distance from the outer surface of a holding pad to its hinge center. The equation shows that w_{tool} monotonically increases with α. In the expanding extreme shown in Fig.4.11(c), the supporting wheels are halted by two stoppers and α reaches α^{+}. The width of the tool reaches w^{+}_{tool}. It must be smaller than the jaw width of a robotic gripper. In the folding extreme shown in Fig.4.11(b), the holding pads contact the ratchet units and α reaches α^{-}. The width of the tool reaches w^{-}_{tool}. It must be larger than $d_{\text{rcht}} + 2w_{\text{pad}}$.

r_{whl}: This value is preferred to be as small as possible, but it subjects to commercial products' availability.

Considering these constraints, we determine the ratchet first. Then, based on the jaw width of an expected robotic gripper that uses the tool and the diameter of the ratchet, we decide w^{+}_{tool} and w^{-}_{tool}. Finally, we optimize r_{drv} following the selected spring (Section.IV.B) and the required output torque (Section.IV.A.3).

Minimum height

The second goal of our geometric optimization is to reduce the height of the tool. The tool's height must be equal to or larger than the holding pads' length, which is constrained by the distance between the supporting wheels on two sides. The distance reaches a minimum at the folding extreme shown in Fig.4.11(c). Thus, the length of the holding pads and also the tool's height must be equal to or larger than this minimum value.

$$h_{\text{tool}} \;\geq\; 2(r_{\text{drv}} + r_{\text{sup}}) \cdot \cos\alpha^{+}. \tag{4.15}$$

The equation indicates that the minimum h_{tool} is essentially affected by three parameters r_{drv}, r_{sup}, and α^{+}. Since r_{drv} and α^{+} have been determined in the previous optimization step, we focus on r_{sup} and study how to reduce it.

Curved supporting surface The idea we use to lessen r_{sup} is to introduce a curved profile to the holding pads' inner surface. The curved profile converts the wheel and the holding pad pair into a mechanical cam pair. The blue curve in Fig.4.12 shows an example. The idea shortens r_{sup} and can thus help reduce the holding pads' length.

We mathematically represent the shape of the curved profile using its parametric form as follows. First, we set up a reference frame at the holder hinge (P_{hng} in

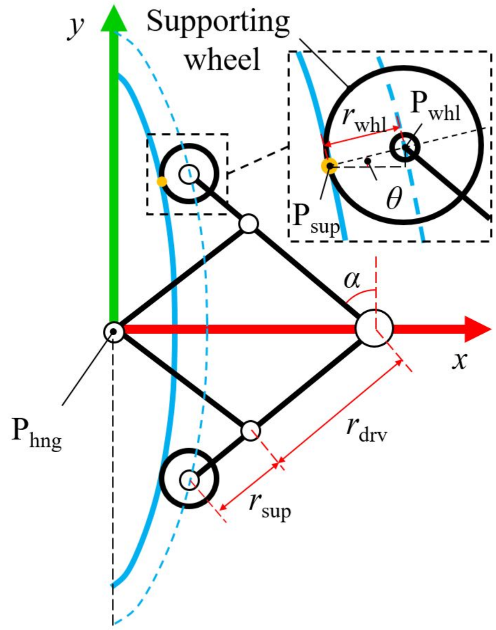

Figure 4.12: Solid blue: A holding pad's curved inner surface. Dashed blue: A supporting wheel's central trajectory.

Fig.4.12(a)). The x axis of the frame points to the center of the ratchet. The y axis aligns with the holding pad. They are illustrated by the red and green arrows in Fig.4.12(a). Then, by representing the supporting wheel's center in the frame as $P_{\text{whl}}=(x_{\text{whl}}, y_{\text{whl}})$, we can formulate P_{whl}'s trajectory as

$$\alpha = \sin^{-1} \frac{x_{\text{whl}}}{r_{\text{drv}} - r_{\text{sup}}}, \tag{4.16}$$

$$y_{\text{whl}} = (r_{\text{drv}} + r_{\text{sup}}) \cos \alpha. \tag{4.17}$$

The blue dashed curve in Fig.4.12(b) illustrates the trajectory. The profile of the holding pad's inner surface is essentially the contact point of the support wheel P_{sup}. It can be obtained by shifting the trajectory of P_{whl} with an offset r_{whl} along $\overrightarrow{P_{\text{whl}}P_{\text{sup}}}$. Assume θ is the angle between $\overrightarrow{P_{\text{whl}}P_{\text{sup}}}$ and x axes. We can represent it as a function of α as

$$\theta = \tan^{-1}(-\frac{\partial y_{\text{whl}}}{\partial \alpha})^{-1}. \tag{4.18}$$

The profile of the holding pad's inner surface will then be

$$\begin{cases} x_{\text{sup}} = x_{\text{whl}} + r_{\text{whl}} \cos\theta \\ y_{\text{sup}} = y_{\text{whl}} - r_{\text{whl}} \sin\theta \end{cases}. \tag{4.19}$$

Here, $(x_{\text{sup}}, y_{\text{sup}})$ indicates the supporting point under the reference frame, and $x_{\text{sup}} \in (0, r_{\text{drv}} - r_{\text{sup}})$. The curved profile represented by this equation can ensure firm contact between a holding pad's inner surface and the supporting wheels across squeezing and stretching phases. Meanwhile, it forces the motion of the SLE arms to be rotation around the ratchet center.

Structural stability Although a smaller r_{sup} reduces h^{-}_{tool}, we cannot choose it arbitrarily as a bad r_{sup} makes the structure less stable. Thus, we perform optimization for r_{sup} and formulate the problem of designing the curved supporting surface as finding the smallest r_{sup} that has satisfying stability.

We evaluate the stability by measuring the wrench cone formed by the Grasp Wrench Set (GWS) of contact points on the holding pads. To simplify the optimization, we assume the motion is 2D, and the contact surfaces are rigid and smooth. Fig.4.13(a) shows all the contact points on the holding pad. We represent them using symbols C_i ($i = 1 \sim 6$), where C_1 and C_2 denote the contacts with gripper fingers. C_3 and C_4 denote the contacts with the supporting wheel. The connections at the hinge are represented as two contacts C_5 and C_6. At each C_i, we use f_i and τ_i to denote the exerted force and moment. We assume that there are friction forces at C_1 and C_2 but $\text{C}_3 \sim \text{C}_6$ are friction-less, as $\text{C}_3 \sim \text{C}_6$ are on the surface of supporting wheels or are hinges. The wrench ω exerted by all the contacts thus equals to:

$$\omega = \sum_{i=1}^{6} G_i \begin{bmatrix} \boldsymbol{f_i} \\ \tau_{ni} \end{bmatrix} = \sum_{i=1}^{6} \begin{bmatrix} \boldsymbol{I} & 0 \\ [\boldsymbol{p_i} \times] & \boldsymbol{n_i} \end{bmatrix} \begin{bmatrix} \boldsymbol{f_i} \\ \tau_{ni} \end{bmatrix}, \tag{4.20}$$

where G_i is the grasp matrix, p_i and n_i indicate the contact positions and the contact normals.

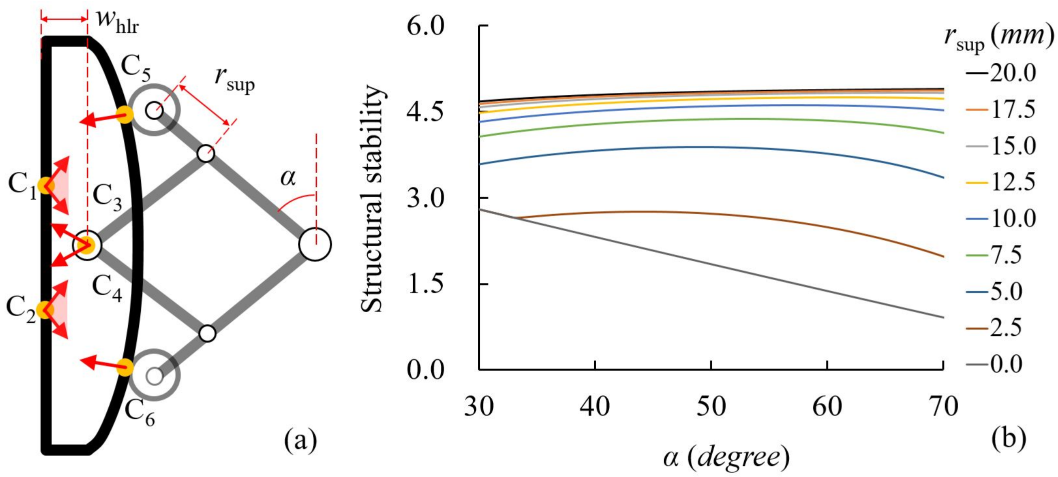

Figure 4.13: (a) We evaluate the structural stability by measuring the wrench cone formed by forces at contacts $C_1 \sim C_6$. (b) The changes in the structural stability with respect to varying r_{sup} and α. The curves with different colors are the results of different r_{sup} values. The w_{hlr} and r_{whl} used to get the results are set to 6.5*mm* and 3.0*mm*, respectively.

Then, we use the Minkovski sum of the wrenches to find the wrench cone following [113]. The structural stability index (Q) is computed as the minimum distance from the wrench cone boundary to a wrench space's origin [137]. Fig.4.13(b) shows the results of our computation under varying r_{sup} and α. The results imply that the structural stability decreases with the increase of both α and r_{sup}. The decreasing speed significantly accelerates when r_{sup} is shorter than 10.0*mm*. Thus, we choose r_{sup} to be 10.0*mm* and determine the shape of the curved supporting surface by replacing it into equations (4.16)-(4.19).

4.3 Prototyping

4.3.1 Mechanical Backlash

First, we study the causes of mechanical backlash, focusing on the ratchet and curved inner holding pad surfaces.

Ratchet

Following the discussions in Section IV.C, we choose a commercial ratchet with a small radius[2] to reduce the tool's geometric size. When the squeezing and stretching phases switch, the relative motion of the ratchet gears and pawls get reversed. The pawl may start from any position between two nearby teeth. The offset from the tooth flanks causes backlash. Fig.4.14 shows the details of our ratchet's pawl-gear section. The backlash appears if the gear starts to rotate counter-clockwise from the shown state. We use θ_{bl} to represent the backlash and use θ_{bl}^{+} to represent its maximum value. Then, θ_{bl}^{+} can be computed by [138].

$$\theta_{\mathrm{bl}}^{+} = \frac{360}{n_{\mathrm{teeth}} \times (1 + \dfrac{\theta_{\mathrm{b}}}{\theta_{\mathrm{f}}})}. \tag{4.21}$$

Here, n_{teeth} denotes the gear's teeth number. θ_{f} and θ_{b} respectively denote the angles on the two sides of a tooth valley. For a ratchet gear, θ_{f} is usually larger than θ_{b}. The value of θ_{bl} is within range $(0, \theta_{\mathrm{bl}}^{+})$. As n_{teeth} and $\theta_{\mathrm{b}}/\theta_{\mathrm{f}}$ increase, θ_{bl} gets smaller and the ratchet rotation becomes faster and smoother. Thus, choosing a ratchet with more gear teeth and a symmetric tooth profile may effectively

[2] ANEX, http://www.anextool.co.jp/item/316

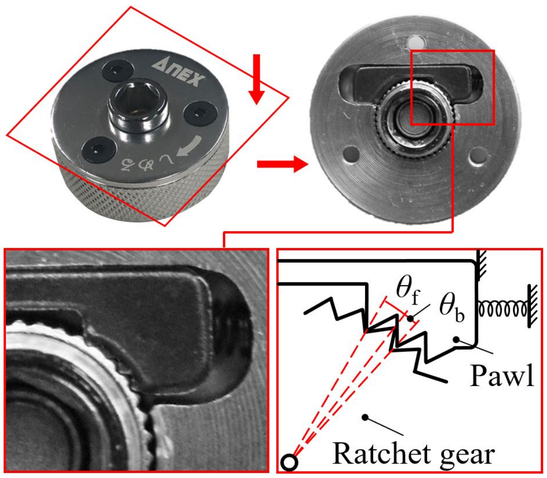

Figure 4.14: Pawl-gear configuration of the selected ratchet.

reduce backlash. Our selected ratchet has 40 gear teeth. Its θ_b and θ_f values are 4.0° and 5.0° respectively. The backlash is at most 5.0° according to equation (4.14).

Machining errors from curved supporting surfaces

As shown in Fig.4.15, machining errors may result in a tilted holding pad after exerting a gripping force and lead to backlash. In this part, we study the tilting and backlash in detail.

To simplify the analysis, we assume $r_{whl} = 0mm$ (or equally $x_{sup} = x_{whl}$ and $y_{sup} = y_{whl}$). Under this assumption, we reformulate equations (4.16) and (4.17) as

$$f(x) = (r_{drv} + r_{sup}) \cos(\sin^{-1}\frac{x}{r_{drv} - r_{sup}}), \tag{4.22}$$

which is the equation of an ideal curve. The solid blue lines in Fig.4.15 illustrate this curve. Following the equation, the curve with machining errors can be represented by

$$f_e(x) = (r_{drv} + r_{sup}) \cos(\sin^{-1}\frac{x + \sigma(x)}{r_{drv} - r_{sup}}) + \psi(f(x)), \tag{4.23}$$

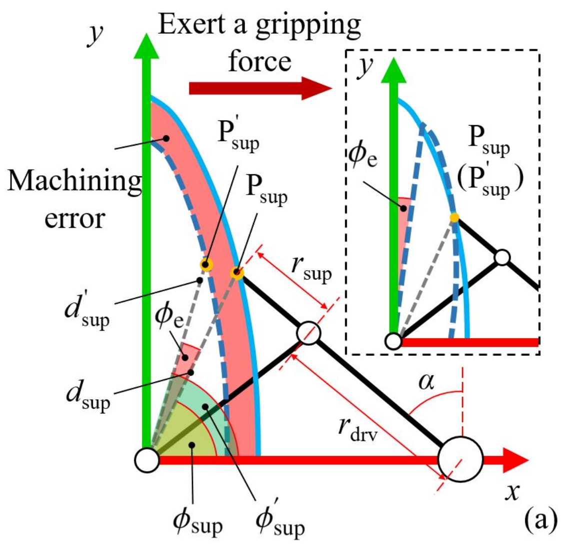

Figure 4.15: An example where machining errors make the curved surface thinner. The solid blue curve shows the theoretical curved surface. The dashed navy curve shows a surface with errors. Due to the errors, the dashed navy curve will rotate with an angle ϕ_e when a gripping force is exerted.

where $\sigma(x)$ and $\psi(f(x))$ indicate machining errors along the x and y axes respectively, and $\sigma(\cdot)$ and $\psi(\cdot)$ are error functions. The dashed navy lines in Fig.4.15 illustrate this curve.

Now we consider a special case where machining errors make the holding pad thinner, which is exactly the one shown in Fig.4.15 – The dashed navy curve shrinks along the -x direction (i.e., $\sigma(x)$=+0.10mm, $\phi(x)$=0mm) from the solid blue curve. The point P_{sup} on the solid blue curve denotes the contact point between the support wheel and the ideal curve. Its coordinates are $P_{sup}=(x_{sup}, f(x_{sup}))$. The point P'_{sup} represents a contact point on the curve with machining errors. Its coordinates are $P'_{sup}=(x'_{sup}, f_e(x'_{sup}))$. When holding pads are pressed, the point P'_{sup} will be forcibly rotated to join the wheel, as is illustrated in Fig.4.15(b), and P'_{sup} and P_{sup} will be coincident. Thus, the d_{sup} and d'_{sup} in Fig.4.15(a) are equal to each other and the following equation can be obtained.

$$\sqrt{f(x_{sup})^2 + x_{sup}^2} = \sqrt{f_e(x'_{sup})^2 + x'^2_{sup}} \tag{4.24}$$

The angle ϕ_e in the figure indicates the backlash angle caused by machining errors. It can be represented by

$$\phi_{\mathrm{e}} = \phi_{\mathrm{sup}} - \phi_{\mathrm{sup}}^{'} = \tan^{-1}\frac{f(x_{\mathrm{sup}})}{x_{\mathrm{sup}}} - \tan^{-1}\frac{f_{\mathrm{e}}(x_{\mathrm{sup}}^{'})}{x_{\mathrm{sup}}^{'}}, \tag{4.25}$$

To study the changes of ϕ_{e} with respect to different α, we formulate equations (4.25) into a relation between ϕ_{e} and α by replacing x_{sup} using $\sin\alpha\cdot(r_{\mathrm{drv}}-r_{\mathrm{sup}})$ and replacing $x_{\mathrm{sup}}^{'}$ using a parametric form deduced from equations (4.23) and (4.24). Then, based on the relation, we particularly study the results of some commonly seen machining errors (constant translations) – We set $\sigma(x) = +0.1mm$; $\sigma(x) = -0.1mm$; $\psi(f(x)) = -0.1mm$; $\psi(f(x)) = +0.1mm$, as seen in Fig.4.16(a.1-4), and observe the resulted ϕ_{e} at different α values to have an intuitive view of how machining errors influence backlash. Fig.4.16(b) shows the results. Here, the values of r_{drv} and r_{drv} are set to $20.0mm$ and $10.0mm$, respectively. By observing the results, we find that: (1) As α increases, the absolute ϕ_{e} gets larger; (2) The $\sigma(\cdot)$ function has a larger influence than the $\psi(\cdot)$ function. With the same constant value, the errors in the x axis lead to a larger ϕ_{e}; (3) For a $0.1mm$ machining error, the maximum ϕ_{e} is $\pm 1.6^{\circ}$. In industrial manufacturing, machining errors of curved surfaces (cams) on a single direction are usually less than $0.02mm$ [139]. Accordingly, the induced backlash is within 0.3°. It is ignorable in practice. Machining errors from the curved surfaces are not a significant source for backlash.

Other machining or assembly errors

To better understand the causes of backlash, we further program a robotic gripper to squeeze and stretch the tool with arbitrary start and end positions and examine the difference from expected output angles. The results of 50 tests show that the backlash values range from 0.1° to 5.4°. The frequency distribution his-

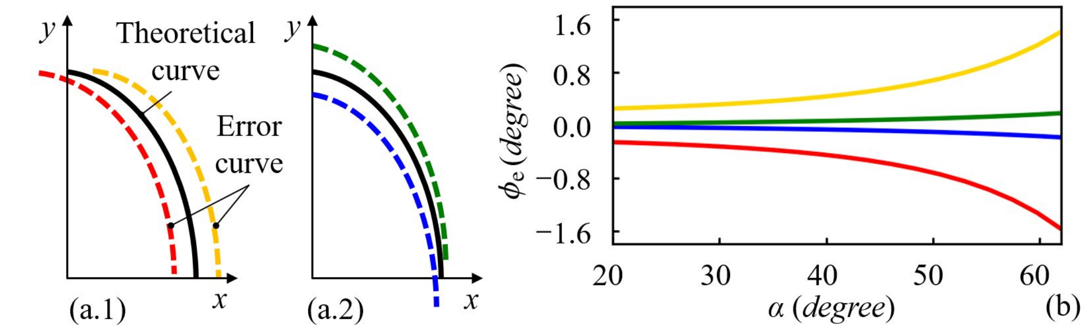

Figure 4.16: (a) Constant translation errors in $\pm x$ and $\pm y$ axes. (a.1) $\sigma(x)$=+0.1mm; (a.2) $\sigma(x)$=−0.1mm; (a.3) $\psi(f(x))$=−0.1mm; (a.4) $\psi(f(x))$=+0.1mm. (b) ϕ_e-α relations under these errors.

togram of the results is shown in Fig.4.17. 90% (45/50) of the backlash values are smaller than 4.0°. The largest observed backlash value (5.4°) slightly exceeds the theoretical maximum (5.0°). The data shows that the teeth of the ratchet are the most important reason for backlash. The excessive 0.4° is probably caused by other machining or assembly errors.

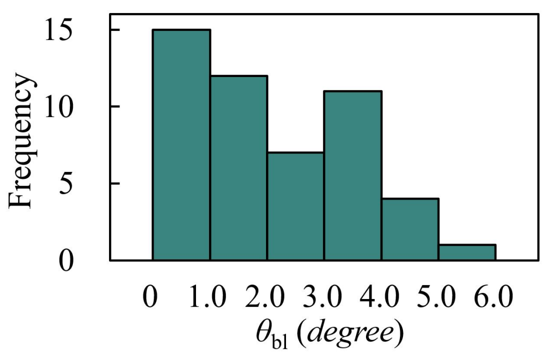

Figure 4.17: Frequency distribution histogram of the observed backlash in 50 random squeezing and stretching experiments. The granularity of the histogram bins is 1.0°.

4.3.2 Fabrications and Analysis

Following the optimization steps and the discussions on backlash, we fabricated three prototypes using curved inner holding pad surfaces and different materials. The first prototype is a fabrication of the design with flat holding pads, as shown in Fig.4.18(a). The second prototype is a fabrication of the design with curved inner holding pad surfaces, as shown in Fig.4.18(b). The links and frames of the two prototypes are made by a 3D printer (ABS materials). We compare them from the perspectives of dimensions, output torques, and output angles. The third prototype is an improved fabrication of the second design. It is made of aluminium materials, has better machining accuracy and mechanical property, and is used in real-world experiments. Note that the pictures in Fig.4.18 are taken on the same scale. By listing them side-by-side, we can observe that the curved surface significantly reduces the dimension of the tool (Fig.4.18(a) *vs*. Fig.4.18(b)). The widths of the two prototypes are both 83.0mm, but the holding pad's height decreases from 80.0mm to 54.0mm, leading to a more compact design that is easier to grasp and more robust to grasping uncertainty. Meanwhile, although the dimension is significantly reduced, the second prototype has a similar output performance as the first one, as shown in Fig.4.19.

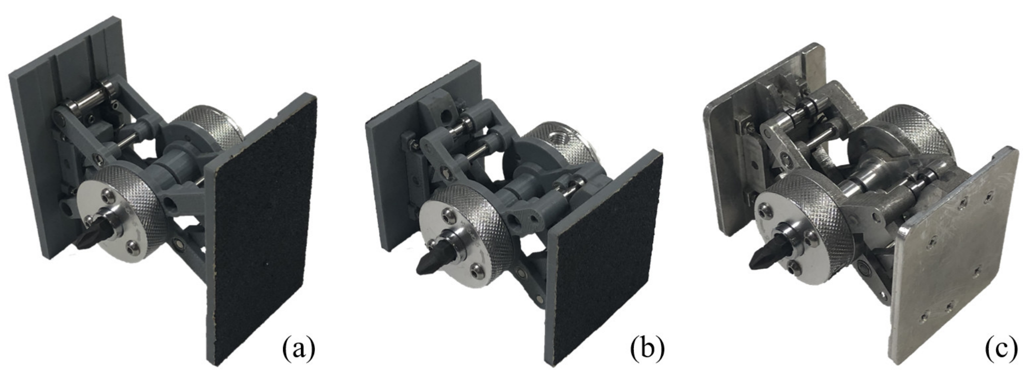

Figure 4.18: (a, b) Two ABS printed prototypes for the designs with flat and curved inner surfaces. (c) An aluminium prototype of the design with curved inner surfaces.

For readers' convenience, we summarize the various parameters we used for

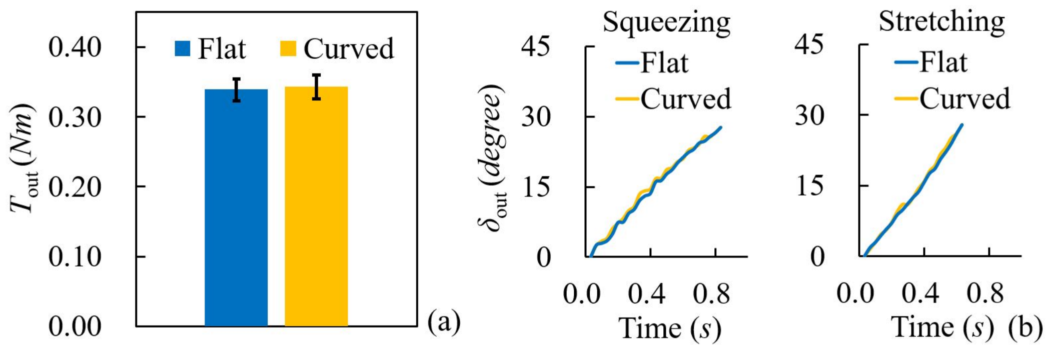

Figure 4.19: (a) Comparison of the maximum T_{out} of the flat and curved prototypes under a 20N gripping force. The results are the average of 5 repetitions. (b) Changes of δ_{out} under v_{sqz} =38mm/s and v_{str} =50mm/s.

the first two prototypes in Table.4.2, and summarize the specifications of the aluminium one in Table.4.3. Note that the tool's effective stroke is not the maximum tool width minus the minimum tool width. A gripper needs to initially squeeze the tool a bit so as to incur enough pressure and friction to hold it. The initial squeezing length is set to 10.0mm considering the selected spring[3].

Table 4.2: Parameters Used to Prototype the Tool

Parameter	Value	Definition
w^{+}_{tool}	83.0mm	Maximum width of the tool
w^{-}_{tool}	40.0mm	Minimum width of the tool
w_{pad}	2.0mm	Thickness of the holding pads
r_{whl}	3.0mm	Radius of a supporting wheel
w_{hlr}	6.5mm	$w_{\text{pad}} + r_{\text{whl}} + offset$
r_{drv}	20.0mm	Length of an mC-SLE's driving arm
r_{sup} $(flat)$	20.0mm	Length of an mC-SLE's supporting arm
r_{sup} $(curved)$	10.0mm	-
h_{tool} $(flat)$	80.0mm	Height of the tool
h_{tool} $(curved)$	54.0mm	-
d_{rcht}	32.0mm	Diameter of the ratchet
ξ	$6.00 \times 10^{-3} Nm/^{\circ}$	Elastic coefficient of the torsional spring

[3]Also see the footnote in page 8. The spring angle for friction is 10°.

Table 4.3: Specifications of the Aluminium Prototype

Item	Value
Size of a bounding box (*mm*)	83.0×62.0×54.0
Weight (*g*)	215
Effective stroke of tool (*mm*)	31.0
δ_{out} in one squeezing-stretching circle (°)	≈ 62

The theoretical time costs for using the tool to fasten a screw can be computed by multiplying the number of squeezing-stretching cycles per screw and the time for one cycle as

$$t_{\text{total}} = \left(\frac{360^\circ}{\delta_{\text{out}}} \cdot \frac{l_{\text{screw}}}{p \cdot n_{\text{ridge}}}\right) \cdot t_{\text{cycle}}, \tag{4.26}$$

where l_{screw} and p are respectively the thread length and thread pitch of the screw, n_{ridge} is the number of thread ridges per pitch, δ_{out} is the output angle of one squeezing-stretching cycle, $(360^\circ/\delta_{\text{out}}) \cdot (l_{\text{screw}}/(p \cdot n_{\text{ridge}}))$ is the number of cycles needed to fasten the screw, and t_{cycle} denotes the time cost of one squeezing-stretching cycle. The value of δ_{out} is 62° for our aluminium prototype. The value of t_{cycle} is 5.5*s* under the maximum gripping speed of Robotiq Hand-E.

The "ST Only" column of Table 4.4 shows the theoretical and real-world efficiency of using the aluminium prototype to fasten screws. Here, we use single-start screws (n_{ridge}=1) with the same thread length (l_{screw}=8.0*mm*) but different thread pitches (M4-0.70*mm*, M6-1.00*mm*, M8-1.25*mm*) for comparison. The results show that the tool is not an efficient one. It takes around 60*s* to fasten an 8*mm* M4 screw. We can use it together with a gearbox tool to improve efficiency. The results after including the gearbox tool are shown in the "ST+GT" column.

Table 4.4: Time costs for fastening different screws

	ST Only			ST+GT		
Screw Type	M4	M6	M8	M4	M6	M8
Number of theoretical cycles	66.2	46.4	37.2	13.3	9.8	7.5
Number of experimental cycles	63.6	43.2	36.0	13.2	9.0	7.2
Theoretical time (s)	62.7	44.0	35.2	12.5	8.8	7.0
Experimental time (s)	58.9	40.2	33.6	11.8	8.1	6.6

* Meanings of abbreviations: ST - Screwing tool; GT - Gearbox tool. The real-world costs tend to be cheaper than the theoretical one. The reason is probably the real thread length becomes shorter due to loss in manufacturing.

4.4 The Manipulation Policies to Use the Tool

This section develops the manipulation policies for using the designed tool. It consists of three parts: (1) Recognizing the tool; (2) Planning grasp and manipulation sequences; (3) Exchanging the tooltips; (4) Detecting and completing screw fastening tasks.

4.4.1 Recognizing the Tool

We assume a depth sensor to be employed for visual recognition. One may use a depth sensor to scan the workspace and locate the tool by registering its model to the collected point cloud. Conventional algorithms like DBSCAN-based segmentation [140], RANSAC-based global search [141], and ICP-based local refinement [142] are employed in the registration. Fig.4.20 shows an example of the collected point cloud and the matched tool pose using the mentioned rough estimation and local refinement routine.

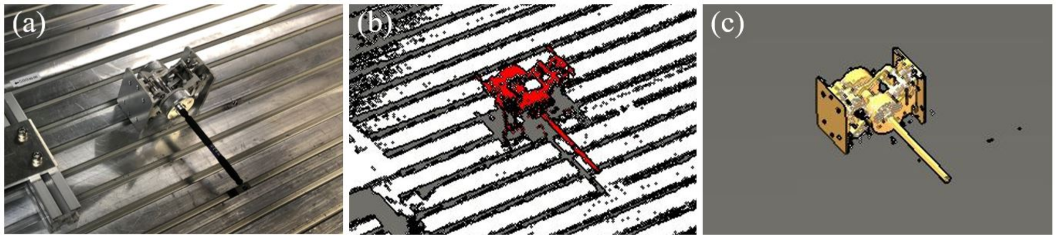

Figure 4.20: (a) The tool on a table. (b) White: Background point cloud; Red: Tool point cloud. (c) The tool pose found by matching the tool's mesh model to the red point cloud.

4.4.2 Planning Grasp and Manipulation Sequences

We use the methods presented in [113] [143] to plan grasping poses, and use the methods presented in [144] [145] [134] [146] to plan placements and regrasp sequences.

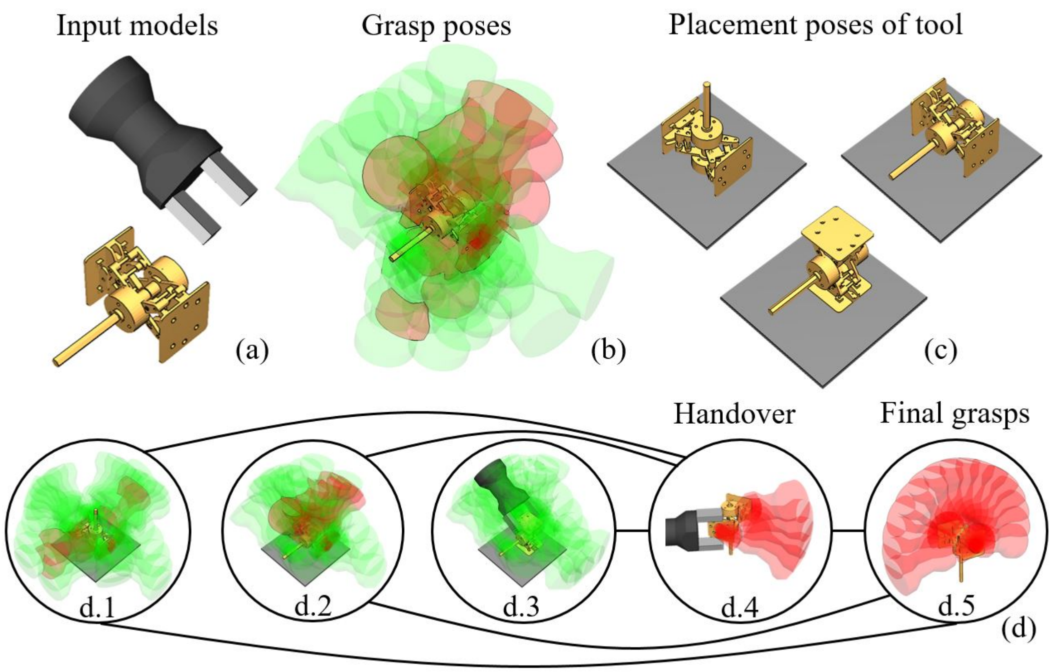

Figure 4.21: (a) Input hand and object models. (b) Planned grasping poses without considering surrounding obstacles. (c) Stable placements of the tool on a flat surface. (d) A graph for reasoning manipulation sequences.

Fig.4.21(a, b) exemplify a hand model and some grasp candidates found by a grasp planner. The planning is automatically performed using the mesh model of the tool. The red hands in Fig.4.21(b) denote the grasp poses that can use the tool. These poses are named the tool-control grasp poses. The green hands denote the grasp poses that can only hold the tool. They are called the tool-holding grasp poses. Fig.4.21(c) shows the stable placements of the tool on a table. A tool's initial pose is a variation of them (the translation and yaw angle may vary). Fig.4.21(d.1-3) show the collision-free grasp poses for each of the stable placements. Fig.4.21(d.4) shows grasp poses for dual-arm hand-over. Given a screwing goal, the collision-free tool-control poses of the tool at the goal can be planned, as shown in Fig4.21(d.5). To manipulate the tool from an initial pose to a goal pose, our planner finds the grasp poses (either tool-control or tool-holding) at the tool's initial pose and performs geometric reasoning between them and the grasp poses in (d.1-4) and the tool-control poses in (d.5) to find the shared ones. The planner will automatically determine single or dual-arm manipulation sequences considering the shared grasp poses.

4.4.3 Exchanging the Tooltips

The tool has two hex magnetic sockets at its output ends for attaching tooltips. A group of tooltips with 1/4 inch hex shank ends can be exchanged and attached to the sockets to meet various task requirements. Attaching the tooltip into the socket is essentially a peg-in-hole problem, and we use a method similar to the one developed by Chen et al. [147] to solve it. We assume one robot arm holds a tooltip while another arm holds a tool. They perform a combined linear search, spiral search, and rotation search with hybrid control to ensure successful insertions.

Linear search

In linear search, the robotic hand holding the tooltip moves along a straight line to make the tooltip end contact the pre-insertion surface. An example is shown in Fig.4.22(a). The robot hand in the example moves along an orange direction $\mathbf{v}^{att}$ to search for the contact between the tooltip end and the socket. The linear motion stops when equation (4.27) is satisfied.

$$\left|\mathbf{v}^{att}(\mathbf{R}^{grpr} \cdot \mathbf{F}^{grpr})\right| \geq F_{threshold}. \tag{4.27}$$

Here, $\mathbf{R}^{grpr}$ is the rotation matrix of the holding hand, $\mathbf{F}$ is the observed force from the F/T sensor mounted at the wrist. $F_{threshold}$ is the desired contact threshold.

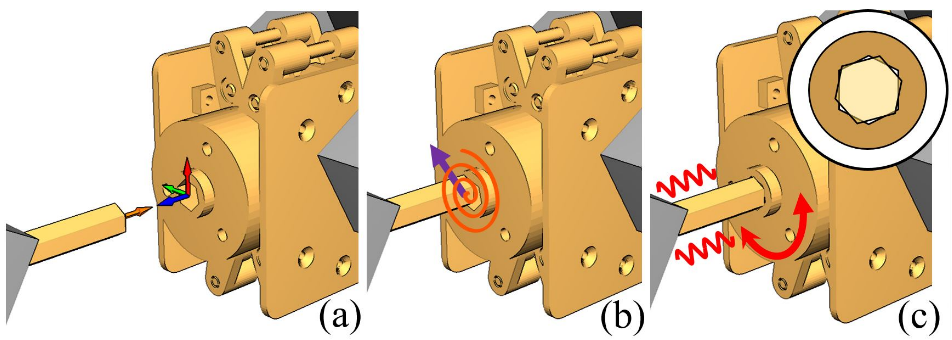

Figure 4.22: (a) Linear search. The hand holding the tooltip moves linearly along the orange vector until it hits the connecting surface. (b) Spiral search. The orange spiral curve indicates the generated spiral path. The purple vector shows the initial spiral direction. (c) Rotation search and impedance control.

Spiral search

Assume that the tooltip end stops at position $\mathbf{P}_0^{hnd}$ at the end of linear search, as is shown in Fig.4.22(b), then, based on this position, a spiral curve and spiral search is planned. The spiral curve is generated according to equation (4.28) in the $\mathbf{R}_x^{socket}$-$\mathbf{R}_y^{socket}$ plane. Here, $\mathbf{R}^{socket}$ represents the pose of the socket. The x and y at the subscript denote the local x and y axes of the rotation matrix.

$$\mathbf{P}_{i+1}^{hnd} = r_{i+1}^{sprl} \cdot \texttt{rodrigues}(\theta_{i+1}^{sprl}, \mathbf{v}^{att}) \cdot \mathbf{v}^{sprl} + \mathbf{P}_i^{hnd}. \tag{4.28}$$

Here, $\mathbf{v}^{sprl}$ indicates the initial spiral direction (the purple vector in Fig.4.22(b)). $\mathbf{P}_i^{hnd}$ and $\mathbf{P}_{i+1}^{hnd}$ are the current position and the planned next position, respectively. $\texttt{rodrigues}(\theta, \mathbf{v})$ is the Rodrigues' rotation formula. θ^{sprl} and r_{i+1}^{sprl} are computed as as:

$$\theta_{i+1}^{sprl} = \theta_i^{sprl} + \delta\theta^{sprl},\ r_{i+1}^{sprl} = r_i^{sprl} + \delta r^{sprl}, \tag{4.29}$$

where $\delta\theta^{sprl}$ and δr^{sprl} are the discretized step rotation and step length of the spiral curve. Since the end of tooltip are chamfered, when the tooltip end is aligned to the pre-inserting position as shown in Fig.4.22(c), equation (4.28) will be violated and the robot will stop the spiral research.

Rotation research and impedance control

After the spiral search, rotation search and impedance control are applied to complete the insertion. We define the impedance control in the workspace following the conventional impedance control law:

$$\mathbf{F}^{insrt} + \mathbf{F}_i^{rsst} = m \cdot \ddot{\mathbf{P}}_i^{hnd} + c \cdot \dot{\mathbf{P}}_i^{hnd} + k \cdot (\mathbf{P}_i^{hnd} - \mathbf{P}_{i-1}^{hnd}) \tag{4.30}$$

where m, c, and k are inertia of the held object, damping coefficient, and stiffness respectively. $\ddot{\mathbf{P}}_i^{hnd}$, $\dot{\mathbf{P}}_i^{hnd}$, and $\mathbf{P}_i^{hnd}$ are the acceleration, velocity, and displacement of the holding hand. $\mathbf{F}^{insrt}$ is the desired insertion force which points to the same direction as $\mathbf{v}^{att}$. $\mathbf{F}_i^{rsst}$ is the external force of the environment. The generated hand motion is thus:

$$\mathbf{P}_{i+1}^{hnd} = \frac{\mathbf{F}^{insrt} + \mathbf{F}_i^{rsst} + m\frac{(2\mathbf{P}_i^{hnd} - \mathbf{P}_{i-1}^{hnd})}{dt^2} + c\frac{\mathbf{P}_{i-1}^{hnd}}{dt} + k\mathbf{P}_i^{hnd}}{\frac{m}{dt^2} + \frac{c}{dt} + k}. \tag{4.31}$$

Along with the impedance control, the hand holding the tool will rotate around $\mathbf{v}^{att}$ to perform rotation research. Thus, $\mathbf{F}_i^{rsst}$ changes with the environment contact and varies with rotation and insertion. The two robots stop simultaneously when $\mathbf{F}^{insrt}$ equals to $(-\mathbf{F}_i^{rsst})_{\mathbf{v}^{att}}$, namely when the tooltip end contacts with the bottom of the socket and the insertion is successfully conducted.

4.4.4 Complete Screw Fastening Tasks

There are two problems in using the tool. First, although the continuous rotation in a squeeze-stretch cycle significantly improves screwing efficiency, they add troubles to task termination as the output torque in the stretching phase is weak and the required fastening torque may not be met if a screwing task is terminated in the stretching phase. The problem might be solved by real-time tactile sensing, which is, however, not always available. Second, detaching the tooltip from a screw head is challenging since it easily gets stick inside the screw head. To solve these problems, we formulate screwing as a decision problem and develop the policy-selection algorithm shown in Fig.4.23 for a robot to perform continuous screwing and complete a screwing task successfully. Here, $(a_{\text{grp}}^{\text{policy}}, a_{\text{rbt}}^{\text{policy}})$ is used to describe the gripper and robot's action or control policy. A gripper has three policies – squeezing, stretching, half-stretching. A robot has two policies – hybrid control and playing a detach primitive. Consequently, the superscript "policy" in $a_{\text{grp}}^{\text{policy}}$ is to be replaced by one of {sqz, str, h-str}. The superscript "policy" in $a_{\text{rbt}}^{\text{policy}}$ is to be replaced by one of {hyb, dtc}. The notation T_{screw} is the screw fastening torque. It is computed by transforming the force and torque measured by a waist F/T sensor to the screw's twist axis. T_{str} indicates the maximum output torque of a stretching phase. The notation T_{goal} denotes the goal screw fastening torque.

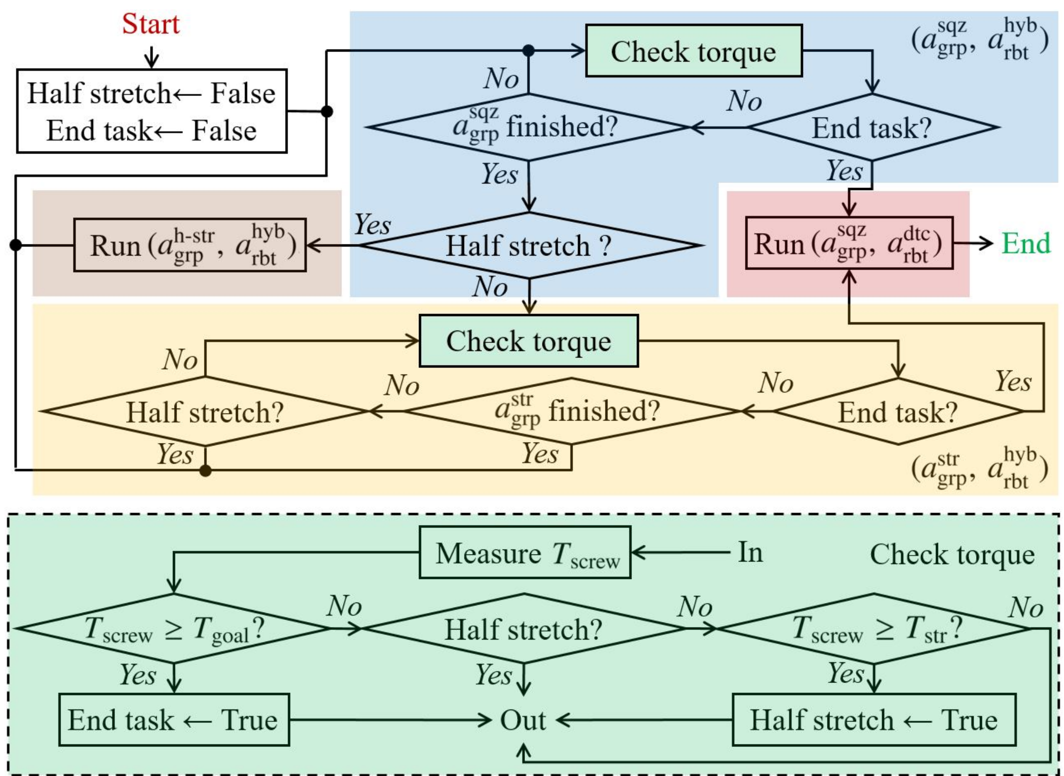

Figure 4.23: Policy-selection algorithm for completing fastening. The light green boxes in the upper part are shown in detail in the dashed block below.

Particularly, the details of $a_{\text{grp}}^{\text{policy}}$ are as follows. $a_{\text{grp}}^{\text{sqz}}$: The gripper closes the fingers to a squeezing extreme (fully closed or the resistant force is larger than the maximum finger force). The policy is irrelevant to initial finger positions. $a_{\text{grp}}^{\text{str}}$: The gripper fully opens the fingers. Likewise, the policy is irrelevant to initial finger positions. $a_{\text{grp}}^{\text{h-str}}$: The gripper opens the fingers until they pass half of the tool's maximum stroke (half open). During screwing, T_{screw} may exceed T_{str}, leading the tool to lose balance and slip out of the gripper. The $a_{\text{grp}}^{\text{h-str}}$ policy is designed to avoid the slippage when T_{screw} is detected to be larger than T_{str}. Its half stretch width will reduce the tool's separation from the fingers[4] Fig.4.24 visualizes the gripper policies. When $T_{\text{screw}}<T_{\text{str}}$, the gripper repeats the $a_{\text{grp}}^{\text{sqz}}$-$a_{\text{grp}}^{\text{str}}$ cycle shown in Fig.4.24(a). When $T_{\text{screw}} \geq T_{\text{str}}$, the gripper repeats the $a_{\text{grp}}^{\text{sqz}}$-$a_{\text{grp}}^{\text{h-str}}$ cycle shown in Fig.4.24(b).

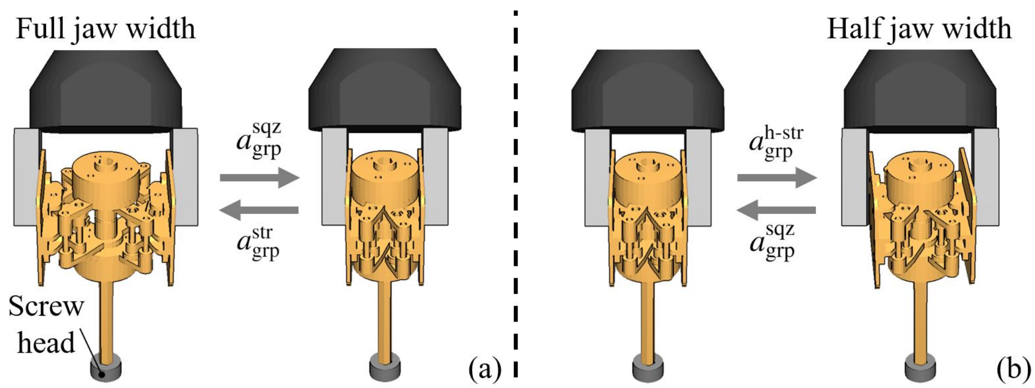

Figure 4.24: Gripper policies. (a) $a_{\text{grp}}^{\text{sqz}}$-$a_{\text{grp}}^{\text{str}}$. (b) $a_{\text{grp}}^{\text{sqz}}$-$a_{\text{grp}}^{\text{h-str}}$.

The details of $a_{\text{rbt}}^{\text{policy}}$ are as follows. $a_{\text{rbt}}^{\text{hyb}}$: A screw will twist into a threaded hole as it is being fastened. Thus, the hand holding the tool must move accordingly to prevent the tooltip from getting separated from the bolt head. Hybrid control is used to implement the accorded hand movement. For the screwing axis, force control is performed to maintain a pushing force between the tooltip and the bolt head. If the contact force reduces, the robot arm will push along the screwing axis to compensate for the force loss and ensure continuous and firm contact between the tooltip and the bolt head. For the remaining transla-

[4]Note that an ideal case is that the opening distance is adjusted automatically following the value of T_{screw}. However, we did not work deep on it since although a dynamically changing stretching distance assures a safer grasp, they result in shorter squeezing travel and thus lower screwing efficiency. In practice, half stretching width both helps avoid losing the tool and at the same time reduces the remaining number of squeezing-stretching cycles.

tional axes, impedance control is used to provide compliance and correct the deviations caused by uncertain deformations. For the rotational axes, position control is used to provide correct squeezing torques. $a_{\text{rbt}}^{\text{dtc}}$: The goal of $a_{\text{rbt}}^{\text{dtc}}$ is to detach the tooltip from a screw head while avoiding sticking. It is designed as a two-phase control policy. In the first phase, the robot performs admittance control to ensure the gripper fingers fully contact the tool holding pads. When T_{screw} exceeds T_{goal}, the gripper fingers are not necessarily in firm contact with the tool. Directly switching to hybrid control and pull the tooltip out may fail because of the small contact force at the infirm contact and unexpected tool inclination. Thus we first perform admittance control to move the robot arm following the force between the gripper fingers and the tool holding pads and make them fully contact each other. In the second phase, the robot performs hybrid control to pull the tooltip out of the screw head. This control policy is developed based on the knowledge that rotating the tool towards the unfastening direction can reduce the force between the tooltip and the screw head. In the hybrid control, the robot moves the tool around the unfastening direction. Meanwhile, it exerts a pulling force along the screwing axis to detach the tool. For the remaining translational and rotational axes, impedance control is used to provide compliance and correct the deviations. Note that rotating the tool towards the unfastening direction will not unfasten screws since the ratchet gear is unlocked along with it. Fig.4.25 visualizes these robot policies.

The policy-selection algorithm shown in Fig.4.23 describes the switches of control policies for successfully completing screwing tasks. In the beginning of a loop, the algorithm initializes the “Half stretch” and “End task” flags as “False”. After that, it starts to perform the ($a_{\text{grp}}^{\text{sqz}}, a_{\text{rbt}}^{\text{hyb}}$) policy, which calls “Check torque” repeatedly until $a_{\text{grp}}^{\text{sqz}}$ is done. In “Check torque”, as shown by the dashed block

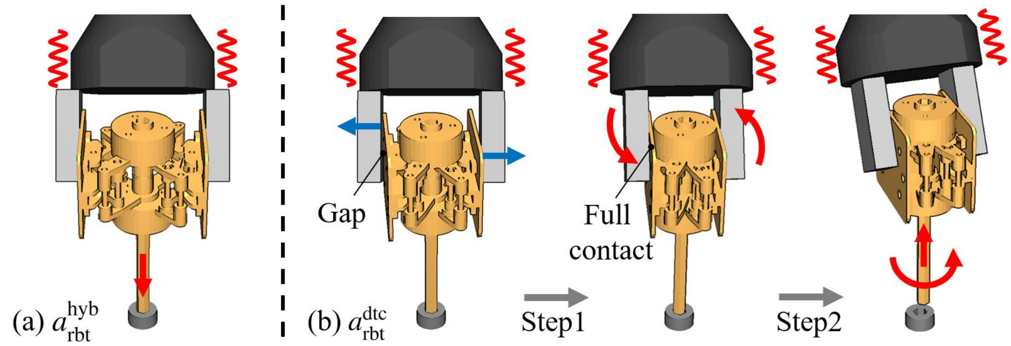

Figure 4.25: Robot policies. (a) $a_{\mathrm{rbt}}^{\mathrm{hyb}}$. (b) $a_{\mathrm{rbt}}^{\mathrm{dtc}}$.

in the lower part of the figure, the algorithm measures T_{screw} and compares it with T_{goal}. If $T_{\mathrm{screw}} \geq T_{\mathrm{goal}}$, "End task" is set to "True". Or else, if $T_{\mathrm{screw}} < T_{\mathrm{goal}}$ and "Half stretch" is "False", T_{screw} is further compared with T_{str}. If $T_{\mathrm{screw}} \geq T_{\mathrm{str}}$, "Half stretch" is set to "True". For other cases, the block returns directly. Back to the main program, when "End task" becomes "True" the algorithm will switch the control policy into $(a_{\mathrm{grp}}^{\mathrm{sqz}}, a_{\mathrm{rbt}}^{\mathrm{dtc}})$ and finish the task. Or else, the algorithm will first wait $a_{\mathrm{grp}}^{\mathrm{sqz}}$ to finish, and then examine "Half stretch". If "Half stretch" is "False", $(a_{\mathrm{grp}}^{\mathrm{str}}, a_{\mathrm{rbt}}^{\mathrm{hyb}})$ will be performed. Otherwise, $(a_{\mathrm{grp}}^{\mathrm{h\text{-}str}}, a_{\mathrm{rbt}}^{\mathrm{hyb}})$ will be selected. Like $(a_{\mathrm{grp}}^{\mathrm{sqz}}, a_{\mathrm{rbt}}^{\mathrm{hyb}})$, $(a_{\mathrm{grp}}^{\mathrm{str}}, a_{\mathrm{rbt}}^{\mathrm{hyb}})$ also calls "Check torque" repeatedly. Note that, when "Half strtch" is set to "True" in $(a_{\mathrm{grp}}^{\mathrm{str}}, a_{\mathrm{rbt}}^{\mathrm{hyb}})$, the current action will be stopped immediately and switched to $(a_{\mathrm{grp}}^{\mathrm{sqz}}, a_{\mathrm{rbt}}^{\mathrm{hyb}})$. When $T_{\mathrm{screw}} \geq T_{\mathrm{str}}$, the stretching phase cannot provide enough torque to further tighten the screw. Thus, we do not call "Check torque" in $(a_{\mathrm{grp}}^{\mathrm{h\text{-}str}}, a_{\mathrm{rbt}}^{\mathrm{hyb}})$. The algorithm will switch to $(a_{\mathrm{grp}}^{\mathrm{sqz}}, a_{\mathrm{rbt}}^{\mathrm{hyb}})$ and perform "Check torque" to determine termination in it after $(a_{\mathrm{grp}}^{\mathrm{h\text{-}str}}, a_{\mathrm{rbt}}^{\mathrm{hyb}})$ is done.

4.5 Experiments and Analysis

In the experiment section, we examine our design's performance, the manipulation policies, and demonstrate the tool's advantages using several real-world tasks.

4.5.1 Performance of the Design

Torque at the tooltip

This part examines our tool's real output torque T_{out} with respect to changing tool width w_{tool} and holding angle β, respectively. The experimental settings are shown in Fig.4.26. A DynPick Capacitive 6-axis F/T sensor (200N, WACOH-TECH Inc.) is used to measure the torque values. One of the robotic grippers holds the tool. The tooltip is inserted into a slot fixed on the torque sensor. The robotic gripper can close as well as open its jaw to exert forces on the tool. The force sensor can thus measure the output torque on-line for both the squeezing and stretching phases. The stable peak torque measured by the force sensor is recorded as the maximum torque.

The results are shown in Fig.4.27 where the yellow curves indicate the theoretical values, and the black curves indicate the experimental values. Fig.4.27(a, b) show the relation between T_{out} and a changing β in squeezing and stretching phases respectively. The value of w_{tool} is set to $73mm$. Fig.4.27(c, d) show the relation between T_{out} and a changing w_{tool} in the two phases. The β angle is fixed to 90°. The theoretical and the experimental results show similarity, but the experimental results are lower than the theoretical ones. The decrease is mainly from

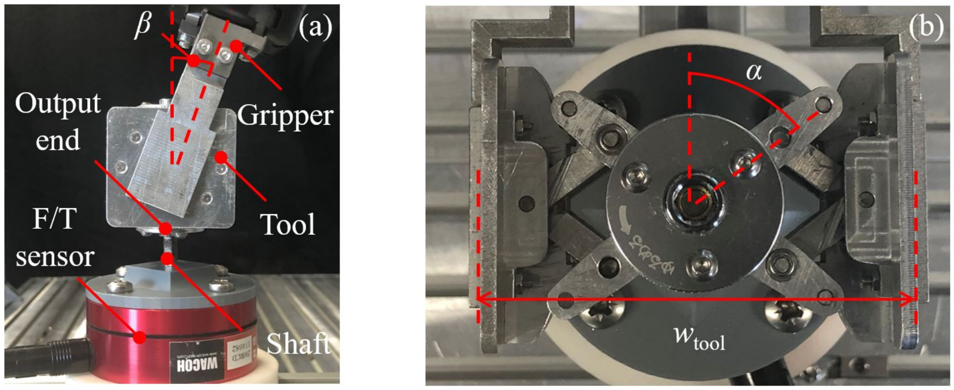

Figure 4.26: Experimental settings for measuring the real maximum output torque. A DynPick Capacitive 6-axis F/T sensor (200N, WACOH-TECH Inc.) is used to measure the output torque. The tool is held by one Robotiq Hand-E gripper. The tooltip is inserted into a slot fixed on the F/T sensor.

the resistance force F_{res}, which is ignored in the theoretical computation as it is hard to model (recall equations (4.6) and (4.8)). According to the experimental results, the tool can output a torque between 3.64Nm ~4.18Nm in the squeezing phase and 0.34Nm ~0.48Nm in the stretching phase. These values are the reference for setting our policy-selection algorithms' parameters (see part B.2 of this section).

Velocities at the tooltip

This part examines the velocities of the tooltip. Particularly, we compared four cases. They are (1) the rotation in the squeezing phase, (2) the rotation in the stretching phase, (3) the rotation in a whole squeezing-stretching cycle, and (4) the rotation during a continuous rotation. An AR marker is used to assist in tracking the rotation. It is attached to plates installed at the tool's output ends, as shown in Fig.4.28(a). Fig.4.28(b) illustrates the front end. Fig.4.28(c) illustrates the back end. Note that since the two ends rotate identically except for their

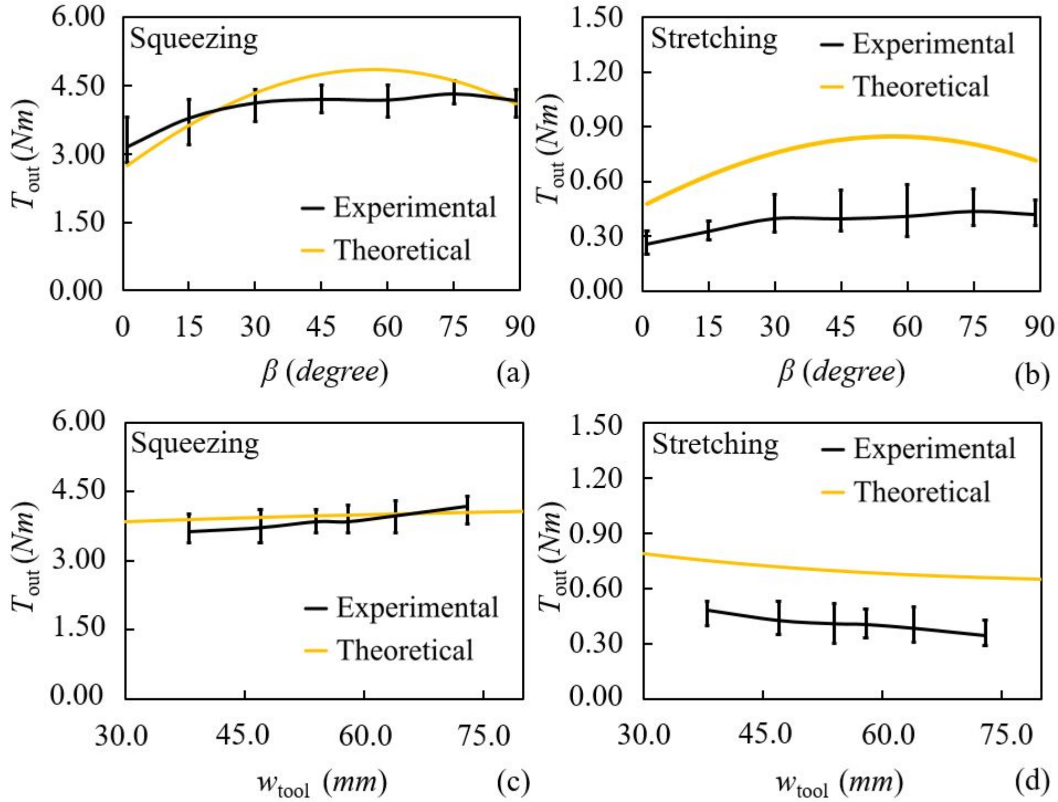

Figure 4.27: Changes of maximum output torque T_{out} with respect to different tool width w_{tool} and holding angle β. Yellow curves indicate the theoretical values. Black curves indicate the experimental values. (a, b) The relation between T_{out} and a changing β. The value of w_{tool} is set to $73mm$. (c, d) The relation between T_{out} and a changing w_{tool}. The β angle is selected to be a fixed value 90°. The theoretical curves are computed using ξ=6.00×10^{-3}$Nm/°$ and F_{grp}=125N.

directions, we only show the front end's measured results below.

Fig.4.29 shows the results. Like Fig.4.27, the yellow curves indicate the theoretical values, and the black curves indicate the measured values. Fig.4.29(a) and (b) are respectively the velocities in the squeezing phase and the stretching phase. For these single-direction actions, the measured values and the theoretical values match well. Fig.4.29(c) is the velocity in a whole squeezing-stretching cycle. The measured values start to deviate from the theoretical values when the tooltip switches its rotation direction – the rotation angle keeps constant from

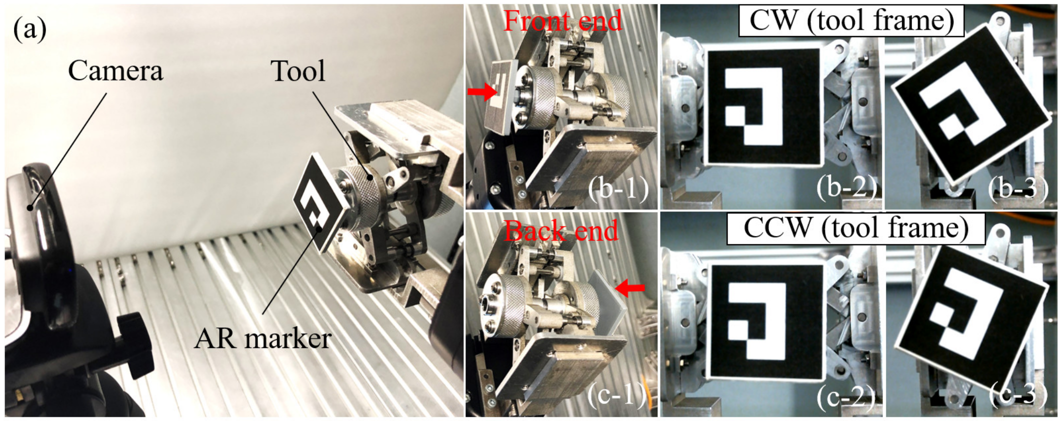

Figure 4.28: An AR marker is used to detect the rotating velocity. (a) The setting for tracking the rotation. (b) The clockwise rotation at the front end. (c) The counter-clockwise rotation at the back end. Note: CW and CCW are counted locally.

3.0s to 3.1s, drops from 3.1s to 3.3s, and resumes to increase after 3.3s. The reason for the constant rotation is that there is a short switching delay between the two phases. The reason for the drop is backlash. Note that the finger speeds in the first three subfigures are 20mm/s for squeezing and 30mm/s for stretching. The slow finger speeds were selected because we would like to have a detailed and clear view of the changes.

Fig4.29(d) further shows the results where a robotic gripper squeezes and stretches the tool continuously. The curve is made of a sequence of smaller patterns where each of them is like the one shown in Fig.4.29(c). In this case, the hand speed used to measure the real angle is selected to 150mm/s. The tool can output a 360° rotation in 5.5s under the speed.

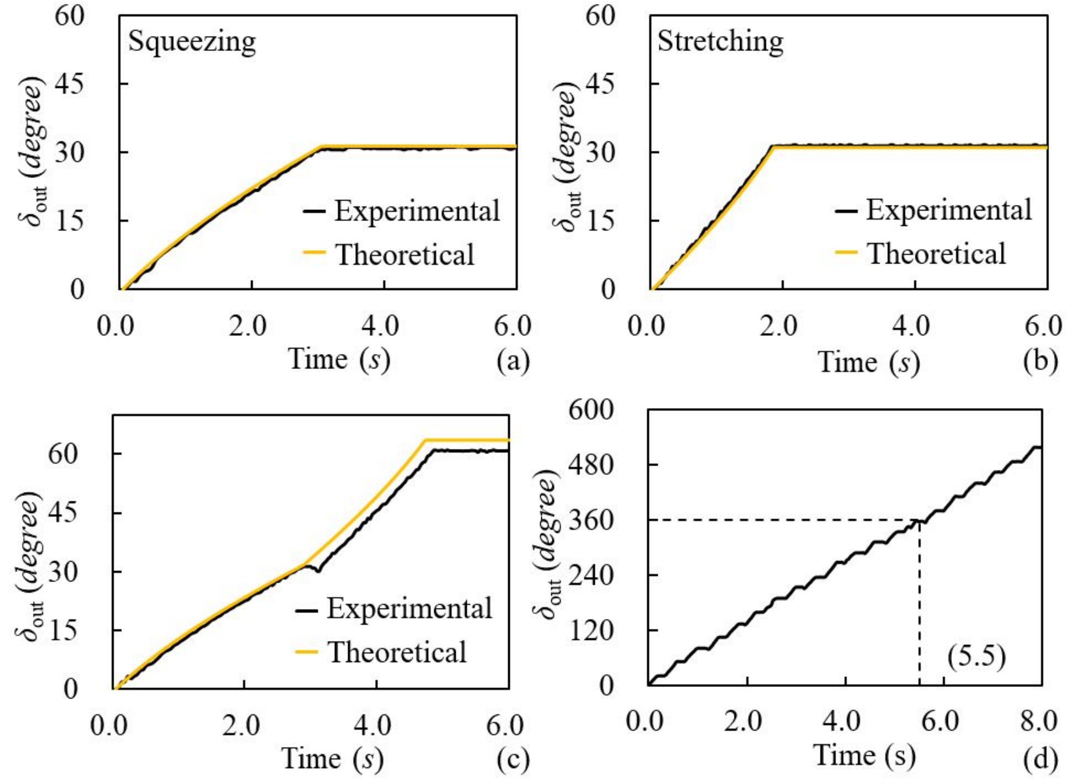

Figure 4.29: Velocities at the tooltip. Yellow curves are theoretical values. Black curves are measured values. (a) Changes of rotation angle concerning time in a squeezing phase. (b) Changes of rotation angle concerning time in a stretching phase. (c) Changes of rotation angle concerning time in a complete squeezing-stretching cycle. (d) The changes of the rotation angle during continuous squeezing and stretching. Note that the results are from the front end. The back ends rotate reversely.

Fatigue life

In this part, we carry out simulations to study the tool's fatigue life. We assume that the gripping force on the tool's holding pads is uniformly distributed and the tool is folded to $\alpha = 60°$. We ignore the ratchet gears, bearings, and springs to simplify the model. The materials of all parts are set to Aluminum alloy (6061). The tool's output end is set to be a fixed rigid body. Based on these assumptions and configurations, we perform static analysis by considering a single load case and a zero-load base type cyclic stress on the tool's holding pads. The maximum number of tolerable squeezing-stretching cycles is counted as the available tool life.

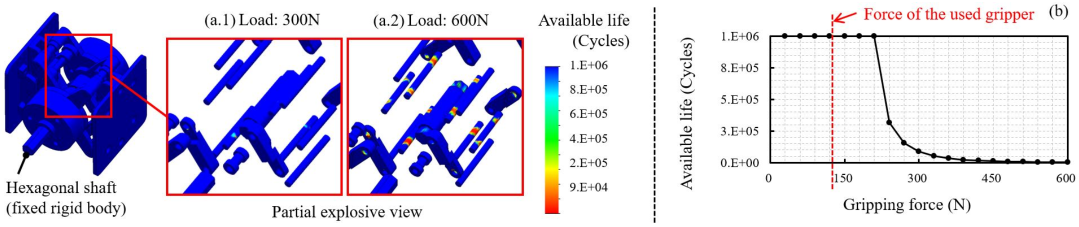

Figure 4.30: Fatigue analysis. (a.1) Load: 300N. (a.2) Load: 600N. (b) Changes of available life under different gripping forces.

Fig.4.30 shows the results. In Fig.4.30(a.1), the exerted gripping force is 300N, and the available tool life is 8.877×10^4 cycles. Fig.4.30(a.2) shows another case when the exerted gripping force is increased to 600N. The available tool life is reduced to 3.528×10^3 cycles. From the results, we find that the weakest parts of the tool are the shafts – fabricating them using durable materials will help increase the available life. Fig.4.30(b) shows the available life curve as the exerted gripping force changes from 30N to 600N. The gripper used in our experiments (Hand-E, Robotiq Inc.) exerts a maximally 125N gripping force on the tool. Under this force, the available life is over 1×10^6 cycles, indicating that the tool is very durable when used by the gripper.

Comparison with other tools

This part compares our tool's efficacy with several other similar ones like manumotive human tools, powered human tools, and powered robot tools quantitatively. We categorize the similar tools into three categories: (1) Manumotive tools designed for humans; (2) Powered tools designed for humans; (3) Powered tools designed for robots. Table 4.5 shows a summary of our tool's pros and cons compared to them. The manumotive tools are designed for humans and are difficult to be grasped by robots. Like the manumotive tools, powered tools designed for humans are also difficult to be grasped by a robot. However, they do not require a robot to perform complicated motions. A robot only needs to pick up a tool and move it to a goal position. Embedded motors realize the tool's rotation function. It is more efficient than the rotation performed by multiple robot joints. Powered tools designed for robots especially consider the structure of a robot hand for achieving force-closure grasps. Robotic end-effectors can firmly hold them. The drawback is that cables like tubes, power supply lines, and other signal wires are indispensable to power on and control the tools. The cables may lead to unexpected collisions or wind around the robot. Compared to these tools, our screwing tool has advantages like stable robotic grasping, small grasping limitations, no cable problems, and low price. Meanwhile, it has a clear disadvantage – low efficiency. To understand the exact efficiency difference, we further compare the detailed screwing time costs in Table 4.6. The proposed tool takes $33.6s$ to fasten an M8 bolt. It is around 1/4-1/5 of a human operating an Allen wrench. To improve the efficiency, a dual-arm robot may use the gearbox tool presented in Section IV.B for collaborative screwing. After including the gearbox tool, the proposed tool's efficiency becomes competitive to humans (the last row of Table 4.6).

4.5.2 Performance of the Manipulation Policies

For examining the performance of the manipulation policies, we focus on exchanging tooltips and completing screwing tasks. Note that since visual recog-

Table 4.5: The comparison of different tools

Tool Types	Robotic Grasping	Constraints for Grasping	Cables	Efficiency	Price
Manumotive	Difficult	Low	No	Low	Low
Powered (Human)	Difficult	High	Needed	High	High
Powered (Robots)	Possible	High	Needed	High	High
Proposed	Convenient	High	No	Low	Low

Table 4.6: Time costs of fastening an M8×8 screw

Tool Names	Time Costs (s)
BOSCH IXO3	2.7
BOSCH GO 3 601 JH2 020	1.8
BOSCH PDR 18LI	0.4
Takagi Earthman ATL-150A	0.3
Allen wrench	7.1
Proposed tool	33.6
Proposed tool with a gearbox tool (1:5)	6.6

The results are based on the average values of 10 trials for each tool. The portable electric tools, BOSCH IXO3, BOSCH 3 601 JH2 020, and BOSCH PDR 18LI, and also the manumotive tool (Allen wrench), are operated by human hands. Takagi Earthman ATL-150A is a pneumatic screwdriver and is operated by a robot.

nition and sequence planning are reusing previously published methods, we do not repeatedly examine them. Only a short discussion about our system recognition precision is included for interested readers. The experiments are performed using two UR3 e-series robot arms, with a Robotiq Hand-E two-finger parallel gripper mounted at each arm's end flange.

Exchanging tooltips

First, we examine the policies for exchanging tooltips. Five tooltips are used in total. They are named to #3 hex screwdriver bit, #6 hex screwdriver bit, #5 short hex screwdriver bit, hex socket extension connector, and cross screwdriver bit. All these tooltips have a 1/4 inch hex shank at the connecting end. The functional ends of the #3 and #6 hex screwdriver bits are used to fasten M4 and M8 inner hex screws, respectively. The functional end of #5 short hex screwdriver bit is used for fastening M6 inner hex screws in a narrow space. The hex socket extension connector is an adapter for other 1/4 inch hex bits. The cross screwdriver bit is used for fastening cross-head screws.

Fig.4.31(a) shows an example where a robot arm removes a #3 hex screwdriver tooltip and replaces it with a #6 one. Some snapshots showing the execution results are shown in Fig.4.31(a). With the tool held by the left hand, the right hand unplugs the #3 hex screwdriver tooltip and inserts a #6 one into the tool's output socket. The linear search, spiral search, and rotation search and impedance control mentioned in Section IV.C are used to ensure a successful insertion. The process is shown in detail in Fig.4.31(a.5-10). Note that removing a tooltip is simply a kinematic motion planning problem along the rotating axis. The connecting hex shanks of the tooltips are chambered to avoid sticking. Thus, there is no need for complicated control. Inside the tool's output end socket, a magnet chip is attached to help stabilize an inserted tooltip. The magnet force is ignorable compared to robotic forces.

Fig.4.31(b-d) show the results for the other tooltips. In the experiments, we assume that the tooltip holders' positions are known, and the screwing tool is held in the robot hand with a known pose. The above tooltips can be inserted and

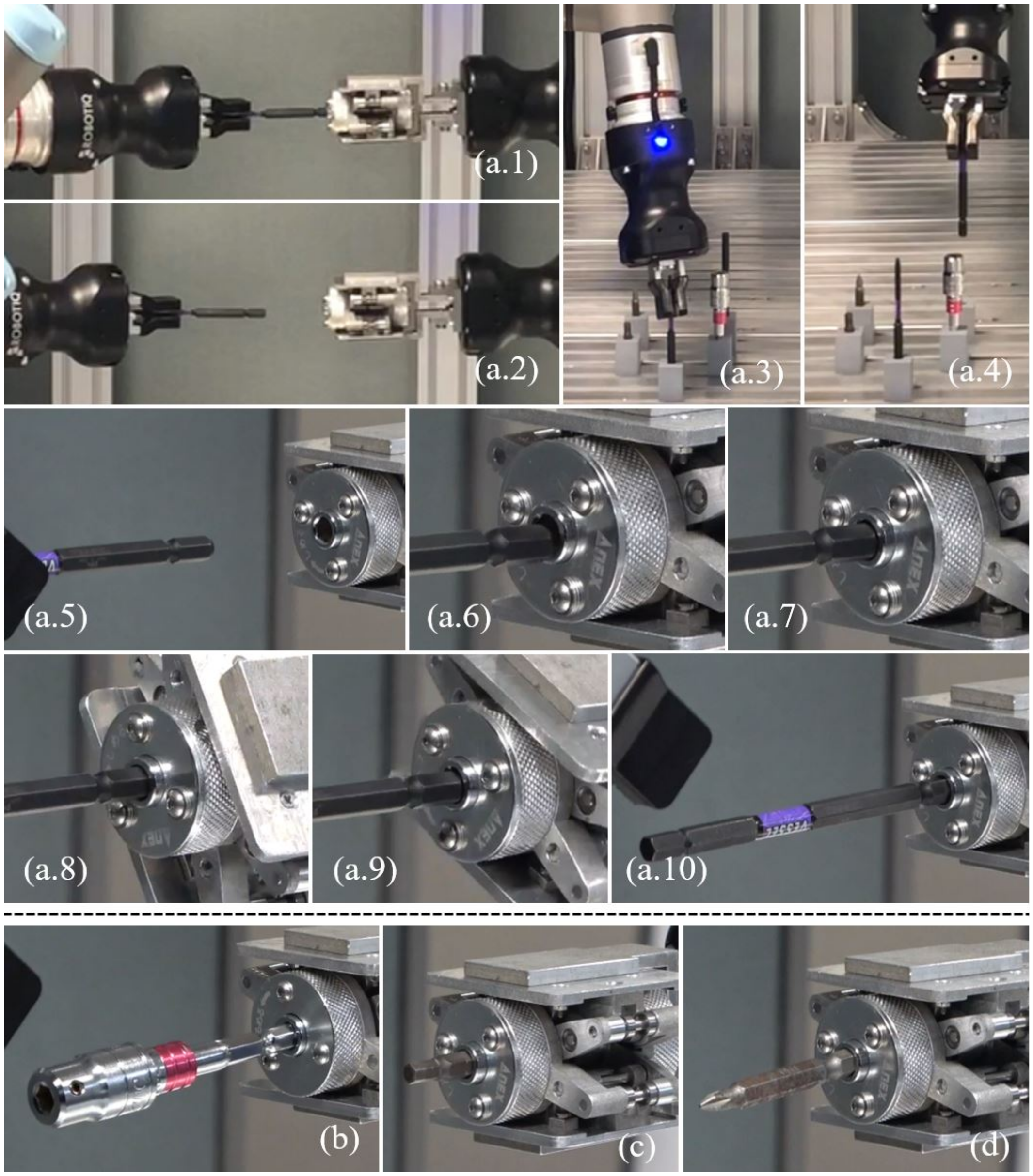

Figure 4.31: (a.1-3) Unplug a #3 hex screwdriver bit and return it to a tooltip stand. (a.4) Pick up a #6 hex screwdriver bit. (a.5-10) Inserting the #6 hex screwdriver bit into the output socket. (a.5,6) Linear search. (a.6,7) Spiral search. (a.8,9) Rotation search and impedance control. (a.10) Final state. (b-d) Some other examples: (b) Exchanging to a hex socket extension connector. (c) Exchanging to a #5 short hex screwdriver bit. (d) Exchanging to a cross screwdriver bit.

exchanged successfully without failure. The proposed manipulation policies for exchanging tooltips are robust to the uncertainty from grasping, modeling, and the tool's hex connecting end's unknown angle.

Completing screwing tasks

We performed several experiments to examine the proposed policy-selection algorithm. The tooltips we used are recessed ballpoint bits (VESSEL No.SS16BP). The value of T_{str} is set as 0.30Nm following Fig.4.29. The value of T_{screw} is computed based on the measurements from the UR3e robot's embedded F/T sensor (Resolution: 0.02Nm; Accuracy: 0.10Nm). The value of T_{goal} is set to different values to examine the performance changes.

Fig.4.32 shows three results of fastening a single-start M8 screw, where T_{goal} is set to 2.00Nm. The black curves are the changes of T_{screw} during screwing. The colored sections denote the selected policies. The blue, yellow, brown, and red colors respectively indicate ($a^{\mathrm{sqz}}_{\mathrm{grp}}$, $a^{\mathrm{hyb}}_{\mathrm{rbt}}$), ($a^{\mathrm{str}}_{\mathrm{grp}}$, $a^{\mathrm{hyb}}_{\mathrm{rbt}}$), ($a^{\mathrm{h\text{-}str}}_{\mathrm{grp}}$, $a^{\mathrm{hyb}}_{\mathrm{rbt}}$), ($a^{\mathrm{sqz}}_{\mathrm{grp}}$, $a^{\mathrm{dtc}}_{\mathrm{rbt}}$). Particularly, Fig.4.32(a) shows a simple case where T_{screw} begins to increase at 4.9s and exceeds T_{goal} at 5.8s. After that, the control policy is switched to ($a^{\mathrm{str}}_{\mathrm{grp}}, a^{\mathrm{dtc}}_{\mathrm{rbt}}$) to finish fastening. Fig.4.32(b) is a bit more complicated. The value of T_{screw} starts to increase at 5.1s. At 5.7s, T_{screw} reaches T_{str}, and the control policy is immediately switched to ($a^{\mathrm{sqz}}_{\mathrm{grp}}$, $a^{\mathrm{hyb}}_{\mathrm{rbt}}$). At 6.0$s$, T_{screw} exceeds T_{goal}, and the control policy is switched to ($a^{\mathrm{str}}_{\mathrm{grp}}, a^{\mathrm{dtc}}_{\mathrm{rbt}}$) to finish fastening. Fig.4.32(c) shows a very complicated case where multiple $a^{\mathrm{h\text{-}str}}_{\mathrm{grp}}$ are performed. At 2.9s, T_{screw} exceeds T_{str} but does not reach T_{goal}. Thus, ($a^{\mathrm{str}}_{\mathrm{grp}}, a^{\mathrm{hyb}}_{\mathrm{rbt}}$) is switched ($a^{\mathrm{h\text{-}str}}_{\mathrm{grp}}, a^{\mathrm{hyb}}_{\mathrm{rbt}}$). After that the ($a^{\mathrm{h\text{-}str}}_{\mathrm{grp}}, a^{\mathrm{hyb}}_{\mathrm{rbt}}$) policy is performed twice between 2.9s~3.9s and between 5.3s~5.7s. At 5.9s, T_{screw} exceeds T_{goal} and the control policy is switched to ($a^{\mathrm{str}}_{\mathrm{grp}}, a^{\mathrm{dtc}}_{\mathrm{rbt}}$) to

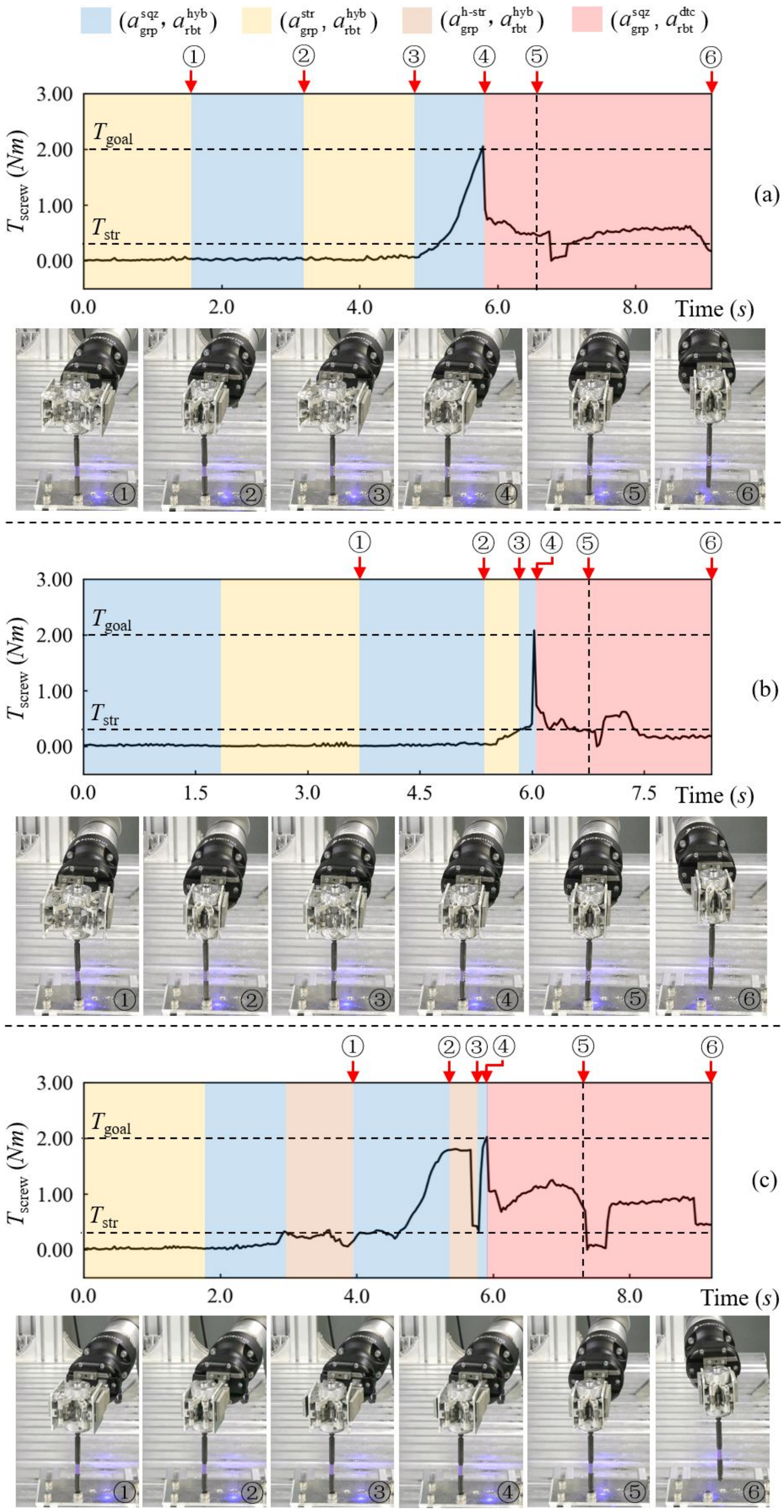

Figure 4.32: Changes of control policies and T_{screw} during fastening a single-start M8 screw. (a), (b), (c) are three different cases. The key time instants and their correspondent gripper states are marked using circle numbers. Especially, ⑤ denotes the changes from admittance control to hybrid control in $a^{\text{dtc}}_{\text{rbt}}$.

finish fastening.

Besides the shown results, we performed multiple examinations using single-start M8, M6, and M4 screws with different T_{goal} (T_{screw} remains unchanged). We set T_{goal} to range from $0.60Nm$ to $3.60Nm$ with $0.50Nm$ intervals. At each T_{goal} value, we perform 10 times of fastening tests. Success is judged when the given T_{goal} is reached and a tooltip is completely detached from a screw head. Under the mentioned settings, all our tests succeeded. The most negative result we observed is that the compliant motion made the tool inclined, but the inclination did not lead to failure. We conclude that the proposed policy-section algorithm is robust to single-start screws.

Recognition Precision

The tool accuracy of visual recognition is influenced by three factors[5]: (1) The precision of the sensor's point cloud; (2) The precision of model registration algorithms; (3) The absolute precision of the robot. The depth sensor we used in our experiments is a Photoneo PhoXi 3D Scanner M. Its calibration accuracy is less than $0.5mm$. The method of model registration has less than $0.5mm$ errors. The UR3e robot's absolute precision is around $0.1mm$. Considering all the error factors, the total tool pose accuracy is around $1.0mm$.

[5]Here we assume the difference between a real object and its 3D CAD model is ignorable.

4.5.3 Real-World Tasks

We use several real-world tasks to demonstrate the advantages of the tool. The video clips of our dual-UR3e robot performing these tasks are available in the supplementary.

Flexibility in planning

First, we program the robot to conduct fastening tasks using the tool. We compare the proposed mechanical screwing tool's flexibility with a conventional pneumatic screwdriver widely used in the manufacturing industry. In the case that the robot uses the pneumatic screwdriver, as shown in Fig.4.33, the robot has difficulty in dealing with the vacuum tube. The vacuum tube may knock down the spray bottle placed in the workspace during the manipulation, as shown in Fig.4.33(a.1). Also, the robot may get entangled with the vacuum tube during manipulation, as shown in Fig.4.33(a.2). Ingenious modeling algorithms and motion planners must be developed to avoid these problems.

Contrarily, since our tool is mechanical, it does not have any "tails" like electric cables, signal wires, or vacuum tubes. There is thus no need to consider their influences. Fig.4.33(b) exemplifies a fastening task using the proposed tool. When the robot cannot directly move the tool to the goal for screwing, a handover between the two grippers is used to reorient the tool to the expected pose.

We also compare the ability of the tool to fasten a screw in a narrow space. Fig.4.34 shows the scenario. The robot cannot use commercial tools to work in the narrow space shown in the scene. It is even not convenient for humans to use a commercial hex wrench, as shown in Fig.4.34(a). In contrast, the proposed

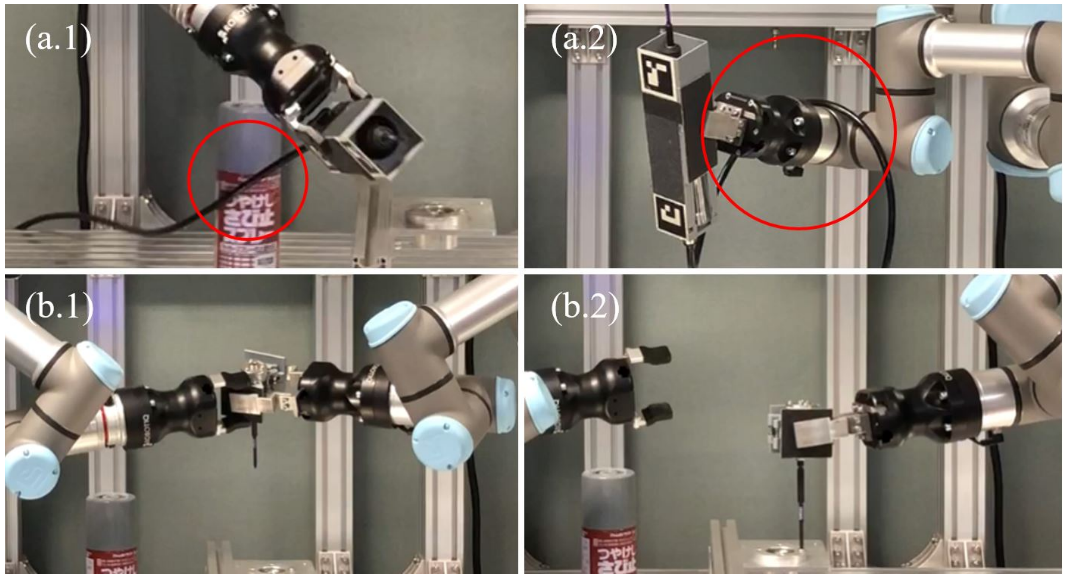

Figure 4.33: (a.1,2) Examples of the problematic cables. (b.1,2) The tool is cableless. Manipulation planning with it is easier.

tool is compact and has many tool-control grasp poses, and it can work in the narrow space to fasten the screw, as shown in Fig.4.34(b).

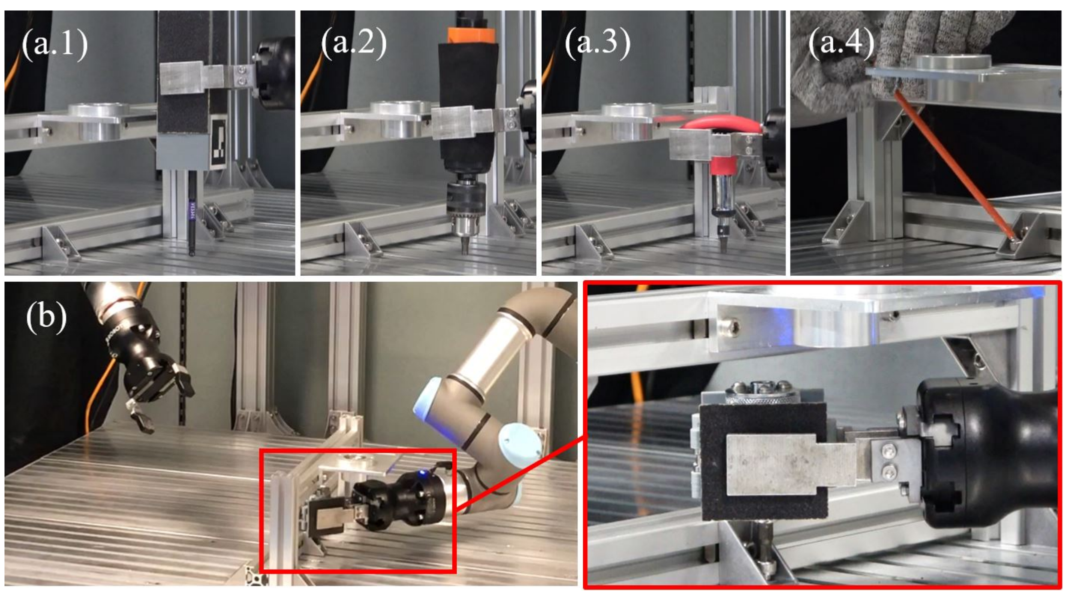

Figure 4.34: (a.1-3) Working in a narrow space is difficult. (a.4) It is even inconvenient for humans. (b) A robot can perform the task by properly grasping the proposed tool.

Multi-tool collaboration

Second, we demonstrate two robot arms can use multiple tools together to conduct tasks that cannot be done using a single special-purpose end-effector. The tasks include: (1) Using a tweezer tool [72] [148] to pick up a screw and using the screwing tool to fasten it; (2) Using a gearbox tool to accelerate screwing speed or increase maximum output torque.

Collaborative bolt picking and screwing For this task, one arm of the robot uses a tweezer tool to pick up and align screws, and the other arm uses the screwing tool to fasten the aligned screws. The tooltip of the tweezer tool is carefully designed for picking and alignment [148]. A robot arm may tilt the tool to slide a picked screw to a corner of the tooltip, and thus precisely align the screw and a threaded hole, as shown in Fig.4.35(a.1,2). To move the tools to pick-up and screwing poses, we follow Section VI.B to build two reasoning graphs and plan the grasp and manipulation motion sequences by searching them. Using the planned sequences, the two robot arms can manipulate the two tools and reorient them to their goal poses. After that, the arm manipulating the tweezer tool picks up a screw and aligns it to a screw hole. The arm manipulating the screwing tool inserts the screwing tooltip to the aligned screw head for fastening. Fig.4.35(a.3) shows a picture of the collaborative screwing process.

Assisting gearbox tool In the second task, we use a gearbox tool to increase or decrease the screwing tool's output. In the beginning, the screw is loose and the gearbox tool is used as a speed increaser to rotate it quickly. When the

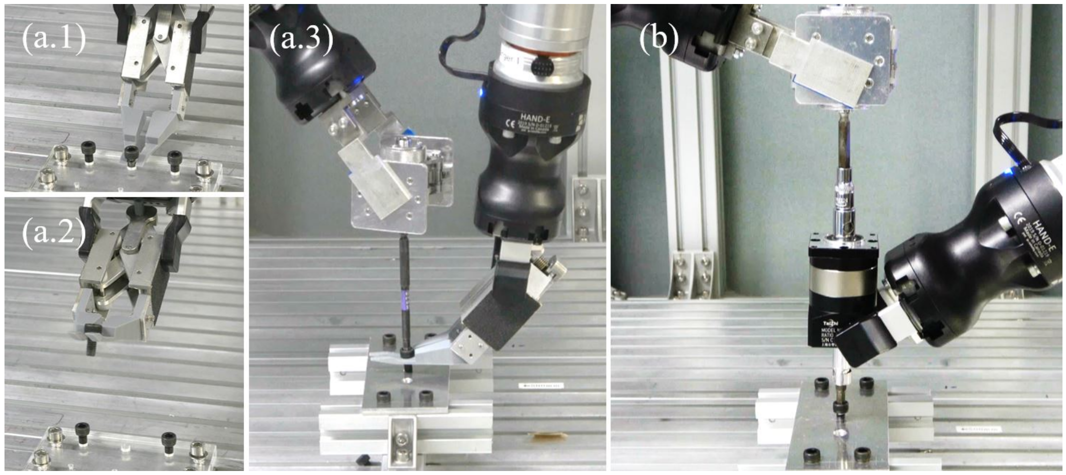

Figure 4.35: (a.1,2) Using the tweezer tool to pick a small screw. (a.3) Collaborative alignment and screwing. (b) Using a gearbox tool to accelerate the rotating speed or increase the maximum output torque of the screwing tool.

screw gets tight, the robot reverses the gearbox tool to reduce rotating speed and increase the output torque. The high output torque will firmly fasten the screw. Fig.4.35(b) shows a picture of the collaboration.

4.6 Summary

This chapter presented the optimal design and manipulation policies of a mechanical screwing tool for 2-finger parallel grippers. The tool can convert linear motion into rotational motion and thus can be used by robots with parallel grippers to fasten screws. Two mC-SLEs and a double-ratchet mechanism are employed in the design. Force analysis and geometric constraints are considered to make the tool have effective transmission capabilities and a compact structure. Manipulation and control policies are developed to exchange the tooltips, plan grasping and manipulation sequences, and detect and complete fastening tasks. Experiments showed a prototype of the designed tool has a good expected performance. Robots can use the tool and also several other tools together to conduct screw fastening tasks. The design is compact, cordless, and flexible. The developed manipulation policies are robust and effective.

In the future, alike tools are expected to replace the current special-purpose end-effectors or tool changers and be provided to general robot arms for complicated manipulation tasks.

Chapter 5

Manipulation for Uncertainty Elimination

Uncertainty is a crucial problem to employ robotic manipulators for assembly tasks. Especially for autonomous manipulators that receive vision feedback and generate manipulation motion online, uncertainty is challenging to eliminate – They originate from a series of mutually coupled components like vision, control, contacts, etc. Overcoming them and achieving precise manipulation is tricky.

Contemporary literature tends to solve the uncertainty problem using multimodal sensing and improved sensing algorithms. Related articles reported significant improvements in robotic perception [149]. However, despite the achievements, the improvements in sensing technology still fail to provide sufficient qualifications for autonomous manipulators, as sensing is not the only reason for uncertainty. On the other hand, researchers in the robotic planning and control community developed sophisticated integral motion planning and control policies to enable robots to correct object poses during manipulation. The policies include but are not limit to scanning search, spiral research, impedance control, hybrid force/position control, etc. [150] [148] [151], which need force sensors [152], tactile sensors [153] [154], or current sensors for feedback. Compliant mechanisms are hardware alternatives of the policies [155] [156]. They are effective and less expensive counterparts of the sensor-based implementation. The policy-based methods or the compliant mechanisms have advantages in regulated scenarios but tend to be influenced by environmental changes. Users need to adjust various parameters or key hardware components like springs for different applications. Unlike methods that improve robotic perception and control or develop new compliant mechanisms, eliminating uncertainty through manipulation while considering geometric and physical constraints is more straightforward, robust, and cost-effective. The fundamental idea is deploying a fixture in the robot workspace. The pose of a workpiece can be precisely aligned and determined by taking advantage of the geometric constraints induced by contacting the fixture and the physical constraints induced by gravity. The idea is not new. It is widely seen in factory automation for aligning randomly placed workpieces [91] [157], and has been practiced since the beginning of robotics. This paper reinspects the idea of employing a fixture to reduce uncertainty. Different from the conventional design and mechanical analysis, our focus is on the planning aspect. We develop algorithms to compute an object's stable poses on a fixture and employ these poses as intermediate states to build manipulation graphs and plan robotic manipulation sequences. With the help of the stable intermediate poses on the fixture, the uncertainty in planned manipulation sequences can be reduced. A workpiece is manipulated precisely, and the manipulation results can be directly used to conduct difficult tasks like insertion. In detail, the fixture used in our study is a triangular corner fixture, which is comprised of three mutually orthogonal planes, as shown in Fig. 4.1. Driven by gravity, a workpiece dropped from above the tilted corner fixture may firstly contact the inner surfaces and then slide to the bottom under gravity and the guides of the mutually orthogonal planes. The workpiece will rest at a particular pose at the bottom of a gravitational bucket formed by the fixture.

Previously, dropping a workpiece onto a tilted corner for regrasp and reducing pose uncertainty was widely used in the automation industry. For practical purposes, the robot motion for a successful dropping was manually specified. Their stability relied on a system integration engineer's subjective adjustments and examination. The method developed in this work automatically finds the Stable Placement Poses (SPPs) of an object on a Triangular Corner Fixture (TCF) and consequently enables auto-planned precise robotic regrasp and manipulation. The method first computes the SPPs considering geometric contact constraints, physical feasibility, and static stability. Then, it elevates the object from its SPPs to dropping poses and finds the Deterministic Dropping Poses (DDPs) from them. When the object is released from the DPPs, it will rest at expected SPPs. Finally, the method computes the gripper configurations for grasping and regrasping the object considering the TCF, SPPs, and DDPs. The method will output a pick-and-place sequence that manipulates the object with the help of the TCF by high precision. In the experiments, we study the performance of different methods for estimating the DDPs of different objects and quantitatively examine the proposed method's ability to eliminating uncertainty by inserting a peg into holes with different clearance. We also examined the method's practical performance using real-world assembly tasks like peg-in-hole insertion, sheathing tubes, aligning holes, and mounting housings, etc. The results verify that the method enables a robot to finish assembly tasks without using sensors, compliant control, or complicated mechanism, making the robot system more robust and flexible.

5.1 Preliminaries and Method Overview

This section explains the background knowledge of a TCF, and presents the outline of the proposed method.

5.1.1 Background knowledge of a TCF

A Triangular Corner Fixture (TCF) is made of three inclined plates intersecting at one bottom point, as shown in Fig. 5.1(a). The three inclined flat plates form a gravitational basket [158] that holds a dropped object at a stable pose. Compared with a flat surface, the plates of a TCF can always pull a dropped object into configurations with minimal potential energy in the gravitational field.

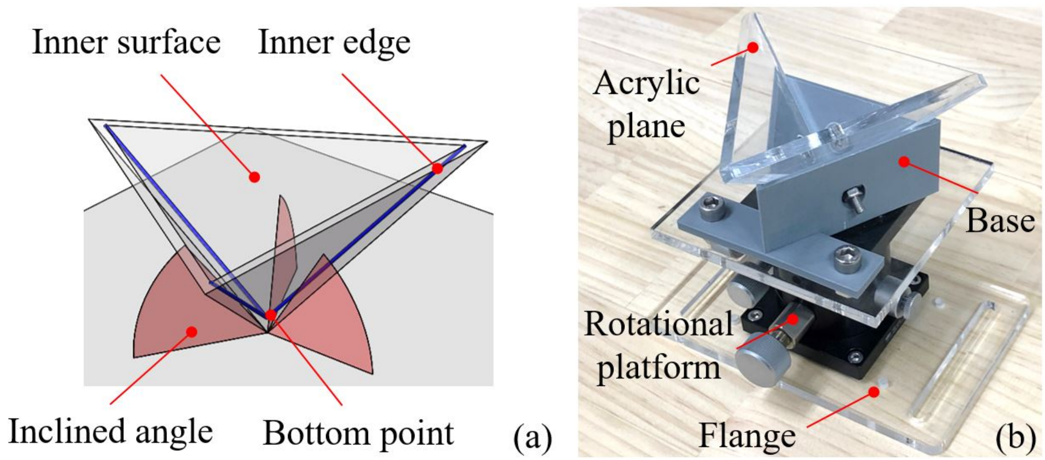

Figure 5.1: Structure of a Triangular Corner Fixture (TCF).

Especially, the plates of the TCF used in this paper are mutually perpendicular. The reason we study this special case is that our goal is to assemble mechanical workpieces precisely. Although these workpieces have different shapes, they comprise geometric primitives like a cylinder, cuboid, ball, wedge, etc., and have three mutually perpendicular surfaces. We thus propose using a TCF made of three mutually perpendicular plates as an intermediary fixture to hold them. Fig. 5.1(a) shows the structure of the mentioned TCF. Its three plates are fabricated as three congruent isosceles right triangles. The angles between the triangular plates and a horizontal plane are the same (54.74°). Figs. 5.1(b) shows a real-world fabrication. The three triangular plates are made of acrylic boards and are detachable from the base. The isosceles length l_e of the triangular plates are equal. Since they are detachable, the l_e can be changed, and the TCF dimensions can be adapted for parts of different scales. The TCF base is mounted on a 3-axes rotational platform for fine-adjustment. The platform bottom has an adapter plate for connecting with other fixtures.

5.1.2 Method Overview

We develop a planner that estimates the robust dropping poses and stable placements of an object in the mentioned TCF and hence finds the regrasp motion that leads to precise assembly. Fig. 5.2 shows the workflow of our proposed planner. It receives the meshed models of the target object, the robotic gripper, and the TCF as the input. Three sub-modules will use the input: the Stable Placement Pose (SPP) planning sub-module, the Deterministic Dropping Pose (DDP) estimation sub-module, and the grasp configuration planning sub-module, respectively, to find stable placement poses, estimate robust dropping poses, and plan gripper configurations. Specifically, the SPP sub-module computes a set of stable placement candidates of a given object that satisfies geometry constraints and is statically stable in the TCF. The DDP estimation sub-module uses a classifier to predict if an object dropped from an elevation position can be aligned to the expected SPP and finds a set of SPP-DDP pairs. The grasp configuration planning sub-module computes the gripper configurations for releasing an object at the DDPs and regrasping the object at the SPPs in the found SPP-DDP pairs. These computed releasing and regrasping gripper configurations are used to build a regrasp graph to reason a robot motion sequence. The details of the three sub-modules will be explained in Sections V-VII.

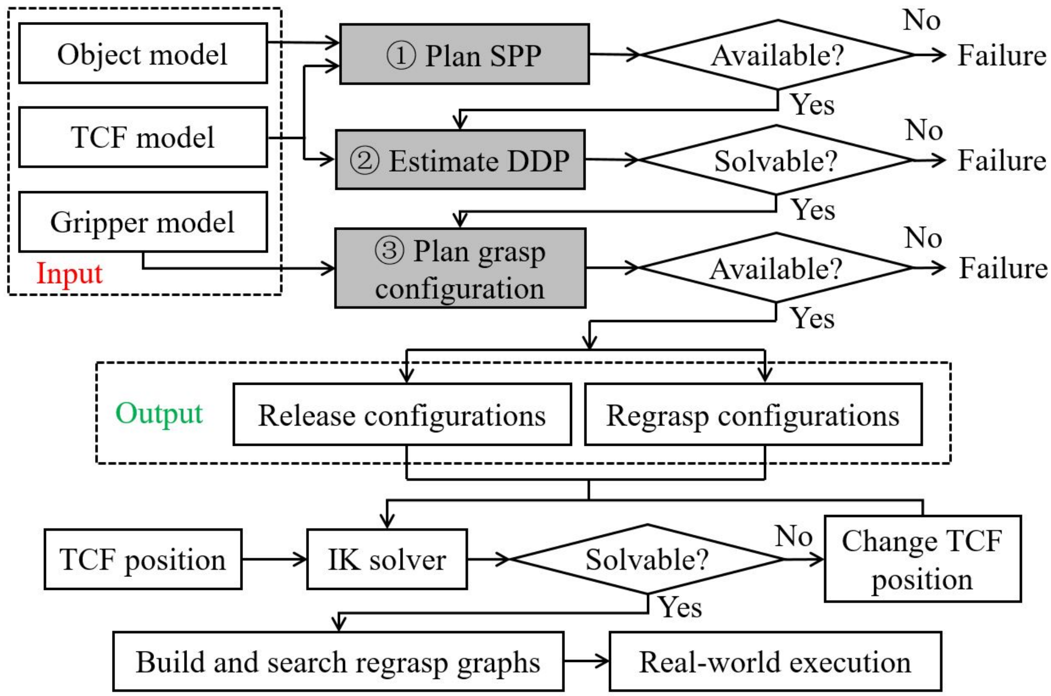

Figure 5.2: Workflow of the proposed planner.

5.2 Plan Stable Placement Poses

We define an SPP as follows: An object is at an SPP when it stays in the triangular corner fixture in a balanced static condition. We use the algorithm shown in Fig. 5.3 to plan the SPPs. The algorithm receives an object and a TCF model as input and returns all satisfying SPPs as output. It comprises three steps which are highlighted using diamonds and blocks of different colors in Fig. 5.3. The first step includes the blue diamonds and blocks. In this step, the algorithm clusters the faces of the object's mesh model into facets and computes their triple combinations. The triplets of facets are the candidate contact faces with the inner surface of the TCF. The second step includes the yellow diamonds and blocks. In this step, the algorithm uses the triplets of facets to compute the object poses in the TCF. The triplets of facets must be in contact with the TCF's inner

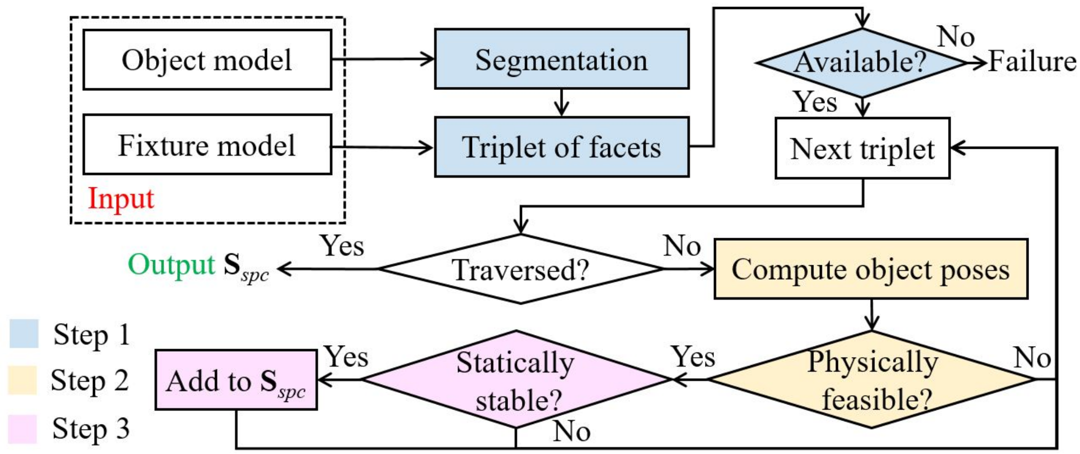

Figure 5.3: Plan the SPPs. The digram is a close-up view of the "Plan SPP" sub-module in Fig. 5.2.

surface during the computation. Meanwhile, the object models are required to be not penetrating the TCF and the surrounding environments. The third step includes the pink diamonds and blocks. The algorithm in this step examines the static stability of the object poses computed in the second step and discards the unstable ones. The details of these three steps are presented below. We only consider face-to-face contact between the object and the TCF as effective contact candidates in the algorithm. Although a point-to-face or line-to-face contact can also stabilize an object, they are less reliable and ignored to simplify the planning algorithm.

5.2.1 Step 1: Facets and Their Triplet Combinations

In this step, the algorithm clusters triangle faces of an object's mesh model $\mathcal{M}_o$ into facets and then uses the facets to find mutually perpendicular triplet combinations.

Using conventional segmentation methods to cluster facets may lead to uneven area [159]. Instead of the conventional methods, we use superimposed segmentation [160] to generate uniform facets. The method especially has better performance when handling curved surfaces. Take the T-shape pipe junction object shown in Fig. 5.4 for example. The mesh model of the junction is shown in Fig. 5.4(a). The segmented superimposed facets are shown in Fig. 5.4(b). For a mesh model $\mathcal{M}_o$, we denote its superimposed facet set using $\mathbf{S}_o = \{s_i\}$ $(i = 1, 2, ...m)$, where each s_i indicates a facet.

After getting the facets, we find the mutually perpendicular triplet facet combinations. Here, we assume to only consider the face-to-face contacts between an object and the TCF, and thus ignore the edge and vertex contact. The details of our workflow is as follows. With all segmented facets, we combine every three surfaces into a triplet and get a collection of triplets $\mathcal{S}_g = \{\mathbf{S}_g(j) = \{s_a, s_b, s_c | s_a, s_b, s_c \in \mathbf{S}_o\},\ j = 1, 2, ...C_m^3\}$. Then, we examine the orthogonality of each triplet's facet normal. The one that has three mutual orthogonal normal is considered as a feasible candidate, as illustrated in Fig. 5.4(c). We use $\mathcal{S}_g^{'} = \{\mathbf{S}_g^{'}(i) = \{s_a, s_b, s_c | (s_a \perp s_b, s_a \perp s_c, s_b \perp s_c)\},\ \mathbf{S}_g^{'}(i) \in \mathcal{S}_g\}$ to denote the feasible candidate collection. The workflow can be accelerated using linear programming to avoid repeatedly examining the impossible combinations.

5.2.2 Step 2: Computing Transformations

In the second step, the algorithm computes the transformation that fits the triplet facets onto the inner surfaces of the TCF. We use $\{C_o\}$ and $\{C_f\}$ to respectively represent the object frame and the TCF frame, and use $\{C_o^{'}\}$ to denote the

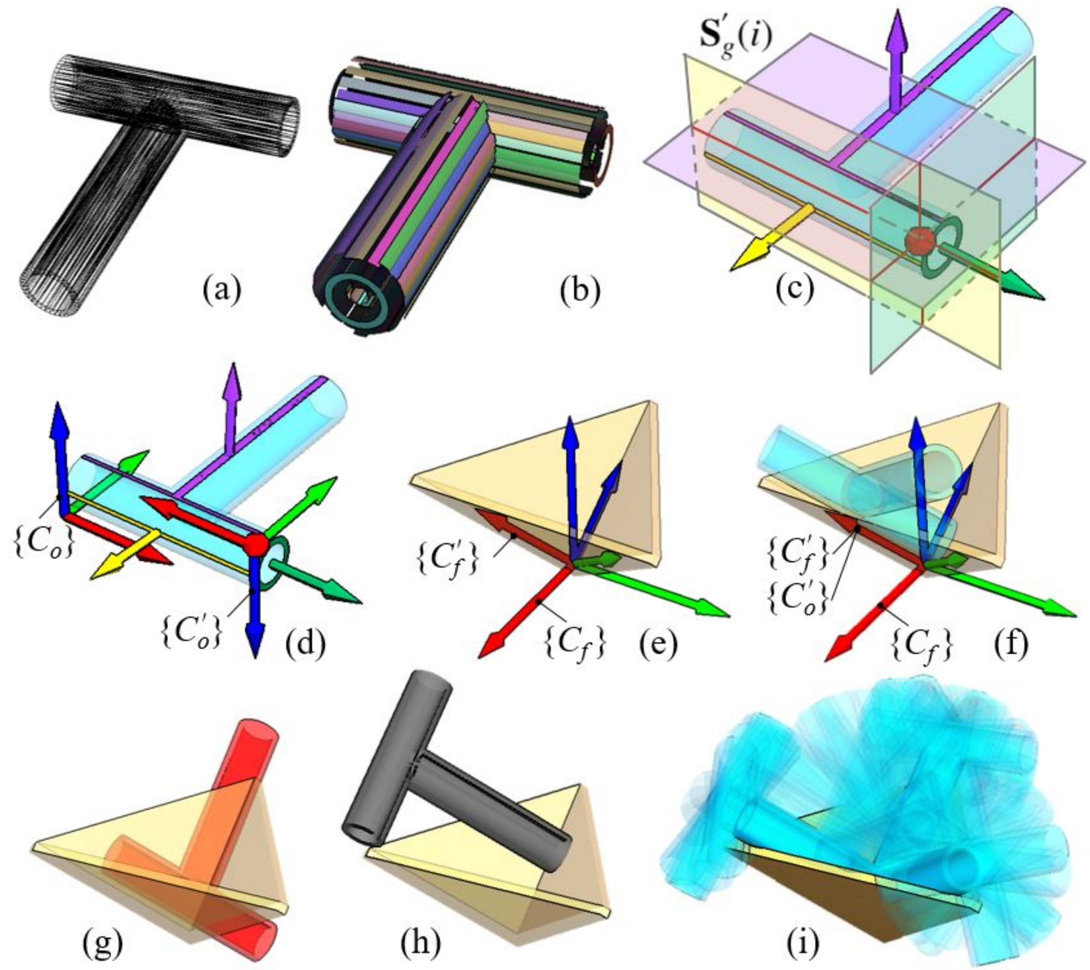

Figure 5.4: (a) A raw meshed model. (b) Segmented surfaces. (c) A candidate triplet of facets. It has three mutual orthogonal surfaces. (d) The object's frame ($\{C_o\}$) and the object-to-TCF transformation coordinate described in it ($\{C_o'\}$). (e) The TCF's frame ($\{C_f\}$) and the object-to-TCF transformation coordinate described in it ($\{C_f'\}$). (f) A placement pose of the object on the TCF. (g) The first failure case: Penetration. (h) The second failure case: Phantom contact. (i) All planned LFPs.

local frame of $\mathbf{S}_g'(i)$. The intersection point of $\mathbf{S}_g'(i)$'s three orthogonal facets are selected as $\{C_o'\}$'s origin. Its coordinate axes are determined considering the inverted normal directions of the facets (The exact x, y, and z choices are free, as long as they meet the right-hand rule). Fig. 5.4(d) illustrates a $\{C_o'\}$ defined considering the $\mathbf{S}_g'(i)$ shown in Fig. 5.4(c).

Next, we compute the placement pose of an object by transforming its $\{C_o'\}$ onto TCF. We define two coordinate systems for the TCF. One is $\{C_f\}$. Its origin is at the bottom point of the TCF, and its orientation is the same as the world coordinate system. The other one is $\{C_f'\}$, which has the same origin as $\{C_f\}$ but the x, y, z axes are along the intersection edges of the TCF's perpendicular surfaces. The placement poses of the object can be computed by superposing $\{C_o'\}$ to $\{C_f'\}$, which means if we use a transformation matrix ${}^{C_f}_{C_o}\mathbf{T}_i$ to denote the placement pose, it can be computed as ${}^{C_f}_{C_o}\mathbf{T}_i$=${}^{C_f}_{C_o}\mathbf{T}_i{}^{C_o}_{C_o'}\mathbf{T}_i$=${}^{C_f}_{C_f'}\mathbf{T}_i{}^{C_o}_{C_o'}\mathbf{T}_i$. An object may have many $\mathbf{S}_g'(i)$ and thus many ${}^{C_f}_{C_o}\mathbf{T}_i$. We name ${}^{C_f}_{C_o}\mathbf{T}_i$s the Potential Placement Poses (PPPs). Fig. 5.4(f) illustrates one PPP of the T-juction object.

Note that the potential ${}^{C_f}_{C_o}\mathbf{T}_i$ may not be logically feasible since we did not check interference and contact. The object may penetrate the TCF, as shown in Fig. 5.4(g). It may also be floating in the air as the size of the TCF is limited and the contact is phantom (Fig. 5.4(h)). Thus, at the end of the second step, we screen the PPPs by detecting collisions and the existence of contact and removing the logically infeasible ones. We get a set of Logically Feasible Poses (LFPs) after the screening, as illustrated by Fig. 5.4(i).

5.2.3 Step 3: Examining the Static Stability

In the third step, we further use Contact Wrench Space (CWS) analysis to examine the static stability of the LFPs and obtain the SPPs. For a clear illustration, we use an L-shape object instead of the T-junction to exemplify this step. The workflow is as follows.

First, we extract the contact polygons between the object and the TCF's inner surfaces. Each of the three TCF inner surfaces has a contact polygon set, which may have a single or multiple elements. We compute the convex hull of the contact polygons in each set to get three support polygons for the three inner surfaces. The SP1-3 in Fig. 5.5(a) illustrate the three support polygons of the L-shape object. Second, we consider the vertices of the three support polygons as the effective contact points that provide supporting forces for the object, compute a wrench cone formed by the wrenches exerted on them and the object's gravity, and judge the stability of the object using the relation between the wrench cone and the origin of the wrench space. The yellow spheres in Fig. 5.5(a) illustrate the effective contact points. Assume there are in total k effective contact points $\boldsymbol{p}_i = [x_i, y_i, z_i]$, $(i = 1, 2..., k)$. We build a local frame at each of the $\boldsymbol{p}_i$s to describe the contact force. The x and y axes of the local frame compose a tangent plane on the contact point, and the z axis aligns with the normal of the TCF's inner surfaces, as shown in Fig. 5.5(d). The contact force at p_i can be represented by the components along the three axes as $\mathbf{f}_i = [f_{xi}, f_{yi}, f_{zi}]^T$. The effect wrench exerted on p_i can be computed using $w_i = \begin{bmatrix} \boldsymbol{I} & 0 \\ [\mathbf{p}_i \times] & \boldsymbol{I} \end{bmatrix} \begin{bmatrix} \mathbf{f}_i \\ \tau_i \end{bmatrix}$, where τ_i indicates the exerted torque. Considering the frictional constraints at the contact point, $\mathbf{f}_i$ must be in a friction cone and f_{xi}, f_{yi}, and f_{zi} must meet $\sqrt{f_{xi}^2 + f_{zi}^2} \leq \mu f_{zi}$, where μ is the friction coefficient. Since $\mathbf{f}_i$ is inside a cone and is not deterministic, directly using the equation to compute wrench cone is difficult. To overcome the difficulty, we approximate the friction cone with a pyramid [161], as shown in Fig. 5.5(b.2-3). The lateral edges of the pyramid represent the extreme $\mathbf{f}_i$ choices. They are named as $\mathbf{f}_i^j$, where the granularity of the approximation determines j. A linear combination of the $\mathbf{f}_i^j$ could approximate a freely chosen $\mathbf{f}_i$ in the friction cone. With this consideration, we represent w_i using multiple values $w_i = \{w_i^j\}$ and use all w_i^j to compute the wrench cone. Each w_i^j will be the wrench from one $\mathbf{f}_i^j$. Considering all of them for wrench cones is the same as considering linear combination of the $\mathbf{f}_i^j$. The wrench set $\mathbf{W}$ born by the object comprises the $\{w_i^j\}$ at every p_i and the object's center of mass. It can be expressed as $\mathbf{W} = \{w_1^j\} \cup ... \cup \{w_k^j\} \cup \{w_g\}$, where w_g denotes the gravitational wrench. The wrench cone $\mathcal{W}_s$ spanned by the wrench is essentially a convex hull of the elements in $\mathbf{W}$ [114]. The stability of LFPs is judged by examining the relationship between the origin of the wrench space and $\mathcal{W}_s$[1]. If the origin is inside the $\mathcal{W}_s$ of an LFP, the LFP is considered to be stable and will be counted as an SPP. The planner will look over all LFPs and find a set of SPPs.

5.3 Estimate Deterministic Dropping Poses

If an object released from a pose on top of the TCF has a deterministic and expectable SPP when it gets stabilized inside the TCF, we call the releasing pose a Deterministic Dropping Pose (DDP). This section presents methods to estimate if the SPPs obtained in the last section have correspondent DDPs. The methods

[1]The magnitude of all elements in $\mathbf{W}$ is set equally as 1 when computing the $\mathcal{W}_s$ since we assume unknown masses.

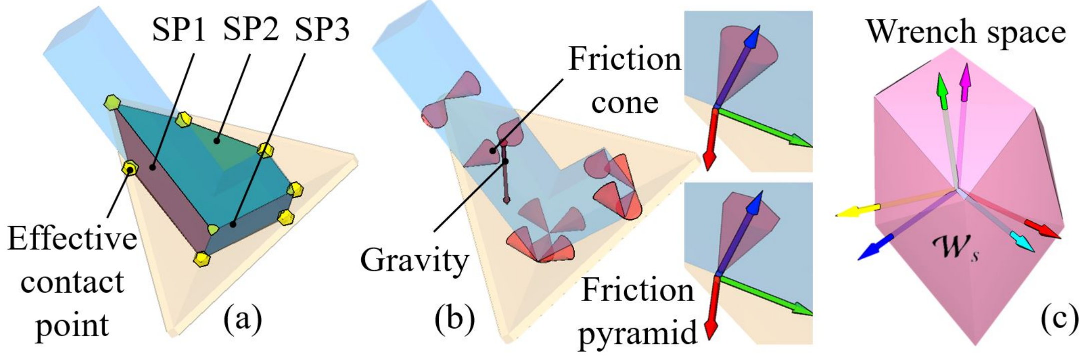

Figure 5.5: (a) Support polygons and contact points formed by the contact between the object and the TCF. (b) Friction cones and gravity exerted on the object. The friction cone is simplified as a hexagonal pyramid. (c) Wrench cone $\mathcal{W}_s$ in the wrench space.

are based on the assumption that a candidate DDP is a pose linearly elevated from an SPP. The elevation height h_e ranges from h^- to h^+, as shown in Fig. 5.6. We elevate an SPP to a random height in $[h^-, h^+]$ to get candidate releasing pose and use the methods presented in the following subsections to estimate if the object deterministically stabilizes at the SPP after being dropped from the releasing pose. If the algorithms suggest a positive predicted result, we save the SPP and the releasing pose as an SPP-DDP pair. All saved SPP-DDP pairs will be used for reasoning and planning the regrasp sequences to improve grasping precision.

Specifically, we propose two methods for the estimation. The first is an analytical method based on CWS, and the second is a learning-based method. Their details are as follows.

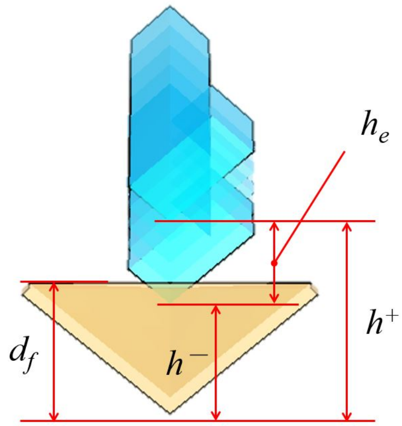

Figure 5.6: Visualization of the elevation height h_e and its effective range $[h^-, h^+]$. The d_f is the depth of the TCF. It is not mentioned in the main text. We choose h^- to be a bit lower than d_f and choose h^+ to be outside d_f to take into account various possibilities.

5.3.1 Analytical Method

In the first method, we predict the SPP by considering a static stability criterion, which screens an SPP considering its capability of resisting external disturbance wrenches. The method is based on an intuition that an SPP with larger stability is more likely to have a DDP than a less stable one.

Similar to the third step of planning SPPs, the analytical method uses CWS to evaluate static stability. However, instead of directly generating convex hull of contact wrenches to span the wrench space, the method constructs the wrench cone by computing the convex hull of $\mathbf{W}$'s Minkowski sum. We use the notation $\mathcal{W}_{mkv}$ to differ the wrench cone in this section from the $\mathcal{W}_s$ used before. Compared to $\mathcal{W}_s$, $\mathcal{W}_{mkv}$ can quantify the resistible external wrench, thus make it easier to decide an evaluation criteria [114]. In particular, the method computes the shortest distance from the origin of the wrench space to the hyperplanes that constitute $\mathcal{W}_{mkv}$ and uses the shortest distance as the stability quality. Then, the method finds the SPPs that have enough stability quality from the obtained SPP set and elevate them to get DDPs.

The static stability criteria-based analysis may find the DDPs with large determinism from the SPPs of an object. However, the stability quality of different objects cannot be measured on a unified scale, making it difficult to set a unique threshold for a general estimation. Also, the criterion is based on intuition and is not fundamentally true. The DDPs may have uncertainty (positional and rotational noises, and also bouncing) in the real world, which are not considered by the method and may invalidate the intuition. For these reasons, more advanced methods need to be explored.

5.3.2 Learning-Based Method

In the second method, we use machine learning to predict DDPs. We use a sim-to-real method [162] to obtain the training data and train different classifiers to judge if an SPP has a correspondent DDP.

Training data

The training data comprises a data section and a label section. The data part comprises the contact polygons, the position of the object's CoM, and the support surfaces of the TCF. They are projected onto a horizontal plane and formulated as a 2D grayscale image shown in Fig. 5.7 to simplify numerical computation. In detail, we assume a grayscale image with 224×224 pixels. The background of the image is white (grayscale value: 255). The regions of the projected support polygons and the contact polygons are set to 220 (support surfaces) and 0 (contact polygons). The projected CoM is formulated as a circular patch. Its color is computed using $v_{grey} = \phi \cdot h_{com}$, where ϕ is the ratio between a real-world distance and the numbers of image pixels used to represent it, h_{com}

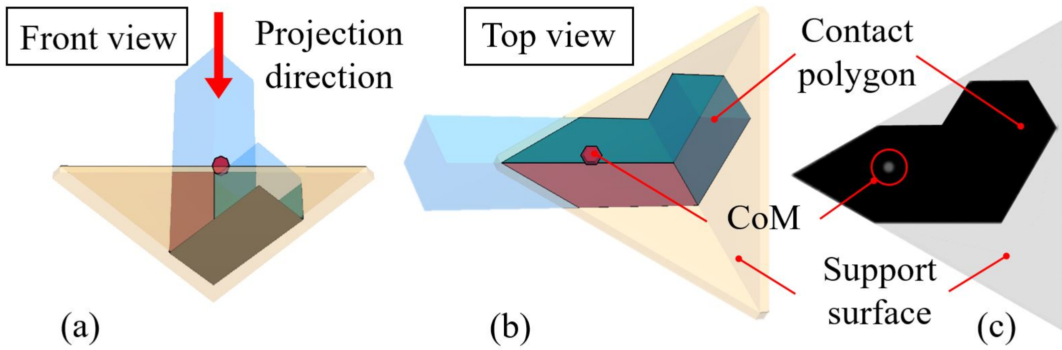

Figure 5.7: An SPP shown in (a) is converted into a grayscale image in (c) by using the top view shown in (b).

indicates the vertical distance from the CoM to the bottom point of a TCF. The v_{grey} essentially normalizes h_{com} considering the dimensions of the TCF and the image.

The label section is collected by physical simulation. We place a work table and a TCF in simulation and generate the candidate releasing poses by randomly elevating an object from their SPPs, dropping the object from the candidate poses, and examining the finally stabilized poses. Unlike the analytical method, we add noises to the releasing poses to take into account uncertainty. The object falls from the releasing poses with random noises, and we compare the object's stabilizing CoM with the CoM of the expected SPP when it gets stabilized. If the two CoMs coincide, a successful trial is recorded. Otherwise, a failure is recorded. Here we use the CoM as the reference to avoid misjudging symmetric objects with small support surfaces (e.g., balls and cylinders). The configurations of these symmetric objects are considered to be identical when moving around the symmetry center. By comparing the CoMs instead of the configurations, we may avoid misjudging the identical configurations. We run 100 trials for each releasing pose and compute a success rate. If the success rate is more significant than a given threshold, the releasing pose will be labeled as a positive sample.

Classifiers

Using the training data collected in the last section, we train classifiers to predict if the object dropped from a releasing pose can rest at an expected SPP. The classification is a simple binary one since there are only two labels. Various methods like Support Vector Machine (SVM), Fully Connected Network (FCN), and Convolutional Neural Network (CNN) can be used to model the classifier. Specifically, we implement and compare a linear SVM, a four-layer FCN, and an Alexnet-CNN. The detailed results and discussions about the implementation and comparison will be presented in Section.VIII-B.

5.4 Plan Grasp Configurations and Regrasp Sequences

This section presents detailed releasing and regrasp planning algorithms for adjusting grasping precision. The algorithms are partially based on our previous work published in [160] and [163]. First, we plan grasps configurations for an object without considering any obstacles using the methods presented in [160]. Then, based on the planned grasp configurations, we generate two sets of grasp configurations for the SPP and DDP in each SPP-DDP pair while considering different levels of collisions. Finally, we build a regrasp graph [163] by reasoning and connecting the grasp sets associated with all SPP-DDP pairs, and search the graph to obtain regrasp sequences.

Fig. 5.8 and 5.9 exemplify the above workflow using the L-shape object. Fig.5.8(a) shows the planned grasp configurations when there are no surrounding obstacles, and the object pose is aligned with the global frame. Fig. 5.8(b-c) show an SPP and its associated grasp configuration set. These grasps in the set are transformed from (a) along with the object pose. The grasp configurations that collide with the TCF after the transformation are removed. Fig. 5.8(d-j) show the DDP paired with the SPP and the procedure for generating its associated grasp configuration set. Fig. 5.8(d) is the DDP. Fig. 5.8(e) is the grasps transformed from (a), with the ones in collision with the TCF removed. Fig. 5.8(f) shows the swept volume of the released object. The grasps in (e) are further examined considering the swept volume. If an opening hand collides with the swept volume, the released object will collide with the hand when it falls onto the TCF, leading to an unexpected resting pose. Thus, we further examine the collision between the grasp configurations in (e) and the swept volume, and remove the collided ones. Fig. 5.8(g.1-2) and 5.8(h.1-2) show a collision-free and a collided examples respectively. The grasp configuration in Fig. 5.8(g.1) does not collide with the swept volume after releasing in Fig. 5.8(g.2). Contrarily, the grasp configuration in Fig. 5.8(h.1) get collided in Fig. 5.8(h.2). Fig. 5.8(i) highlights all collided grasp configurations in (e) with red color. Fig. 5.8(j) shows the remaining collision-free grasps.

Fig. 5.9 shows the regrasp graph built using the two grasp configuration sets in Fig. 5.8(c) and (j). The black maximally connected graphs in Fig. 5.9(a) and (d) show the transit relations among the grasp configurations associated with the initial and goal object poses. The black maximally connected graphs in Fig. 5.9(b) and (c) show the transit relations among the grasp configurations associated with the DDPs and their pairing SPPs. The blue edges among the maxi-

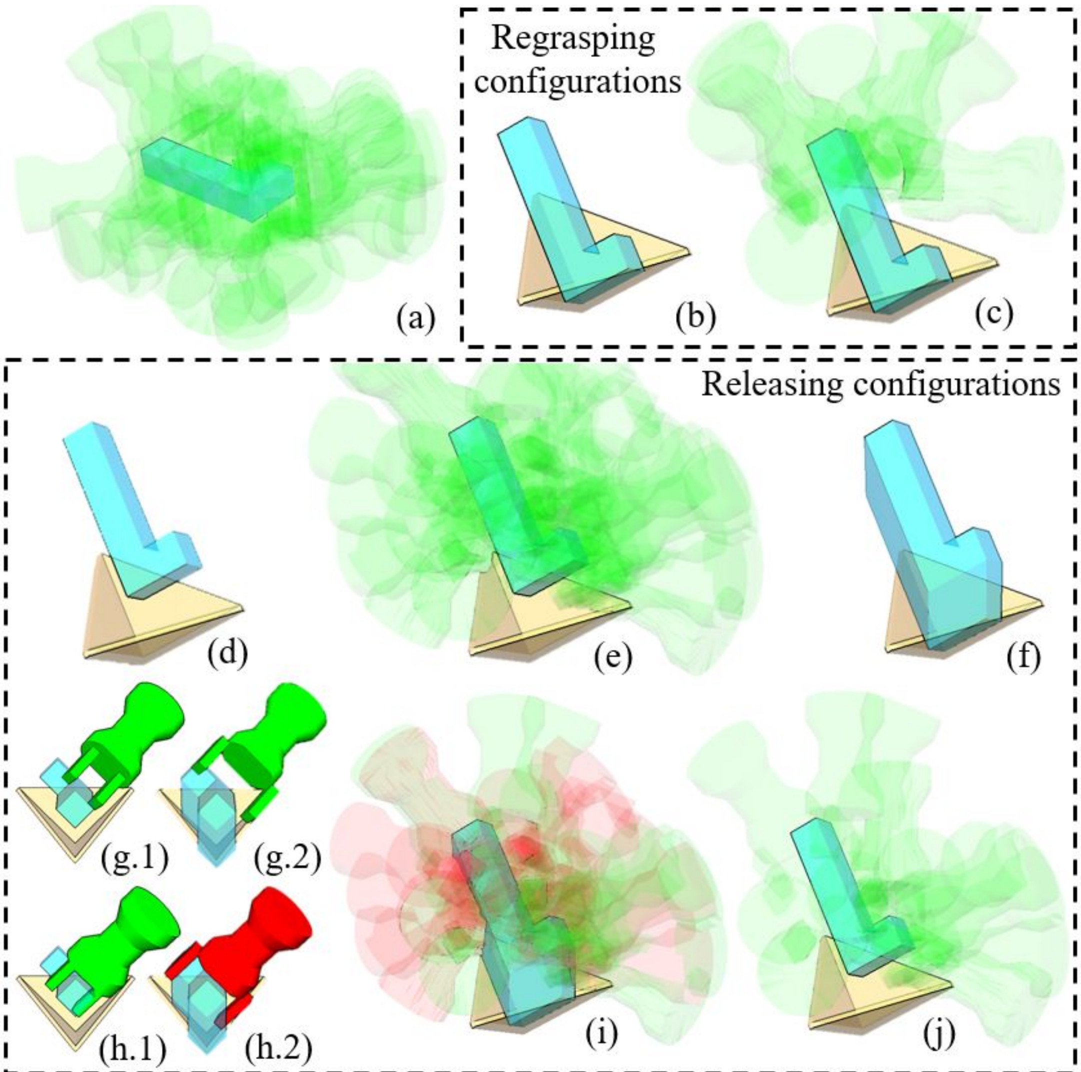

Figure 5.8: (a) Grasp configurations planned without considering any surrounding obstacles or pose changes. (b) An SPP. (c) The grasp configuration set associated with the SPP in (b). (d) A DDP. (e) Transformed collision-free grasps from (a), with the ones in collision with the TCF removed. (f) Swept volume of the dropped object. (g-h) Releasing hands may collided with the swept volume. (i) Grasp configurations that collide with the swept volume are highlighted in red and will be removed. (j) Grasp configurations associated with the DDP.

mally connected graphs show the transfer relations among the grasp configurations associated with different object states. The yellow edges represent strong connections between the black maximally connected graphs in Fig. 5.9(b) and (c). They indicate that a grasp configuration associated with a DDP can transit to another grasp configuration associated with its pairing SPP. To precisely regrasp the L-shape object, our planner will search a path on the graph by starting from one node in (a) (the initial grasp) and ending at another node in (b) (the final grasp). The path essentially maps to a sequence where the object will be grasped from the initial pose (a node in (a)), moved to a DDP (a node in (b)), dropped down onto the TCF and regrasped (a node in (c)), and finally moved to the goal (a node in (d)).

5.5 Experiments and Analysis

This section includes three parts. First, we compare the methods for estimating the DDP-SPP pairs. Second, we use the most satisfying method to perform regrasp and examine the regrasp precision. Third, we validate the benefits of the proposed method using real-world assembly tasks.

5.5.1 Comparison of the DDP Estimation Methods

We proposed one analytical method and three learning-based methods in Section V-B-2) for estimating the DDPs. In this subsection, we compare their performance using physical simulation. Especially for the learning-based methods, we use the 14 primitives shown in Fig. 5.10(a) to obtain the training data. The primitives are scaled from 50% to 150% with 10% granularity, as shown in Fig. 5.10(b), to obtain 154 objects. Using these objects, we get 4464 SPPs. We collect training data using these SPPs in a PyBullet-based physical simulator. According to the real-world model, the friction coefficient and the bounce rate between the object and the TCF in the simulator are set to 0.3 and 0.2. The inner edge length of the TCF is set to 50.0 mm. Its d_f is set to 28.0 mm. We collect the training data by repeatedly elevating the objects from the SPPs to random start positions between $h^- = 0.8d_f$ and $h^+ = 1.5d_f$ with maximally 3.0 mm positional and 3.0° rotational noises, and dropping them from the start position. When the objects get stabilized, we compare their CoMs with that of the source SPPs and label the results. Through the physical simulation, we collected 1770 positive samples and 2674 negative samples. 80% of the data is used to train the estimators with cross-validation used to verify the results. The remaining 20% is used for the test.

The results using different methods (including the analytical one) are shown in Fig. 5.11. The learning methods have better performance, of which the AlexNet shows the highest success rate (90.1%). The analytical method has poor performance because "finding the SPPs with enough stability quality" needs a threshold. For practical purposes, we only used the most stable configuration, which easily leads to ignored DDPs. Meanwhile, even if one configuration has the most stable stability, there is no guarantee that its elevated counterpart is a DDP. The DDPs found by the method may thus be unconvincing.

Besides the simulated data, we also validate the various methods using four real objects shown in Fig. 5.13. They include: (a) an L-shape object; (b) a T-junction; (c) a bracket; (d) a bearing housing. According to the object's size, we chose a 50.0 mm-TCF for the L-shape object and bearing housing, and a 70.7 mm-TCF for the bracket and the T-junction. For the learning-based method, we used the classifiers trained above to judge DDP-SPP pairs. For the analytical method, we use the most stable configuration. The results are shown in Table.

5.12. The table's ground truth values (Denominators of the "Unpaired" and "DDP-SPP" columns) are obtained by repeated physical simulation. There are 54 SPPs for the L-shape object. 6 of them have DDP-SPP pairs, as shown by the denominators of the L-shape object's "DDP-SPP" column. The remaining 48 does not have counterpart DDPs, as shown by the denominators of the L-shape object's "Unpaired" column. The numerators of the "Unpaired" column show the actual number of SPPs that do not have a DDP. The numerators of the "DDP-SPP" column show the actual number of SPPs that have a DDP. The T-junction has 72 SPPs, where 24 of them have DDP-SPP pairs, and the remaining 48 do not have DDP counterparts. The bracket has 12 DDP-SPP pairs and 42 unpaired SSPs. The bearing housing has 72 DDP-SPP pairs and 72 unpaired ones. The results show that the analytical method works effectively for the L-shape object and the bracket, but performs poorly for the T-junction object and the bearing housing. The learning-based methods are better on average but may have shortages for specific objects (i.e. the bracket). The AlexNet method is the best of all learning-based methods, which is consistent with the results shown in Fig. 5.11.

We further performed real-world dropping tests using the four objects. The process is as follows. First, we place the object with a selected SPP on the TCF. Then, the robot will grasp the object, elevate it to a DDP with random offset noises, and open the gripper to release the object. Finally, we observe the dropping process, check if the object gets stabilized at the selected SPP, and record the results. The process is repeated 30 times for each SPP to get a statistical view. Fig. 5.14 shows results. Due to page limits, it is impossible to show all SPPs and we only present some representative DDP-SPP cases for readers' convenience. The results indicate that the estimation mostly accords with the real-world results.

Since the analytical method had an extremely bad performance on the T-junction object and the bearing housing, we further analyzed the detailed contact between these objects and the TCF surfaces to understand the reason. We found the DDP-SPP pair that has the best SPP stability is like Fig. 5.11(b.3) and (d.2). These SPPs have high static stability qualities, but their contact areas are distributed around the objects' CoMs (as shown by the 2D grayscale images of the figure). A large section of an object is not in contact with the inner surface of the TCF. The object will have a low chance to stably "stand" on the distributed contact when being dropped. It may get stuck by the edges of the TCF.

5.5.2 Performance on Eliminating Uncertainty

In the experiments of this subsection, we use robotic peg-in-hole insertion tasks to evaluate the performance of the proposed method on eliminating uncertainty and compare it with the conventional method that does not use TCF regrasp.

Fig.5.15 shows the difference of the methods used for comparison. The first method is the conventional one which directly plans to move the picked object to the goal pose, as shown in Fig.5.15(a). The method is abbreviated as DPM in the following context. The second method is our proposed method, in which we build and search a regrasp graph to find a regrasp sequence. Especially, we propose two implementations of the method: Regrasp with All Grasps (RAG) and Regrasp with a Prescribed Grasp (RPG). In the RAG implementation, all the grasp configurations for the goal pose and SPP are considered to build the regrasp graph, as shown in Fig.5.15(b). The implementation exactly follows the graph shown in Fig. 5.9. In the RPG implementation, a goal SPP and a goal grasp configuration are prescribed manually, as shown in Fig.5.15(c). The motion between the prescribed goal SPP and the prescribed goal pose using the prescribed grasp configuration is taught instead of planned. From the viewpoint of Fig. 5.9, the connections in Fig. 5.9(c) and Fig. 5.9(d) are replaced with a given path. The regrasp sequence planner plans to (c) and uses the given path to reach (d). Both the RAG and RPG methods can take advantages of the TCF fixture to reduce the uncertainty of the yellow object poses. However, the RAG implementation's performance relies a lot on a robot's absolute precision. The robot action is online generated until the last step. In contrast, the RPG method leverages taught motion to move the object from the TCF to the final goal. Its performance is dominated by a robot's repeatability precision. We compare all the DPM, RAG, and RPG methods (or implementations) in the experiments. The holes of the insertion tasks in the experiments have different clearance, as shown in Fig. 5.16(a). The diameters of the holes range from 10.1 mm to 18.0 mm. The length and diameter of the peg are 75.0 mm and 10.0 mm, respectively. The clearance thus ranges from 0.1 mm to 8.0 mm. We run the insertion for each hole using one of the methods repeatedly by 15 times to obtain an average success rate, and get the methods' performance on eliminating uncertainty by considering the smallest clearance with 100% success rate.[2] In each repetition, we place the object in a random initial position on a table. A robot will detect it using a PhotoneoPhoXi 3D Scanner M depth sensor and move it to a pre-given goal pose with or without regrasp at the TCF. At the goal pose, the robot will insert the peg by moving a straight line with position control.

The results are shown in Fig. 5.16 as a bar chart, where the horizontal axis is the different hole diameters, and the vertical axis is the average success rate.

[2] A 100% average success rate means the method can always suppress the peg's uncertainty within a range indicated by the clearance value.

The results tell that the smallest clearance of the DPM, RAG, and RPG methods are 7.0 mm, 1.0 mm, and 0.1 mm, respectively. The methods share the same uncertainty origins, including visual recognition, fabrication, robotic control, etc., but they eliminate the uncertainty to different ranges. The RAG clearance is larger than RPG, which confirms that the robot has low absolute precision compared to repeatability precision.

5.5.3 Performance in Practical Real-World Tasks

Finally, we test the proposed method using four practical real-world assembly tasks: (1) Inserting the L-shape object into a rectangular groove; (2) Sheathing the T-junction with a tube; (3) Aligning the holes of the bracket and a base plate; (4) Mounting the bearing housing on a bracket. These tasks are frequently seen at industrial manufacturing sites.

Inserting the L-shape object

In this task, we fix an acrylic board with a rectangular groove on a table, and ask the robot to insert the L-shape object into the rectangular groove. Fig. 5.17(a.1) shows the sizes of the object and the groove. The clearance between them is 2.0 mm.

Sheathing the T-junction

The goal of this task is to sheathe a tube into the T-junction. The tube is vertically fixed on the table, and the robot is asked to manipulate the T-junction to perform

Table 5.1: Results of various methods in the practical tasks.

	Clearance	DPM	RAG	RPG
Insert L-shape	2.0 mm	2/10	10/10	10/10
Sheath T-junction	0.3 mm	0/10	0/10	10/10
Align holes	1.7 mm	0/10	10/10	10/10
Mount bearing housing	$<$0.1 mm	0/10	0/10	10/10

the sheathing action. Fig. 5.17(b.1) shows the sizes of the T-junction and tube. The maximum clearance between the inner circle of the T-junction and the outer circle of the tube is 0.3 mm.

Aligning the holes

In this task, a base plate with thread holes is fixed on a table. The two through-holes on the short side of the bracket are required to be aligned with the thread holes on the base plate. If a screw bolt can be fastened in the thread holes across the through-holes, we judge the alignment to be successful. Fig. 5.17(c.1) shows the sizes of the bracket and the thread holes. The difference between the inner thread-hole diameter and through-hole diameter is the task's clearance. Its value is 1.7 mm.

Mounting the bearing housing

This task requires the robot to mount the bearing housing on a fixed bracket. The sizes of the bearing housing and mounting hole are shown in Fig. 5.17(d.1). The clearance between them is less than 0.1 mm.

Like the previous experiments, the environment model, object models, and the configuration of the TCF are pre-given and pre-calibrated. Also, the goal poses of them in the assembly tasks are known. The initial poses of the objects are random. The conventional method (DPM) and the two implementations of our method (RAG and RPG) are tested. For each of the above tasks, we run ten times of experiments using different methods. Table 5.1 shows the experiment results. Using the DPM method, only two successful attempts were observed in inserting the L-shape object. All other tasks failed. Using the RAG method, all attempts to insert the L-shape object and align the holes succeeded, but no success was observed in the tasks of sheathing a T-junction and mounting a bearing housing. All tasks were successfully performed when the RPG method was used. The results show that the proposed method can provide reliable and robust performance for these tasks, especially when the RPG method is used.

Fig.5.17(a.2-d.2) shows execution pictures of some successful results in Table 5.1. Readers may also refer to the video supplementary attached to this manuscript to observe the detailed robotic actions.

5.6 Summary

This chapter presented a regrasp planning method to eliminate grasp uncertainty. The proposed method first computes all SPPs on a TCF, then estimates the DDP to find all DDP-SPP pairs, and finally generates the grasp configurations for releasing and regrasping the object. In particular, an analytical and a learning-based method are proposed for the DDP estimation. Experimental results verified that the learning-based method is more reliable than the analytical one. The regrasp sequence planned by the proposed method is demonstrated to reduce uncertainty to less than 0.1 mm using an RPG implementation, which is way more robust than a conventional regrasp sequence that does not take into account a TCF. Several real-world applications are also presented to show the proposed method's promising usage in assembly tasks.

Note that we ignored the influence of different materials in our work, and we assumed uniform density, fixed friction coefficient (0.3), and bounce rate (0.2). We also ignored the rotation around an object's symmetric axis (i.e., rotation of the bearing housing). It is thus impossible to stabilize this axis using the assumed TCF. In the future, we are interested in building a large deep neural network that generalizes to many common materials and developing flexible features and planners to consider more complicated object shapes.

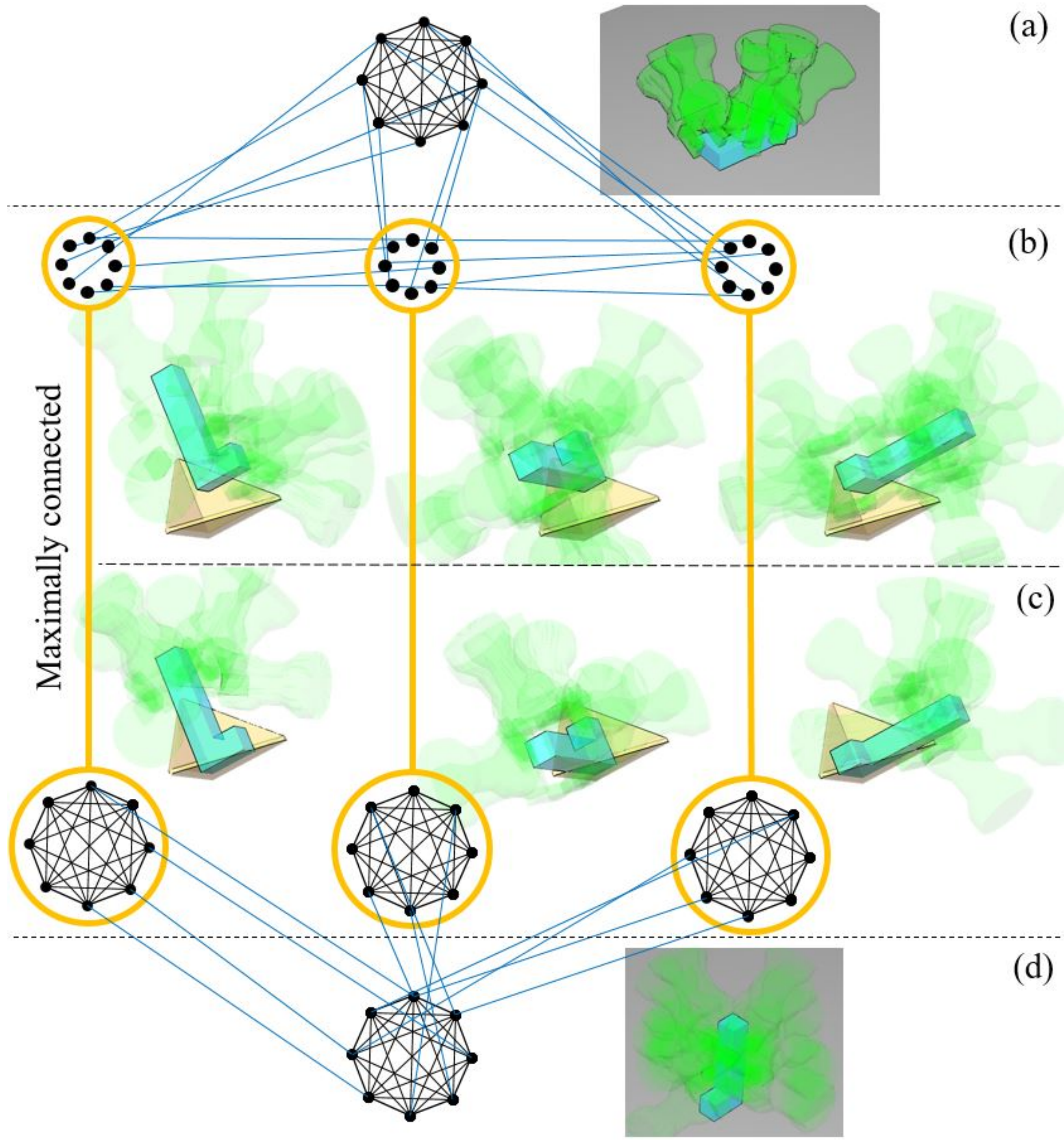

Figure 5.9: A regrasp graph. (a) Initial pose and its subgraph. (b) DDP and its subgraph. (c) SPP and its subgraph. (d) Goal pose and its subgraph. Each black node in the graph indicates one grasp pose. Each circle indicates an object pose. The nodes inside the circle are the grasp configurations associated with the corresponding pose. First, the nodes in (a), (b), (c), and (d) are connected separately to represent transit relations. Second, the shared grasp configurations between (a) and (b), and between (c) and (d) are connected for transfer relations. Third, the nodes in (b) and (c) are connected to represent transit relations between DDPs and SPPs.

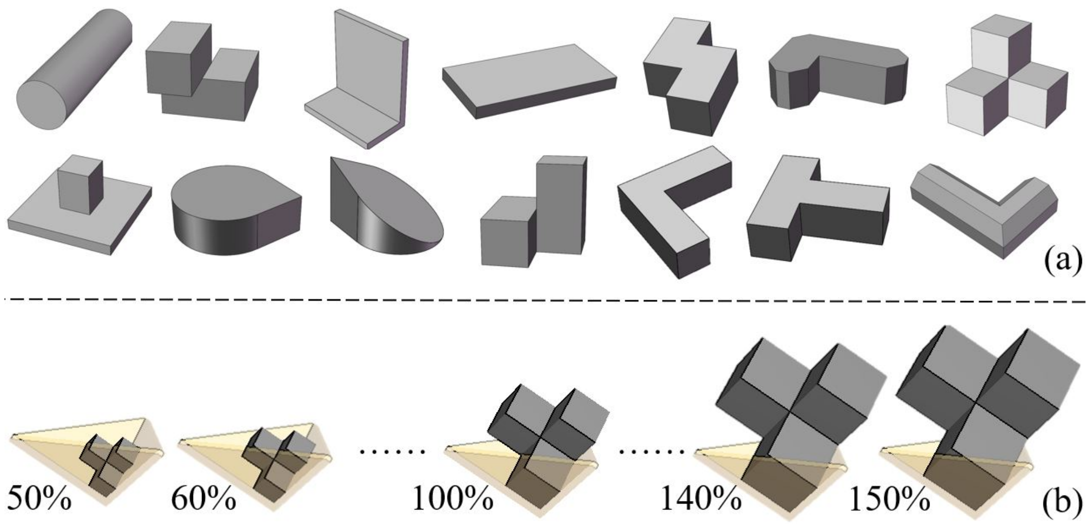

Figure 5.10: Objects used for obtaining the training data. By scaling the 14 primitive objects in (a) using the rules shown in (b) (resize the object from 50% to 150% at every 10%), in total 154 objects are prepared.

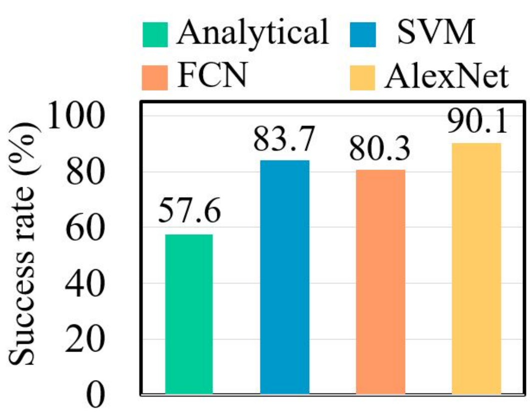

Figure 5.11: Comparison of the different estimation methods. The learning-based methods have higher estimation success rate. Especially, the AlexNet method is the most effective one.

	L-shape object			T-junction			Bracket			Bearing housing		
Method	Unpaired	DDP-SPP	Total(%)	Unpaired	DDP-SPP	Total(%)	Unpaired	DDP-SPP	Total(%)	Unpaired	DDP-SPP	Total(%)
Analytical	48/48	6/6	100	0/48	0/24	0	42/42	12/12	100	72/72	6/72	54
SVM	48/48	6/6	100	38/48	14/24	72	33/42	12/12	83	72/72	45/72	81
FCN	48/48	6/6	100	37/48	14/24	71	32/42	9/12	76	72/72	50/72	85
AlexNet	48/48	6/6	100	41/48	18/24	82	38/42	10/12	89	72/72	60/72	92

Figure 5.12: The Unpaired and DDP-SPP columns are presented in a fraction style. The denominator values indicate the ground truth obtained using repeated physical simulation. The numerator values indicate the estimated results.

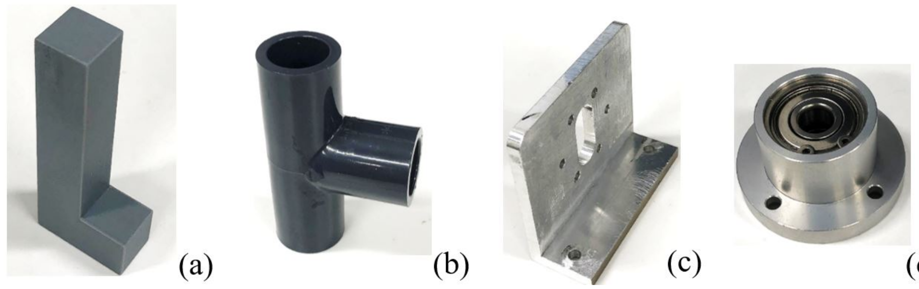

Figure 5.13: The objects used for testing the planner. (a) L-shape object. (b) T-junction. (c) Bracket. (d) Bearing housing.

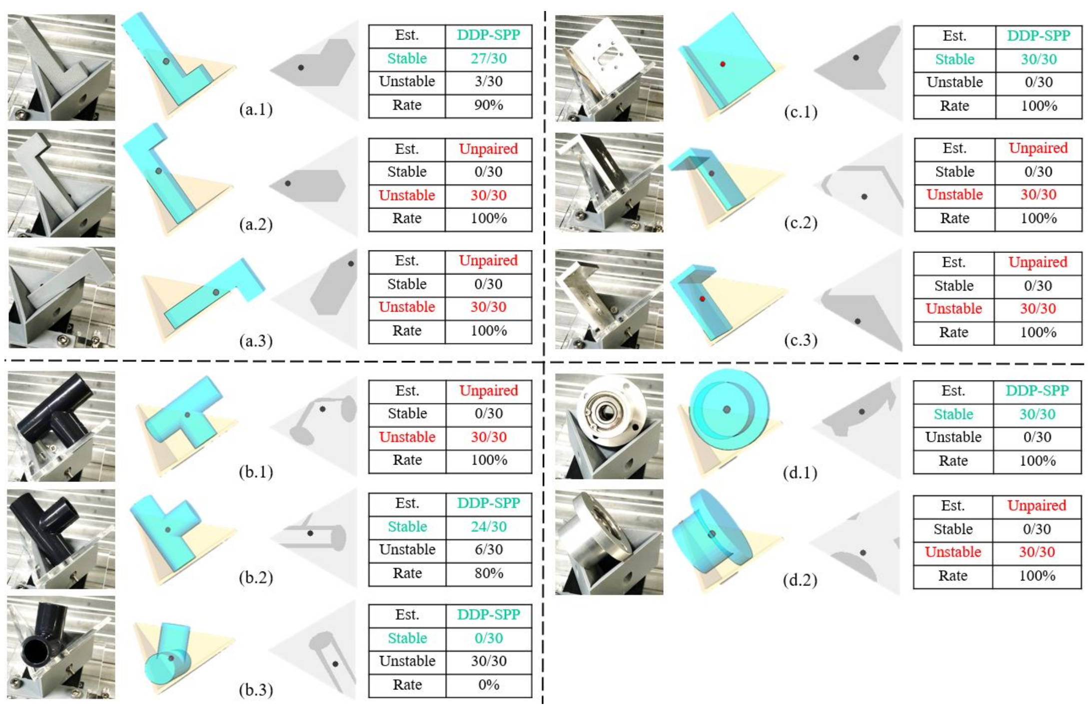

Figure 5.14: The results of testing the estimator using different objects. (a) L-shape object. (b) T-junction. (c) bracket. (d) bearing housing. The SPPs of each object are selectively shown. The left column shows the real-world photos, the middle column shows the placements in the simulator, and the right column illustrates the projected images.

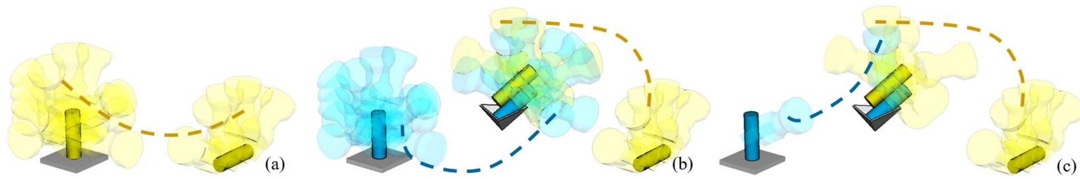

Figure 5.15: Illustrations of the task process using different methods. The initial pose, the intermediate DDP, and their associated grasps are illustrated in a yellow color. The intermediate SPP, the goal pose, and their associated grasp poses are illustrated in a cyan color. (a) DPM: Directly plan to move the object to the goal pose. (b) RAG: An implementation of the proposed method that plans regrasp using all grasp configurations for the goal pose and the regrasp. (c) RPG: Another implementation that plans regrasp using a prescribed grasp configuration for the goal pose and the regrasp. The cyan object poses and grasp configurations (a single one for each object pose) indicate the prescribed items.

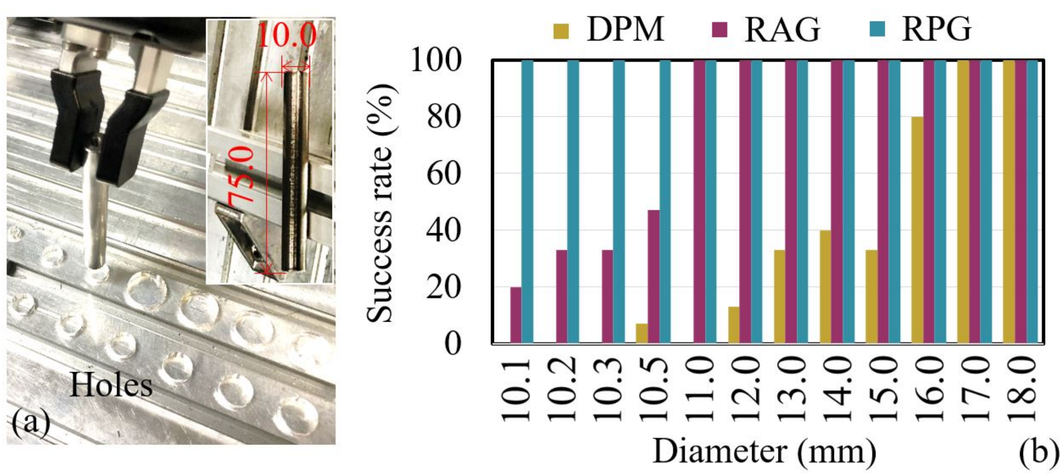

Figure 5.16: The success rates (%) of inserting a peg into holes with different diameters using different methods.

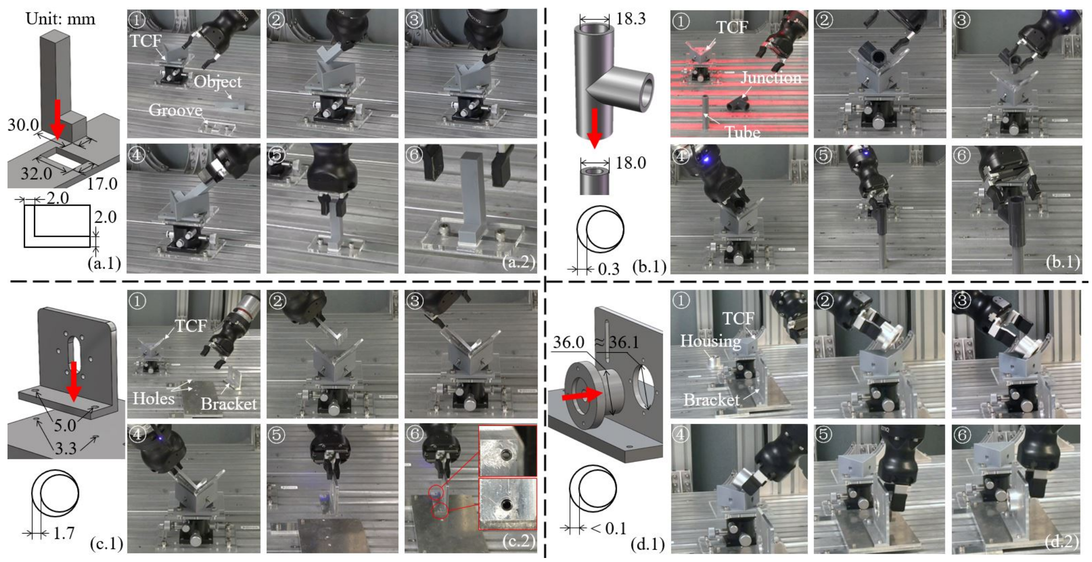

Figure 5.17: (a) Inserting the L-shape object. (b) Sheathing the T-junction. (c) Aligning the holes. (d) Mounting the bearing housing. The left column shows the main boundary dimensions of the components and also points the assembly direction. The right column shows the demonstration of the successful task.

Chapter 6

Conclusions and Future Work

6.1 Conclusions of the Contents

This thesis proposes the methods of designing mechanical tools for the robots with two-finger parallel grippers. Three tools are presented, respectively. They are the clamping tool, the rotating tools, and a peripheral tool, TCF. The clamping tool converts the parallel motion of the gripper into the parallel motion on the tooltips. By using different tools with different tooltips, the general parallel grasp can also adapt to various objects. The Rotating tools converts the parallel motion of the gripper into the continuous rotating motion on the tooltip for screwing tasks. Additionally, the TCF can be used as a regrasp intermedia to eliminate the grasp uncertainty as well as orient the object. It's not only used for the manipulation of objects, but also can be used to orient the proposed mechanical tools, and reduce the errors on tool use.

This thesis consists of six chapters. Besides of the sixth chapter, the conclusions of the other five chapters are as following.

Chapter one is the introduction. We investigate the current challenges in modern manufacturing, and especially discuss the difficulties in the robotic assembly and robotic manipulation. We therefore focus on an urgent problem in industry, adaptive assembly tasks using robots. This chapter also introduces the conventional methods for extending the functions of robots by the developments on robotic hands and hand changers, and the concept of manipulation using tools. On the basis of this background, we present the core proposal of this thesis, designing mechanical tools to extend the functions of general grippers to promote the flexible robotic assembly work.

Three topics are analyzed in this chapter: mechanism design, robot operation with tools, and uncertainty removal operation. The part about mechanism design focuses on the design of end-effector with high-performance, especially those that facilitate force transformation and motion convention. By reviewing the robotic operation of the tool usage, we summarize how to plan the use of tools with better reasoning. After that, we study sensor-less manipulation and placement estimation methods that can eliminate uncertainty. Finally, by comparing our method with previous studies, we stress on the novelties of the former and thus prove the significance of this method.

Chapter three elaborates the design of clamping tools. We presents the fundamental kinematic structure of the mechanical tool, which use two symmetric parallelograms to transmit the motion of the robotic gripper to the tooltips. Four torsion springs are attached to the four inner joints of the two parallelograms to reopen the tool as the robotic gripper releases. The forces and transmission are analyzed in detail to make sure the tool reacts well with respect to the gripping forces and the spring stiffness. Based on the kinematic structure, various tooltips were designed for the mechanical tool to perform different tasks. The designed tool could be treated as a normal object and be picked up and used by automatically planned grasps. A robot may locate the tool through the AR markers attached to the tool body, grasp the tool by selecting an automatically planned grasp, and move the tool from any arbitrary pose to a specific pose to perform various tasks. The robot may also determine the optimal grasps and usage according to the requirements of given tasks.

Chapter four details the design, optimization, and manipulation policies of the rotating tools. This mechanical design is based on a combined Scissor-Like Element (SLE) and double-ratchet mechanism that converts the gripping motion of 2-finger parallel grippers into a continuous rotation to realize tasks like fastening screws. This chapters presents the tool design, optimizes the tool's dimensions and effective stroke lengths, and studies the contacts and forces to achieve stable grasping and screwing. It also shows the related manipulation and control policies, including recognizing the tool, changing tool poses, and completing screw fastening tasks. The designed tool, together with the related manipulation and control policies, are analyzed and verified in several real-world applications. Robots with parallel grippers can robustly and flexibly use the tool to fasten screws. The tool can also be used collaboratively with other tools to finish difficult tasks.

Chapter five presents the method of eliminating uncertainty based on the regrasp using the TCF as an intermedia. We develop the algorithms that plan releasing and regrasp sequences using a triangular corner fixture, and thus reduces the grasp uncertainty. With the help of the algorithms and the fixture, a robot can perform online pick-up and at the same time conduct precise assembly. There is no need for complicated vision recognition or force control. The proposed method can improve grasp precision and also reduce the grasp errors on manipulation the proposed mechanical tools.

6.2 Discussion

6.2.1 Advantages

Fast integration

Traditional robot integration relies heavily on the setup of peripheral devices. Arranging and positioning the devices to need the effort of experienced engineers. They determine types of robotic hands, types of tool changers, and other associated devices like compressors, miscellaneous connectors, and cables. Besides, they also perform teaching and programming tasks to make the industry robots move while carefully considering collisions with the surrounding environment and other parts of the robots. The cost of system integration is not cheap. In comparison, the designed tool is closely connected to intelligence. It is inherently designed for autonomous tasks and motion planning. The proposed tool can be placed in an arbitrary position, and the robot recognizes the tool and plans to use it. Therefore, these tools help to fast integrate the robot system.

The tools are purely mechanical, the cost is extremely low compared with the functional robot hands and hand changers with control modules and power systems. For various tasks, preparing suitable tools for the robots is easier and cheaper than configuring multiple tools and hand changers.

Collision-free motion planning

Robots may also use electric tools or pneumatic tools for the same goals as our tools. But to power and control the powered tools, the tailed cables or tubes are non-negligible. These cables are deformable with varying elasticity, so it's hard to plan the collision-free motion trajectories. The cables may tangle robots or environmental objects, and even drag robots until protective stop. The proposed tools are powered and controlled by grippers. No external power supply and control signal. Thus, using the tools is planning of moving rigid bodies.

Torque control

The robots are usually equipped with F/T sensors on their wrists. The sensors can be used to monitor the torque output of the rotating tool. The electric tools with cables are feasible to communicate with the robot system to accurately control the output. But the disadvantage of motion planning is a fatal defect. Cordless tools help to get rid of the impact from cables. But robots are hard to control the switch of tools as smoothly as a human. Using wireless control is a possible way to control cordless tools. However, cordless electric tools are rarely equipped with torque sensors that can accurately control the output torque, and real-time communication for controlling the output torque is also difficult.

Extra degree of freedom for flexible motion

Robots can plan different grasp poses to use the tool. The tool provides extra degrees of freedom for manipulation. Thus, the reachable range of robots is extended with the tools. This feature solves the problem that no IK solution for task requirements.

6.2.2 Limitation

The tools extend the flexibility, meanwhile, the stability and accuracy are decreased. The tool is fixed by gripping, which is less stable and accurate than the connection of the hand changer. Besides, the tool is hard to be calibrated if the fabrication accuracy is not satisfying. Instead of accurate calibration, we proposed to use compliant control to offset, and use the adaptive tooltips to tolerate the uncertainty.

The efficiency of the tool is a weakness, especially the screwing speed of the rotating tool. We proposed to use the assistant gearbox tool to accelerate the rotation, but it costs too much to involve another gripper, and the flexibility also decreases, which deviates from our original intention. It's potential to add the miniaturized gear hat on the ratchets to accelerate, and also reduce the speed to obtain high output torque

We would like to further the application of the proposed tools. Currently, the tools are only practical for the assembly work in laboratory scenes. As industrial robots and devices have strict standards, our prototypes are far away from these. But our tools provide the possible solutions for solving the urgent problems in fast integration, collision-free motion planning, output torque control, and increasing flexibility.

The object alignment, in our method, is based on the physical constraints between the outer profile of the object and the TCF, but the inner features of the object make no sense to the analysis except the position of CoM. If the final task only concerns the features of the outer profile of the object, our method can provide reliable results. However, if the final task focuses on the fits of the inner features of the objects, our method fails to provide feasible results. Take the task of mounting a bearing housing, as an example, the robot can insert the cylinder part into the hole on the bracket, but the four small holes on the flange have no way to be aligned. Thus, the manipulation methods using visual feedback are needed to adjust the rotation to align them.

6.3 Future work

In the long-term vision, we propose to promote the standardization of robots. In the future, robots are expected to be hired like human workers, instead of just being integrated into factory automation systems like machines. Nowadays, to fast meet the short-term profit, many customized robots and grippers were proposed. They only work well in the limited range, and the nonstandard systems make the system integration very complicated. With the standardization of robots, we can fast integrate the system and reuse the general knowledge and skills.

Along with the proposed concept, we would like to design more tools to further expand the tool lineup for standard robots. Not only limited by the clamping motion and rotation, but it's also possible to use tools to transmit the simple gripper motion into more skillful motions. Additionally, the tool is specially designed for 2-finger parallel grippers in their current state. This limits the application. We start by designing for 2 fingers as it is simpler to deduce the formulae and analyze the contacts for two same finger pads. We would like to consider the tool use method for other grippers

For the short-term targets, we should increase the stability of holding the tool, and increase the efficiency of output. This part relies on a novel mechanism design. Besides, to make it more practical, increasing the accuracy of fabrication and assembly is in urgent need. For aligning the object, we would like to extend this idea for the objects with various shapes instead of the ones with triplets of orthogonal contact surfaces.

ACKNOWLEDGMENTS

This thesis would not come into being if I had not received help from my supervisor, teachers, classmates, and family. Foremost, I would like to express my sincere gratitude to my supervisor Prof. Harada Kensuke for the continued support of my Ph.D. study and research for his patience, motivation, enthusiasm, and immense knowledge. He offered me a free and inclusive space for my study and life. His guidance helped me in all the time of research and writing of this thesis. I could not have imagined having a better advisor and mentor for my Ph.D. study.

Besides my supervisor, I would like to appreciate Prof. Wan Weiwei. He cultivated my basic ability of scientific research. and he helped me to make step-by-step progress and to shape the world of academic research.

I would like to also thank the rest of my thesis committee: Prof. Ishiguro Hiroshi and Prof. Hosoda Koh for their encouragement, insightful comments, and hard questions.

I especially thank my lab mates, Mr. Chen Hao, Ms. Liu Ruishuang, for the endless academic discussion, for the sleepless nights we were working together before deadlines, and for all the fun we have had in the last three years. Here is also a special thank to my labmate and also my roommate, Mr. Zhang Qi. From undergraduate to doctor, we fight shoulder to shoulder, I thank for his accompany. Also, all my lab mates helped me a lot in both life and study, Mr. Zhang Ang, Mr. Xu Jingren, Ms. Zhang Xinyi, Ms. Wang Zhengting, Ms. Gao Yuan, Mr.Cristian Beltran, Mr. Higashi Kazuki, Mr. Matsuosa Shogo, Mr. Kobayashi Sho, Mr. Hayakawa Shogo, and Mr. Tsuru Masato. I sincerely thank their help.

While, I will never forget to thank the graduated students from our lab, Mr. Nie Kaidi, Mr. He Qiming, Mr. Daniel, Mr. Nakayama Kento, Mr. Wang Yan, and Mr. Joshua for guiding me to this lab at that time, and taking care of me when I was a rookie.

Last but not the least, I would like to thank my parents for giving birth to me in the first place and supporting me spiritually throughout my life. Their encouragement when the times got rough is much appreciated and duly noted. My heartfelt thanks.

It wasn't until I finished writing my doctor dissertation that I slowly figured out how to start an excellent doctoral project. With the in-depth research, I gradually realized my shortcomings. As told by my thesis examiners, Prof. Ishiguro and Prof. Hosoda, a doctorate is just an entry pass for you to embark on an academic path. Getting a doctorate is not a triumphant song, but a clarion call for a new journey.

BIBLIOGRAPHY

[1] HK Shivanand. *Flexible manufacturing system*. New Age International, 2006.

[2] John H Blackstone, Don T Phillips, and Gary L Hogg. A state-of-the-art survey of dispatching rules for manufacturing job shop operations. *The International Journal of Production Research*, 20(1):27–45, 1982.

[3] Steven Y Liang, Rogelio L Hecker, and Robert G Landers. Machining process monitoring and control: the state-of-the-art. *J. Manuf. Sci. Eng.*, 126(2):297–310, 2004.

[4] CA Van Luttervelt and J Peng. Symbiosis of modelling and sensing to improve the accuracy of workpieces in small batch machining operations. *The International Journal of Advanced Manufacturing Technology*, 15(10):699–710, 1999.

[5] Urban Wemmerlöv and Nancy L Hyer. Cellular manufacturing in the us industry: a survey of users. *The international journal of production research*, 27(9):1511–1530, 1989.

[6] Taeyong Choi, Hyunmin Do, Chanhun Park, Kwangcho Chung, Dongil Park, and Jinho Kyung. Advanced manufacturing with robot. In *2012 12th International Conference on Control, Automation and Systems*, pages 2207–2209. IEEE, 2012.

[7] MH Korayem, N Shiehbeiki, and T Khanali. Design, manufacturing, and experimental tests of a prismatic robot for assembly line. *The International Journal of Advanced Manufacturing Technology*, 29(3):379–388, 2006.

[8] Baek-Suk Chu, Dong-Nam Kim, and Dae-Hie Hong. Robotic automation technologies in construction: A review. *International Journal of Precision Engineering and Manufacturing*, 9(3):85–91, 2008.

[9] Sandra Robla-Gómez, Victor M Becerra, José Ramón Llata, Esther Gonzalez-Sarabia, Carlos Torre-Ferrero, and Juan Perez-Oria. Working together: A review on safe human-robot collaboration in industrial environments. *IEEE Access*, 5:26754–26773, 2017.

[10] Matthew T Mason. *Mechanics of robotic manipulation*. MIT press, 2001.

[11] Matthew T Mason. Toward robotic manipulation. *Annual Review of Control, Robotics, and Autonomous Systems*, 1:1–28, 2018.

[12] Ray A Jarvis. A laser time-of-flight range scanner for robotic vision. *IEEE Transactions on pattern analysis and machine intelligence*, (5):505–512, 1983.

[13] Qi She, Fan Feng, Xinyue Hao, Qihan Yang, Chuanlin Lan, Vincenzo Lomonaco, Xuesong Shi, Zhengwei Wang, Yao Guo, Yimin Zhang, et al. Openloris-object: A robotic vision dataset and benchmark for lifelong deep learning. In *2020 IEEE international conference on robotics and automation (ICRA)*, pages 4767–4773. IEEE, 2020.

[14] Wei Chen, Heba Khamis, Ingvars Birznieks, Nathan F Lepora, and Stephen J Redmond. Tactile sensors for friction estimation and incipient slip detection—toward dexterous robotic manipulation: A review. *IEEE Sensors Journal*, 18(22):9049–9064, 2018.

[15] YF Li and XB Chen. On the dynamic behavior of a force/torque sensor for robots. *IEEE Transactions on Instrumentation and Measurement*, 47(1):304–308, 1998.

[16] Daolin Ma and Caishan Liu. Contact law and coefficient of restitution in elastoplastic spheres. *Journal of Applied Mechanics*, 82(12):121006, 2015.

[17] Wenzhen Yuan, Siyuan Dong, and Edward H Adelson. Gelsight: High-resolution robot tactile sensors for estimating geometry and force. *Sensors*, 17(12):2762, 2017.

[18] S Reza Kashef, Samane Amini, and Alireza Akbarzadeh. Robotic hand: A review on linkage-driven finger mechanisms of prosthetic hands and evaluation of the performance criteria. *Mechanism and Machine Theory*, 145:103677, 2020.

[19] Fan Yu Chen. Gripping mechanisms for industrial robots: an overview. *Mechanism and Machine Theory*, 17(5):299–311, 1982.

[20] Thierry Laliberte, Lionel Birglen, and Clément Gosselin. Underactuation in robotic grasping hands. *Machine Intelligence & Robotic Control*, 4(3):1–11, 2002.

[21] Yasuhisa Hirata, Aya Kaisumi, Kengo Yamaguchi, and Kazuhiro Kosuge. Design of handling device for caging and aligning circular objects. In *2011*

IEEE International Conference on Robotics and Automation, pages 4370–4377. IEEE, 2011.

[22] Chih-Hsing Liu, Ta-Lun Chen, Chen-Hua Chiu, Mao-Cheng Hsu, Yang Chen, Tzu-Yang Pai, Wei-Geng Peng, and Yen-Pin Chiang. Optimal design of a soft robotic gripper for grasping unknown objects. *Soft robotics*, 5(4):452–465, 2018.

[23] Kensuke Harada, Kazuyuki Nagata, Juan Rojas, Ixchel G Ramirez-Alpizar, Weiwei Wan, Hiromu Onda, and Tokuo Tsuji. Proposal of a shape adaptive gripper for robotic assembly tasks. *Advanced Robotics*, 30(17-18):1186–1198, 2016.

[24] Joshua C Triyonoputro, Weiwei Wan, and Kensuke Harada. A double jaw hand designed for multi-object assembly. In *2018 IEEE-RAS 18th International Conference on Humanoid Robots (Humanoids)*, pages 427–430. IEEE, 2018.

[25] Kaidi Nie, Weiwei Wan, and Kensuke Harada. A hand combining two simple grippers to pick up and arrange objects for assembly. *IEEE Robotics and Automation Letters*, 4(2):958–965, 2019.

[26] C Piazza, G Grioli, MG Catalano, and AJAROC Bicchi. A century of robotic hands. *Annual Review of Control, Robotics, and Autonomous Systems*, 2:1–32, 2019.

[27] Design of an automatic tool changer with disc magazine for a cnc horizontal machining center. *International Journal of Machine Tools and Manufacture*, 37(3):277–286, 1997.

[28] Kent Lundberg. Automatic tool changer [25 years ago]. *IEEE Control Systems Magazine*, 31(6):18–18, 2011.

[29] Jayson P. Rogelio and Renann G. Baldovino. Development of an automatic tool changer (atc) system for the 3-axis computer numerically-controlled (cnc) router machine: Support program for the productivity and competitiveness of the metals and engineering industries. In *2014 International Conference on Humanoid, Nanotechnology, Information Technology, Communication and Control, Environment and Management (HNICEM)*, pages 1–5, 2014.

[30] Tools for the body (schema). *Trends in Cognitive Sciences*, 8(2):79–86, 2004.

[31] Animal tool-use. *Current Biology*, 20(23):R1032–R1039, 2010.

[32] Tool use and physical cognition in birds and mammals. *Current Opinion in Neurobiology*, 19(1):27–33, 2009. Cognitive neuroscience.

[33] J Cuadrado, MA Naya, M Ceccarelli, and G Carbone. An optimum design procedure for two-finger grippers: a case of study. *IFToMM Electronic Journal of Computational Kinematics*, 15403(1):2002, 2002.

[34] Weiwei Wan, Koyama Keisuke, and Harada Kensuke. Generation of robotic task motion - motion planning and its related technologies. *Journal of the Robotics Society of Japan*, 38(6):511–515, 2020.

[35] Daniel Sánchez, Weiwei Wan, and Kensuke Harada. Tethered tool manipulation planning with cable maneuvering. *IEEE Robotics and Automation Letters*, 5(2):2777–2784, 2020.

[36] Daniel Sanchez, Weiwei Wan, and Kensuke Harada. Four-arm collaboration: Two dual-arm robots work together to manipulate tethered tools. *IEEE/ASME Transactions on Mechatronics*, pages 1–11, 2021.

[37] Gareth J Monkman, Stefan Hesse, Ralf Steinmann, and Henrik Schunk. *Robot grippers*. John Wiley & Sons, 2007.

[38] Andreas Wolf and Henrik A Schunk. *Grippers in motion: the fascination of automated handling tasks*. Carl Hanser Verlag GmbH Co KG, 2018.

[39] Alaa Hassan and Mouhammad Abomoharam. Design of a single dof gripper based on four-bar and slider-crank mechanism for educational purposes. *Procedia CIRP*, 21:379–384, 2014.

[40] Hikmet Kocabas. Gripper design with spherical parallelogram mechanism. *Journal of Mechanical Design*, 131(7):075001, 2009.

[41] Lionel Birglen, Thierry Laliberté, and Clément M Gosselin. *Underactuated robotic hands*. Springer, 2007.

[42] Raymond R Ma, Adam Spiers, and Aaron M Dollar. M 2 gripper: Extending the dexterity of a simple, underactuated gripper. In *Advances in Reconfigurable Mechanisms and Robots II*, pages 795–805. 2016.

[43] Wenrui Chen, Caihua Xiong, Wenbin Chen, and Shigang Yue. Mechanical adaptability analysis of underactuated mechanisms. *Robotics and Computer-Integrated Manufacturing*, 49:436–447, 2018.

[44] K. Harada, T. Tsuji, S. Uto, N. Yamanobe, K. Nagata, and K. Kitagaki. Stability of soft-finger grasp under gravity. In *Proceedings of IEEE International Conference on Robotics and Automation*, pages 883–888, 2014.

[45] William Zuk and Roger H Clark. *Kinetic architecture*. 1970.

[46] Qais Khasawneh, Mohammad A Jaradat, and Ahmad Alshorman. Enhanced design of microgripper using double actuators of shape memory alloy wires. In *Proceedings of ASME Dynamic Systems and Control Conference*, 2014.

[47] Feray Maden, Koray Korkmaz, and Yenal Akgün. A review of planar scissor structural mechanisms: geometric principles and design methods. *Architectural Science Review*, 54(3):246–257, 2011.

[48] Yi Yang, Yaping Tian, Yan Peng, and Huayan Pu. A novel 2-dof planar translational mechanism composed by scissor-like elements. *Mechanical Sciences*, 8(1):179–193, 2017.

[49] David Corinaldi, Massimo Callegari, Matteo-Claudio Palpacelli, and Giacomo Palmieri. Synthesis of a spatial 3-dof deployable mechanism to grasp stacked non-rigid materials. In *Advances in Reconfigurable Mechanisms and Robots II*, pages 1095–1106. 2016.

[50] Yosri Taha Sanaani, Ahmad Alshorman, and Khaled Alshurman. A novel design of flexure based, shape memory alloy actuated microgripper. In *ASME International Mechanical Engineering Congress and Exposition*, volume 58370, page V04AT05A023, 2017.

[51] Hossein Mehrabi, Mohsen Hamedi, and Iman Aminzahed. A novel design and fabrication of a micro-gripper for manipulation of micro-scale parts actuated by a bending piezoelectric. *Microsystem Technologies*, 26(5):1563–1571, 2020.

[52] Jianjun Yuan, Weiwei Wan, Kaiwei Chen, Qi Fang, and Weijun Zhang. Design and prototyping a cable-driven multi-stage telescopic arm for mobile surveillance robots. In *2014 IEEE International Conference on Robotics and Biomimetics (ROBIO 2014)*, pages 1845–1850, 2014.

[53] Tomoaki Mashimo, Rosen Diankov, Takateru Urakubo, and Takeo Kanade. Analysis of task feasibility for a home robot using prismatic joints. In *2010 IEEE/RSJ International Conference on Intelligent Robots and Systems*, pages 2370–2376, 2010.

[54] Mahdi Bamdad and Arman Mardani. Design and analysis of a novel tendon-less backbone robot. *International Journal of Robotics, Theory and Applications*, 4(3):55–65, 2015.

[55] Yudong Luo, Na Zhao, Yantao Shen, and Kwang J Kim. Scissor mechanisms enabled compliant modular earthworm-like robot: Segmental muscle-mimetic design, prototyping and locomotion performance validation. In *Proceedings of IEEE International Conference on Robotics and Biomimetics*, pages 2020–2025, 2016.

[56] Isaac Ndawula and Samy FM Assal. Conceptual design and kinematic analysis of a novel open field 3dof multi-gripper pot seedlings transplanting robot. In *Proceedings of IEEE International Conference on Mechatronics and Automation*, pages 1458–1463, 2018.

[57] Miguel Nobre Castro, John Rasmussen, Michael Skipper Andersen, and Shaoping Bai. A compact 3-dof shoulder mechanism constructed with scissors linkages for exoskeleton applications. *Mechanism and Machine Theory*, 132:264–278, 2019.

[58] Jing-Shan Zhao, Jian-Yi Wang, Fulei Chu, Zhi-Jing Feng, and Jian S Dai. Structure synthesis and statics analysis of a foldable stair. *Mechanism and Machine Theory*, 46(7):998–1015, 2011.

[59] Yenal Akgün, Charis J Gantes, Werner Sobek, Koray Korkmaz, and Konstantinos Kalochairetis. A novel adaptive spatial scissor-hinge structural mechanism for convertible roofs. *Engineering Structures*, 33(4):1365–1376, 2011.

[60] Yuantao Sun, Sanmin Wang, James K Mills, and Changjian Zhi. Kinematics and dynamics of deployable structures with scissor-like-elements based on screw theory. *Chinese Journal of Mechanical Engineering*, 27(4):655–662, 2014.

[61] Sanmin Wang, Changjian Zhi, Bo Li, et al. A new flexible multibody dynamics analysis methodology of deployable structures with scissor-like elements. *Chinese Journal of Mechanical Engineering*, 32(1):1–10, 2019.

[62] Bo Li, San-Min Wang, Viliam Makis, and Xiang-Zhen Xue. Dynamic characteristics of planar linear array deployable structure based on scissor-like element with differently located revolute clearance joints. *Proceedings of the Institution of Mechanical Engineers, Part C: Journal of Mechanical Engineering Science*, 232(10):1759–1777, 2018.

[63] A Padma Rao, A Kiran Kumar, and S Suresh. Power generation from speed breaker by rack and ratchet mechanism. *International Journal of Current Engineering and Technology*, (2), 2014.

[64] Dzung Viet Dao, Phuc Hong Pham, Satoshi Amaya, and Susumu Sugiyama. Micro ratcheting transmission systems based on electrostatic actuator. In *Proceedings of International Symposium on Micro-NanoMechatronics and Human Science*, pages 17–20, 2008.

[65] Michiel Plooij, Glenn Mathijssen, Pierre Cherelle, Dirk Lefeber, and Bram Vanderborght. Lock your robot: A review of locking devices in robotics. *IEEE Robotics & Automation Magazine*, 22(1):106–117, 2015.

[66] Bing Li, Qiang Deng, and Zhichao Liu. A spherical hopping robot for exploration in complex environments. In *Proceedings of IEEE International Conference on Robotics and Biomimetics*, pages 402–407, 2009.

[67] Joost Geeroms, Louis Flynn, Rene Jimenez-Fabian, Bram Vanderborght, and Dirk Lefeber. Ankle-knee prosthesis with powered ankle and energy transfer for cyberlegs α-prototype. In *Proceedings of IEEE International Conference on Rehabilitation Robotics*, pages 1–6, 2013.

[68] T Abe, H Nakaji, and R Nakamura. Development of the bending mechanism for forceps with least-incision transformable end-effector mechanism for endoscopic surgery: Development of the operating interface and in vivo experiment. In *Proceedings of IEEE-RAS/EMBS International Conference on Biomedical Robotics and Biomechatronics*, pages 919–923, 2012.

[69] Lucas Gerez and Minas Liarokapis. A compact ratchet clutch mechanism for fine tendon termination and adjustment. In *Proceedings of IEEE/ASME International Conference on Advanced Intelligent Mechatronics*, pages 1390–1395, 2018.

[70] Pouya Sabetian, Amir Feizollahi, Farzad Cheraghpour, and S Ali A Moosavian. A compound robotic hand with two under-actuated fingers and a continuous finger. In *Proceedings of IEEE International Symposium on Safety, Security, and Rescue Robotics*, pages 238–244, 2011.

[71] YC Hao, WZ Yuan, HM Zhang, and HL Chang. A microgripper with a ratchet self-locking mechanism. In *Proeedings of IEEE International Conference on Micro Electro Mechanical Systems*, pages 1106–1109, 2015.

[72] Z. Hu, W. Wan, and K. Harada. Designing a mechanical tool for robots with two-finger parallel grippers. *IEEE Robotics and Automation Letters*, 4(3):2981–2988, 2019.

[73] Marc Toussaint, Kelsey Allen, Kevin A Smith, and Joshua B Tenenbaum. Differentiable physics and stable modes for tool-use and manipulation planning. In *Robotics: Science and Systems*, 2018.

[74] Solly Brown and Claude Sammut. A relational approach to tool-use learning in robots. In *International Conference on Inductive Logic Programming*, pages 1–15. Springer, 2012.

[75] Hao Chen, Weiwei Wan, and Kensuke Harada. Combined task and motion planning for a dual-arm robot to use a suction cup tool. In *Proceedings of IEEE-RAS International Conference on Humanoid Robots*, pages 446–452, 2019.

[76] SK Gupta, Christiaan JJ Paredis, and PF Brown. Micro planning for mechanical assembly operations. In *Proceedings of IEEE International Conference on Robotics and Automation*, volume 1, pages 239–246, 1998.

[77] Vadim Tikhanoff, Ugo Pattacini, Lorenzo Natale, and Giorgio Metta. Exploring affordances and tool use on the icub. In *Proceedings of IEEE-RAS International Conference on Humanoid Robots*, pages 130–137, 2013.

[78] Namiko Saito, Kitae Kim, Shingo Murata, Tetsuya Ogata, and Shigeki Sugano. Detecting features of tools, objects, and actions from effects in a robot using deep learning. In *Proceedings of Joint IEEE International Conference on Development and Learning and Epigenetic Robotics*, pages 1–6, 2018.

[79] Kuan Fang, Yuke Zhu, Animesh Garg, Andrey Kurenkov, Viraj Mehta, Li Fei-Fei, and Silvio Savarese. Learning task-oriented grasping for tool manipulation from simulated self-supervision. *The International Journal of Robotics Research*, 39(2-3):202–216, 2020.

[80] Namiko Saito, Kitae Kim, Shingo Murata, Tetsuya Ogata, and Shigeki Sugano. Tool-use model considering tool selection by a robot using deep learning. In *Proceedings of IEEE-RAS International Conference on Humanoid Robots*, pages 270–276, 2018.

[81] Zexiang Li and S Shankar Sastry. Task-oriented optimal grasping by multifingered robot hands. *IEEE Journal on Robotics and Automation*, 4(1):32–44, 1988.

[82] Aravind Rajeswaran, Vikash Kumar, Abhishek Gupta, Giulia Vezzani, John Schulman, Emanuel Todorov, and Sergey Levine. Learning complex dexterous manipulation with deep reinforcement learning and demonstrations. In *Proceedings of Robotics: Science and Systems*, Pittsburgh, Pennsylvania, June 2018.

[83] Yixin Zhu, Yibiao Zhao, and Song Chun Zhu. Understanding tools: Task-oriented object modeling, learning and recognition. In *Proceedings of the IEEE Conference on Computer Vision and Pattern Recognition*, pages 2855–2864, 2015.

[84] Mohamed Raessa, Daniel Enrique Sanchez Aranguren, Weiwei Wan, and Kensuke Harada. Teaching a robot to use electric tools with regrasp planning. *CAAI Transactions on Intelligence Technology*, 4:54–63, 2019.

[85] Annie Xie, Frederik Ebert, Sergey Levine, and Chelsea Finn. Improvisation through physical understanding: Using novel objects as tools with visual foresight. *arXiv preprint arXiv:1904.05538*, 2019.

[86] Rachel Holladay, Tomás Lozano-Pérez, and Alberto Rodriguez. Force-and-motion constrained planning for tool use. In *Proceedings of IEEE/RSJ International Conference on Intelligent Robots and Systems*, 2019.

[87] Zhenzhong Jia, Ankit Bhatia, Reuben M Aronson, David Bourne, and Matthew T Mason. A survey of automated threaded fastening. *IEEE Transactions on Automation Science and Engineering*, 16(1):298–310, 2018.

[88] Edward J Nicolson and Ronald S Fearing. Compliant control of threaded fastener insertion. In *Proceedings IEEE International Conference on Robotics and Automation*, pages 484–490, 1993.

[89] Liming Tan, Cheng Sun, Muye Pang, Kui Xiang, and Biwei Tang. Design of screw fastening tool based on sea. In *International Conference on Intelligent Robotics and Applications*, pages 370–381, 2019.

[90] Michael A Erdmann and Matthew T Mason. An exploration of sensorless manipulation. *IEEE Journal on Robotics and Automation*, 4(4):369–379, 1988.

[91] AK Gupta and Satish K Arora. *Industrial automation and robotics*. Laxmi publications, 2009.

[92] Matthew Mason. The mechanics of manipulation. In *IEEE International Conference on Robotics and Automation*, volume 2, pages 544–548, 1985.

[93] Randy C Brost. Automatic grasp planning in the presence of uncertainty. *The International Journal of Robotics Research*, 7(1):3–17, 1988.

[94] Kaidi Nie, Weiwei Wan, and Kensuke Harada. An adaptive robotic gripper with l-shape fingers for peg-in-hole tasks. In *IEEE/RSJ International Conference on Intelligent Robots and Systems*, pages 4022–4028, 2018.

[95] Huy Ha, Shubham Agrawal, and Shuran Song. Fit2Form: 3D generative model for robot gripper form design. In *Conference on Robotic Learning*, 2020.

[96] Kenneth Y Goldberg. Orienting polygonal parts without sensors. *Algorithmica*, 10(2-4):201–225, 1993.

[97] Jiaji Zhou, Robert Paolini, Aaron M Johnson, J Andrew Bagnell, and Matthew T Mason. A probabilistic planning framework for planar grasping under uncertainty. *IEEE Robotics and Automation Letters*, 2(4):2111–2118, 2017.

[98] Yusuke Maeda and Tomohiro Asamura. Sensorless in-hand caging manipulation. In *IEEE/RSJ International Conference on Intelligent Autonomous Systems*, pages 255–267, 2016.

[99] Péter L Várkonyi. Sensorless part feeding with round cages in two and three dimensions. *IEEE Robotics and Automation Letters*, 1(2):724–731, 2016.

[100] Michael Erdmann. An exploration of nonprehensile two-palm manipulation. *The International Journal of Robotics Research*, 17(5):485–503, 1998.

[101] Arne Schmidt, Victor M Baez, Aaron T Becker, and Sándor P Fekete. Coordinated particle relocation using finite static friction with boundary walls. *IEEE Robotics and Automation Letters*, 5(2):985–992, 2020.

[102] Robert-Paul Berretty, Ken Goldberg, Mark H Overmars, and A Frank van der Stappen. Computing fence designs for orienting parts. *Computational Geometry*, 10(4):249–262, 1998.

[103] David D Grossman and Michael W Blasgen. Orienting mechanical parts by computer-controlled manipulator. *IEEE Transactions on Systems, Man, and Cybernetics*, (5):561–565, 1975.

[104] Pragna Mannam, Alexander Volkov, Robert Paolini, Gregory Chirikjian, and Matthew T Mason. Sensorless pose determination using randomized action sequences. *Entropy*, 21(2):154, 2019.

[105] Weiwei Wan and Kensuke Harada. Reorientating objects with a gripping hand and a table surface. In *IEEE-RAS International Conference on Humanoid Robots*, pages 101–106, 2015.

[106] Chao Cao, Weiwei Wan, Jia Pan, and Kensuke Harada. Analyzing the utility of a support pin in sequential robotic manipulation. In *IEEE International Conference on Robotics and Automation*, pages 5499–5504, 2016.

[107] Daniel Sánchez, Weiwei Wan, Kensuke Harada, and Fumio Kanchiro. Regrasp planning considering bipedal stability constraints. In *IEEE-RAS 18th International Conference on Humanoid Robots*, pages 271–277, 2018.

[108] Weiwei Wan, Matthew T Mason, Rui Fukui, and Yasuo Kuniyoshi. Improving regrasp algorithms to analyze the utility of work surfaces in a workcell. In *IEEE International Conference on Robotics and Automation*, pages 4326–4333, 2015.

[109] Jiayao Ma, Weiwei Wan, Kensuke Harada, Qiuguo Zhu, and Hong Liu. Regrasp planning using stable object poses supported by complex structures. *IEEE Transactions on Cognitive and Developmental Systems*, 11(2):257–269, 2018.

[110] Kensuke Harada, Tokuo Tsuji, Kazuyuki Nagata, Natsuki Yamanobe, Hiromu Onda, Takashi Yoshimi, and Yoshihiro Kawai. Object placement planner for robotic pick and place tasks. In *IEEE/RSJ International Conference on Intelligent Robots and Systems*, pages 980–985, 2012.

[111] Heiko Mosemann, Frank Rohrdanz, and Friedrich M Wahl. Stability analysis of assemblies considering friction. *IEEE Transactions on Robotics and Automation*, 13(6):805–813, 1997.

[112] Yifang Liu, Maira Saboia, Vivek Thangavelu, and Nils Napp. Approximate stability analysis for drystacked structures. In *International Conference on Robotics and Automation*, pages 8819–8824, 2019.

[113] Kensuke Harada, Tokuo Tsuji, Soichiro Uto, Natsuki Yamanobe, Kazuyuki Nagata, and Kosei Kitagaki. Stability of soft-finger grasp under gravity. In *IEEE International Conference on Robotics and Automation*, pages 883–888, 2014.

[114] Tokuo Tsuji, Kensuke Harada, and Kenji Kaneko. Easy and fast evaluation of grasp stability by using ellipsoidal approximation of friction cone. In *IEEE/RSJ International Conference on Intelligent Robots and Systems*, pages 1830–1837, 2009.

[115] Hung Pham and Quang-Cuong Pham. Critically fast pick-and-place with suction cups. In *IEEE International Conference on Robotics and Automation*, pages 3045–3051, 2019.

[116] Mohammadali Honarpardaz, Johan Ölvander, and Mehdi Tarkian. Fast finger design automation for industrial robots. *Robotics and Autonomous Systems*, 113:120–131, 2019.

[117] Fadri Furrer, Martin Wermelinger, Hironori Yoshida, Fabio Gramazio, Matthias Kohler, Roland Siegwart, and Marco Hutter. Autonomous robotic stone stacking with online next best object target pose planning. In *IEEE International Conference on Robotics and Automation*, pages 2350–2356, 2017.

[118] Vivek Thangavelu, Yifang Liu, Maira Saboia, and Nils Napp. Dry stacking for automated construction with irregular objects. In *Proceedings of IEEE International Conference on Robotics and Automation*, pages 1–9, 2018.

[119] Peng Song, Jeffrey C Trinkle, Vijay Kumar, and Jong-Shi Pang. Design of part feeding and assembly processes with dynamics. In *IEEE International Conference on Robotics and Automation*, volume 1, pages 39–44, 2004.

[120] David J Kriegman. Let them fall where they may: Capture regions of curved objects and polyhedra. *The International Journal of Robotics Research*, 16(4):448–472, 1997.

[121] Jimmy A Jorgensen, Lars-Peter Ellekilde, and Henrik G Petersen. Handling uncertainties in object placement using drop regions. In *ROBOTIK 2012; 7th German Conference on Robotics*, pages 1–6, 2012.

[122] Péter L Várkonyi. Estimating part pose statistics with application to industrial parts feeding and shape design: New metrics, algorithms, simu-

lation experiments and datasets. *IEEE Transactions on Automation Science and Engineering*, 11(3):658–667, 2014.

[123] Márk Fekula and Gergely Horváth. Determining stable equilibria of spatial objects and validating the results with drop simulation. *Procedia CIRP*, 81:316–321, 2019.

[124] Johannes Baumgartl, Tim Werner, Per Kaminsky, and Dominik Henrich. A fast, gpu-based geometrical placement planner for unknown sensor-modelled objects and placement areas. In *IEEE International Conference on Robotics and Automation*, pages 1552–1559, 2014.

[125] Qingkai Lu and Tucker Hermans. Modeling grasp type improves learning-based grasp planning. *IEEE Robotics and Automation Letters*, 4(2):784–791, 2019.

[126] Xiaolong Li, He Wang, Li Yi, Leonidas J Guibas, A Lynn Abbott, and Shuran Song. Category-level articulated object pose estimation. In *Proceedings of the IEEE/CVF Conference on Computer Vision and Pattern Recognition*, pages 3706–3715, 2020.

[127] Rhys Newbury, Kerry He, Akansel Cosgun, and Tom Drummond. Learning to place objects onto flat surfaces in human-preferred orientations. *arXiv preprint arXiv:2004.00249*, 2020.

[128] Changhyun Choi, Wilko Schwarting, Joseph DelPreto, and Daniela Rus. Learning object grasping for soft robot hands. *IEEE Robotics and Automation Letters*, 3(3):2370–2377, 2018.

[129] Eadom Dessalene, Yi Herng Ong, John Morrow, Ravi Balasubramanian, and Cindy Grimm. Using geometric features to represent near-contact behavior in robotic grasping. In *IEEE International Conference on Robotics and Automation*, pages 2772–2777, 2019.

[130] Qian Feng, Zhaopeng Chen, Jun Deng, Chunhui Gao, Jianwei Zhang, and Alois Knoll. Center-of-mass-based robust grasp planning for unknown objects using tactile-visual sensors. *arXiv preprint arXiv:2006.00906*, 2020.

[131] Marco Santello, Martha Flanders, and John F Soechting. Postural hand synergies for tool use. *Journal of Neuroscience*, 18(23):10105–10115, 1998.

[132] Robert D Howe and Mark R Cutkosky. Practical force-motion models

for sliding manipulation. *The International Journal of Robotics Research*, 15(6):557–572, 1996.

[133] Matei Ciocarlie, Claire Lackner, and Peter Allen. Soft finger model with adaptive contact geometry for grasping and manipulation tasks. In *Second Joint EuroHaptics Conference and Symposium on Haptic Interfaces for Virtual Environment and Teleoperator Systems*, pages 219–224, 2007.

[134] Weiwei Wan, Kensuke Harada, and Fumio Kanehiro. Preparatory manipulation planning using automatically determined single and dual arms. *IEEE Transactions on Industrial Informatics*, 2019.

[135] JIS B 1082. Stress area and bearing area for threaded fasteners, 2009.

[136] JIS B 1083. Method of tightening test for threaded fasteners, 2008.

[137] Carlo Ferrari and John F Canny. Planning optimal grasps. In *Proceedings of the IEEE International Conference on Robotics and Automation*, pages 2290–2295, 1992.

[138] Michael L Stern et al. *Novel mechanical mechanisms for the development of undergraduate knowledge*. B.e. thesis, Massachusetts Institute of Technology, 2009.

[139] Shuwen Sun, Jianwu Yang, Jie Huang, and Siqi Cao. Research on the machining error analysis method of globoidal indexing cam profile. *International Journal of Mechanical Engineering and Robotics Research*, 8(2), 2019.

[140] Ian H Witten and Eibe Frank. Data mining: practical machine learning tools and techniques with Java implementations. *ACM Sigmod Record*, 31(1):76–77, 2002.

[141] Qian-Yi Zhou, Jaesik Park, and Vladlen Koltun. Fast global registration. In *Proceedings of European Conference on Computer Vision*, pages 766–782, 2016.

[142] François Pomerleau, Francis Colas, Roland Siegwart, and Stéphane Magnenat. Comparing icp variants on real-world data sets. *Autonomous Robots*, 34(3):133–148, 2013.

[143] Tokuo Tsuji, Soichiro Uto, Kensuke Harada, Ryo Kurazume, Tsutomu Hasegawa, and Ken'ichi Morooka. Grasp planning for constricted parts

of objects approximated with quadric surfaces. In *Proceedings of IEEE/RSJ International Conference on Intelligent Robots and Systems*, pages 2447–2453, 2014.

[144] Weiwei Wan and Kensuke Harada. Integrated single-arm assembly and manipulation planning using dynamic regrasp graphs. In *IEEE International Conference on Real-time Computing and Robotics*, pages 174–179, 2016.

[145] Weiwei Wan, Feng Lu, Zepei Wu, and Kensuke Harada. Teaching robots to do object assembly using multi-modal 3d vision. *Neurocomputing*, 259:85–93, 2017.

[146] Weiwei Wan and Kensuke Harada. Achieving high success rate in dual-arm handover using large number of candidate grasps, handover heuristics, and hierarchical search. *Advanced Robotics*, 30(17-18):1111–1125, 2016.

[147] Hao Chen, Juncheng Li, Weiwei Wan, Zhifeng Huang, and Kensuke Harada. Integrating combined task and motion planning with compliant control – Successfully conducting planned dual-arm assembly motion using compliant peg-in-hole control. *International Journal of Intelligent Robotics and Applications*, 4:149–163, 2020.

[148] Kaidi Nie, Felix Von Drigalski, Joshua C Triyonoputro, Chisato Nakashima, Yoshiya Shibata, Yoshinori Konishi, Yoshihisa Ijiri, Taku Yoshioka, Yukiyasu Domae, Toshio Ueshiba, et al. Team o2as'approach for the task-board task of the world robot challenge 2018. *Advanced Robotics*, 34(7-8):477–498, 2020.

[149] Rui Li and Hong Qiao. A survey of methods and strategies for high-precision robotic grasping and assembly tasks—some new trends. *IEEE/ASME Transactions on Mechatronics*, 24(6):2718–2732, 2019.

[150] Hao Chen, Juncheng Li, Weiwei Wan, Zhifeng Huang, and Kensuke Harada. Integrating combined task and motion planning with compliant control. *International Journal of Intelligent Robotics and Applications*, 4(2):149–163, 2020.

[151] Zhimin Hou, Markus Philipp, Kuangen Zhang, Yong Guan, Ken Chen, and Jing Xu. The learning-based optimization algorithm for robotic dual peg-in-hole assembly. *Assembly Automation*, 2018.

[152] Song Liu, You-Fu Li, and Dengpeng Xing. Sensing and control for simul-

taneous precision peg-in-hole assembly of multiple objects. *IEEE Transactions on Automation Science and Engineering*, 17(1):310–324, 2019.

[153] Xinran Li, Wanlin Li, Yu Zheng, Kaspar Althoefer, and Peng Qi. Criminisi algorithm applied to a gelsight fingertip sensor for multi-modality perception. In *IEEE/ASME International Conference on Advanced Intelligent Mechatronics*, pages 190–195, 2020.

[154] Yu She, Shaoxiong Wang, Siyuan Dong, Neha Sunil, Alberto Rodriguez, and Edward Adelson. Cable manipulation with a tactile-reactive gripper. In *Robotics: Science and Systems*, 2020.

[155] Ravi K Jain, Somajoyti Majumder, and Ashish Dutta. Scara based peg-in-hole assembly using compliant ipmc micro gripper. *Robotics and Autonomous Systems*, 61(3):297–311, 2013.

[156] D Shetty. Compliant gripper for precision robotic assembly. In *IEEE International Conference on Systems Engineering*, pages 335–338, 1990.

[157] Yifan Hou, Zhenzhong Jia, and Matthew T Mason. Fast planning for 3d any-pose-reorienting using pivoting. In *IEEE International Conference on Robotics and Automation*, pages 1631–1638, 2018.

[158] Elon D Rimon, Florian T Pokorny, and Weiwei Wan. Geometric characterization of two-finger basket grasps of 2-d objects: Contact space formulation. In *IEEE International Conference on Robotics and Automation*, pages 1560–1566, 2020.

[159] A. D. Kalvin and R. H. Taylor. Superfaces: polygonal mesh simplification with bounded error. *IEEE Computer Graphics and Applications*, 16(3):P.64–77, 1996.

[160] Weiwei Wan, Kensuke Harada, and Fumio Kanehiro. Planning grasps with suction cups and parallel grippers using superimposed segmentation of object meshes. *IEEE Transactions on Robotics*, 37(1):166–184, 2020.

[161] Jeffrey C Trinkle, J-S Pang, Sandra Sudarsky, and Grace Lo. On dynamic multi-rigid-body contact problems with coulomb friction. *ZAMM-Journal of Applied Mathematics and Mechanics/Zeitschrift für Angewandte Mathematik und Mechanik*, 77(4):267–279, 1997.

[162] Joshua C Triyonoputro, Weiwei Wan, and Kensuke Harada. Quickly in-

serting pegs into uncertain holes using multi-view images and deep network trained on synthetic data. In *IEEE/RSJ International Conference on Intelligent Robots and Systems*, pages 5792–5799, 2019.

[163] Weiwei Wan, Kensuke Harada, and Fumio Kanehiro. Preparatory Manipulation Planning Using Automatically Determined Single and Dual Arm. *IEEE Transactions on Industrial Informatics*, 16:442–453, 2020.

LIST OF PUBLICATIONS

Journal Articles

- Zhengtao Hu, Weiwei Wan, Keisuke Koyama and Kensuke Harada. A Mechanical Screwing Tool for Parallel Grippers—Design, Optimization, and Manipulation Policies. *IEEE Transactions on Robotics*, July 2021 (Early access).
- Zhengtao Hu, Weiwei Wan and Kensuke Harada. Designing a Mechanical Tool for Robots With Two-Finger Parallel Grippers. *IEEE Robotics and Automation Letters*, 4(3):2981 - 2988, 2019.
- Zhengtao Hu, Weiwei Wan, Keisuke Koyama, and Kensuke Harada. Reducing Uncertainty Using Placement and Regrasp Planning on a Triangular Corner Fixture. *IEEE Transactions on Automation Science and Engineering*, September 2021 (submitted).

International Conferences (non peer-reviewed)

- Zhengtao Hu, Weiwei Wan and Kensuke Harada. Designing a Mechanical Tool for 2-Finger Robotic Grippers. *1st International Symposium on Symbiotic Intelligent Systems*, 2019.

Local Conferences (non peer-reviewed)

- Zhengtao Hu, Weiwei Wan and Kensuke Harada. Picking Tasks by a Robot Using Mechanical Tools. *The Robotics and Mechatronics Conference (ROBOMECH)*, 2019.
- Zhengtao Hu, Weiwei Wan, Keisuke Koyama and Kensuke Harada. A Mechanical Rotating Tool for 2-Finger Parallel Grippers. *The Robotics and Mechatronics Conference (ROBOMECH)*, 2020.
- Zhengtao Hu, Weiwei Wan, Keisuke Koyama and Kensuke Harada. Manipulation Polices for Screw Fastening Task Using the Designed Rotating Tool. *The Robotics and Mechatronics Conference (ROBOMECH)*, 2021.
- Zhengtao Hu, Weiwei Wan, Keisuke Koyama and Kensuke Harada. Regrasp Using a Tray Corner for Eliminating Grasp Uncertainty. *The Conference of the Robotics Society of Japan(RSJ)*, 2020.
- Zhengtao Hu, Weiwei Wan, Keisuke Koyama and Kensuke Harada. Eliminating Grasp Uncertainty Using Planned Sequential Handover Regrasp with Compliance control. *The conference of the Society of Instrument and Control Engineers System Integration Division (SICE SI)*, 2021.